Calhoun: The NPS Institutional Archive

DSpace Repository

Theses and Dissertations | 1. Thesis and Dissertation Collection, all items

1998-09

Change detection analysis with spectral thermal imagery

Behrens, Richard J.

Monterey, California. Naval Postgraduate School

http://hdl.handle.net/10945/8070

Downloaded from NPS Archive: Calhoun

http://www.nps.edu/library

Calhoun is the Naval Postgraduate School's public access digital repository for research materials and institutional publications created by the NPS community. Calhoun is named for Professor of Mathematics Guy K. Calhoun, NPS's first appointed -- and published -- scholarly author.

Dudley Knox Library / Naval Postgraduate School
411 Dyer Road / 1 University Circle
Monterey, California USA 93943

NPS ARCHIVE
1998.09
BEHRENS, R.

DUDLEY KNOX LIBRARY
NAVAL POSTGRADUATE SCHOOL
MONTEREY, CA 93943-5101

DUDLEY KNOX LIBRARY
NAVAL POSTGRADUATE SCHOOL
MONTEREY CA 93943-5101

NAVAL POSTGRADUATE SCHOOL
Monterey, California

THESIS

CHANGE DETECTION ANALYSIS WITH SPECTRAL THERMAL IMAGERY

by
Richard J. Behrens

September 1998

Thesis Advisors: Richard C. Olsen
David D. Cleary

Approved for public release; distribution is unlimited

REPORT DOCUMENTATION PAGE

Form Approved
OMB No. 0704-0188

Public reporting burden for this collection of information is estimated to average 1 hour per response, including the time for reviewing instruction, searching existing data sources, gathering and maintaining the data needed, and completing and reviewing the collection of information. Send comments regarding this burden estimate or any other aspect of this collection of information, including suggestions for reducing this burden, to Washington headquarters Services, Directorate for Information Operations and Reports, 1215 Jefferson Davis Highway, Suite 1204, Arlington, VA 22202-4302, and to the Office of Management and Budget, Paperwork Reduction Project (0704-0188) Washington DC 20503.

1. AGENCY USE ONLY *(Leave blank)*	2. REPORT DATE September 1998	3. REPORT TYPE AND DATES COVERED Master's Thesis

4. TITLE AND SUBTITLE CHANGE DETECTION ANALYSIS WITH SPECTRAL THERMAL IMAGERY	5. FUNDING NUMBERS
6. AUTHOR(S) Behrens, Richard J.	
7. PERFORMING ORGANIZATION NAME(S) AND ADDRESS(ES) Naval Postgraduate School Monterey, CA 93943-5000	8. PERFORMING ORGANIZATION REPORT NUMBER
9. SPONSORING / MONITORING AGENCY NAME(S) AND ADDRESS(ES)	10. SPONSORING / MONITORING AGENCY REPORT NUMBER

11. SUPPLEMENTARY NOTES

The views expressed in this thesis are those of the author and do not reflect the official policy or position of the Department of Defense or the U.S. Government.

12a. DISTRIBUTION / AVAILABILITY STATEMENT	12b. DISTRIBUTION CODE
Approved for public release; distribution is unlimited.	

13. ABSTRACT *(maximum 200 words)*

Spectral imagery offers additional information about a scene that can enhance an analyst's ability to conduct change detection. Change detection is required to automate to the process of sifting through countless images to identify scenes that have significant intelligence value. Change detection in spectral thermal imagery enables exploitation at night by taking advantage of the emissive characteristics of the scene. Data collected from the Spatially Enhanced Broadband Array Spectrograph System (SEBASS) were used to investigate the feasibility of spectral thermal change detection in the long wave infrared (LWIR) region. This study used analysis techniques such as differencing, histograms, and principal components analysis to detect spectral changes and investigate the utility of spectral change detection. Many undesirable characteristics exist that influence the sensitivity of change detection methods. Temperature dependence and gross registration errors greatly affect an analysts ability to make use of spectral thermal data for change detection; however, with effort, spectral changes were still detected with these data and suggest that the techniques would be useful once the undesirable characteristics are minimized.

14. SUBJECT TERMS Remote sensing, Hyperspectral, Digital Imagery Analysis, Change Detection, SEBASS, CARD SHARP, Camp Pendleton	15. NUMBER OF PAGES 152
	16. PRICE CODE

17. SECURITY CLASSIFICATION OF REPORT	18. SECURITY CLASSIFICATION OF THIS PAGE	19. SECURITY CLASSIFI- CATION OF ABSTRACT	20. LIMITATION OF ABSTRACT
Unclassified	Unclassified	Unclassified	UL

NSN 7540-01-280-5500

Standard Form 298 (Rev. 2-89)
Prescribed by ANSI Std. 239-18

DUDLEY KNOX LIBRARY
NAVAL POSTGRADUATE SCHOOL
MONTEREY, CA 93943-5101

Approved for public release; distribution is unlimited

CHANGE DETECTION ANALYSIS WITH SPECTRAL THERMAL IMAGERY

Richard J. Behrens
Lieutenant, United States Navy
B.S., Rochester Institute of Technology, 1994

Submitted in partial fulfillment of the
requirements for the degree of

MASTER OF SCIENCE IN SPACE SYSTEMS OPERATIONS

from the

NAVAL POSTGRADUATE SCHOOL
September, 1998

ABSTRACT

Spectral imagery offers additional information about a scene that can enhance an analyst's ability to conduct change detection. Automation of change detection is required to sift through countless images to identify scenes that have significant intelligence value. Change detection in spectral thermal imagery enables exploitation at night by taking advantage of the emissive characteristics of materials. Data collected from the Spatially Enhanced Broadband Array Spectrograph System (SEBASS) were used to investigate the feasibility of spectral thermal change detection in the long wave infrared (LWIR) region. This study used analysis techniques of differencing, histograms, and principal components analysis to detect spectral changes and investigate the utility of spectral change detection. Many artifacts can influence the sensitivity of change detection methods. Temperature dependence and gross registration errors greatly affect an analysts ability to make use of spectral thermal data for change detection; however, with effort, spectral changes were still detected with these data and suggest that the techniques would be useful once the undesirable characteristics are minimized.

TABLE OF CONTENTS

I. INTRODUCTION 1

II. BACKGROUND 5

A. SPECTRAL ANALYSIS 5
1. Principal Components Analysis (PCA) 6
2. Spectral Angle Mapper 10

B. THERMAL ANALYSIS 11

C. MULTISPECTRAL ANALYSIS 13
1. Image Differencing 13
2. Image Ratioing 16
3. Index Differencing 18
4. Principal Components Analysis 21
5. Post Classification Comparison 29
6. Direct Multidate Classification 31
7. Change Vector Analysis 34
8. Previous Studies 38

III. THE SPATIALLY ENHANCED BROADBAND ARRAY SPECTROGRAPH SYSTEM (SEBASS) 41

A. DESIGN 41

B. CALIBRATION 46
1. Spectral Calibration 46
2. Radiometric Calibration 49

C. CHARACTERISTICS 51
1. Thermal Drift 51
2. Unresponsive Detectors and Pixel Slip 51

IV. DATA COLLECTION 53

A. CARD SHARP 53
1. The Collection Scenario 54
2. Data 59

B. MCAS CAMP PENDLETON 59

1. Collection Parameters 60
2. Target Description 61
3. Considerations 61

C. CONSIDERATIONS FOR SPECTRAL CHANGE DETECTION 64

V. DATA ANALYSIS 69

A. METHODS FOR HYPERSPECTRAL CHANGE DETECTION 69

B. CHANGE DETECTION: CARD SHARP 70
1. Image Differencing and the Target-to-Background Separation (TBS) 70
2. Spectral Angle 85

C. CHANGE DETECTION: CAMP PENDLETON 87
1. Image Differencing 87
2. Spectral Angle 95
3. Registration Errors and False Detections 98

VI. RESULTS 103

A. SEBASS INSTRUMENT AND DATA 103

B. EVALUATION OF SPECTRAL CHANGE TECHNIQUES 103

C. THE UTILITY OF THERMAL DATA FOR CHANGE DETECTION. 105

D. REQUIREMENTS FOR IMPROVED CHANGE DETECTION 106

VII. CONCLUSION 107

APPENDIX A. HYPERSPECTRAL ANALYSIS TECHNIQUES 109

APPENDIX B. COLOR FIGURES 111

LIST OF REFERENCES 129

INITIAL DISTRIBUTION LIST 133

LIST OF FIGURES

Figure 2.1: A subset of two Landsat TM images of Boulder, Colorado are used as examples in this chapter. 5
Figure 2.2: A graphical depiction of the eigenvectors produced from a DKLT (from Therrien, 1992). 7
Figure 2.3: Principal component transform a 6-band Landsat TM image of Boulder, Colorado acquired in August, 1985 8
Figure 2.4: Standardized principal components produced from the same Landsat image in Figure 2.3. 9
Figure 2.5: A graphical illustration of the spectral angle for a two-band example (after Collins, 1996). 10
Figure 2.6: A diagram of the components of emitted radiation reaching the sensor. 12
Figure 2.7: A histogram of the differenced image in Figure 2.8. 14
Figure 2.8: Image differencing as applied to Landsat TM images of Boulder, Colorado acquired on August and October, 1985. 15
Figure 2.9: The histogram for ratio band 4 of the Boulder scene. 16
Figure 2.10: The same Band 4 images used in Figure 2.8 applied to ratioing. Note that the center of the ratio scale is not 1.0. 17
Figure 2.11: NDVI differenced image of the Boulder scene. 20
Figure 2.12. Principal components analysis where band-by-band differencing is used. . 21
Figure 2.13: Differenced principal components bands of the Landsat Boulder image. Each band represents the of the August PC band from the same PC band in October. 22
Figure 2.14. Spectral Principal Components Analysis. 23
Figure 2.15: The first 6 PC bands produced by combining the two Boulder images and conducting the tranform on the 12-band composite image. 25
Figure 2.16: A sample of three eigenvectors for the 12-band composite image. The bands are separated into two lines by date and overlaid for a better comparison. 26
Figure 2.17. NDVI-based Principal Components Analysis. 27
Figure 2.18: Two NDVI images combined and converted to principal components. PC band 2 identifies the areas of change 28
Figure 2.19: A flow diagram illustrating post classification comparison. 29
Figure 2.20: Post classification comparison as applied to the water class on the Boulder scene. 30
Figure 2.21: Direct multidate classification. The right side is a breakout of the various classes. Classes 3 and 7 contain change information. 33
Figure 2.22: A scatter plot of three classes. 34
Figure 2.23. An illustration of the formation of a change vector using two-band image vectors (after Deer, 1995) 35
Figure 2.24: Spectral angle mapper using a mean vegetation spectrum as the reference. 37

Figure 3.1: SEBASS installed in the aircraft atop the roll compensator. 40
Figure 3.2: The SEBASS optical layout (From Hackwell, 1997)..... 41
Figure 3.3: The SEBASS FPA configuration (From Hackwell, 1997)..... 41
Figure 3.4: A plot of the band width of each spectral band for the LWIR channel..... 42
Figure 3.5: The flight crew maintains a sufficient liquid helium level to keep the FPAs at 11°K. 43
Figure 3.6: The effects of coadding frames on the noise equivalent spectral response (from Hackwell, 1997). 43
Figure 3.7: The flight crew monitors SEBASS status and operation from this console.. 44
Figure 3.8: This graph depicts the shape of the slit image at the FPAs for four wavelengths. The variation is less than one pixel. The FPA diagram (right) orients the array. (From Hackwell, 1997) 46
Figure 3.9: This graph depicts the shape of the slit image across the spectral dimension. The FPA diagram (right) orients the graph. (from Hackwell, 1997) 46
Figure 3.10: The polymer film is inserted in place for the LWIR wavelength calibration. 48
Figure 4.1: Site layout at Redstone Arsenal (from Smith and Schwartz, 1997). 55
Figure 4.2: Vehicle positions in the CARD SHARP field of view..... 56
Figure 4.3: The M1E1 Abrams MBT positioned at site S1 with woodland camouflage. 57
Figure 4.4: The M1E1 Abrams MBT positioned at site S1 without camouflage. 57
Figure 4.5: A composite image consisting of Landsat TM (bands 1, 2, and 3), a color aerial photograph mosaic, and the two of the SEBASS images scanned for this study. 60
Figure 4.6: The cross-correlation technique for removing error correction. (a) The uncorrected image. (b) The technique by finding the offset with the highest correlation. (c) The corrected (straightened) image. 62
Figure 4.7: A subset of the Camp Pendleton supply depot where roll correction and registration has been applied. 62
Figure 4.8: These images show that an along-track gradient exists where the left side of the image is brighter than the right side. 64
Figure 4.9: A comparison of PC bands 1, 7, and 15 for both dates and the difference between the two dates. 65
Figure 4.10: A comparison of CARD SHARP images converted to emissivity. 66
Figure 4.11: Histograms of band 64 from both dates converted to emissivity. 67
Figure 5.1: A change image created by first averaging all bands of each hypercube and then differencing the two resulting images. 71
Figure 5.2: A histogram of the CARD SHARP change image in Figure 5.1 produced from the pseudo FLIR images. 72
Figure 5.3: The first 200 lines of the CARD SHARP change vector - eighteen bands spaced seven bands apart..... 73
Figure 5.4: Ground truth spectra acquired during CARD SHARP for the M-60A MBT.74

Figure 5.5: A variety of difference spectra produced by subtracting the spectrum at a given pixel location in the 10 October image from the spectrum at the same pixel location in the 11 October image. 75
Figure 5.6: MODTRAN output for Huntville, Alabama during October. 76
Figure 5.7: A comparison of SEBASS and ground truth *difference* data for the M-60A MBT with and without camouflage. 77
Figure 5.8: A comparison of three significant bands. 78
Figure 5.9: Histogram for CARD SHARP difference band 27 (9.16 μm). 79
Figure 5.10: Change image for CARD SHARP difference band 27 (9.16 μm). 79
Figure 5.11: Histogram for CARD SHARP difference band 33 (9.50 μm). 80
Figure 5.12: Change image for CARD SHARP difference band 33 (9.50 μm). 80
Figure 5.13: Histogram for CARD SHARP difference band 86 (12.02μm). 81
Figure 5.14: Change image for CARD SHARP difference band 86 (12.02 μm). 81
Figure 5.15: Histogram for CARD SHARP difference band 98 (12.52 μm). 82
Figure 5.16: Change image for CARD SHARP difference band 98 (12.52 μm). 82
Figure 5.17: Target-to-background separation for the CARD SHARP change image. ... 83
Figure 5.18: A scatter plot for CARD SHARP difference band 27 (9.16 μm) and band 33 (9.50 μm). 84
Figure 5.19: Histogram for the CARD SHARP spectral angle result. 86
Figure 5.20: Change image for the CARD SHARP spectral angle result. 87
Figure 5.21: Image differencing result for band 51 (10.28 μm) of the Camp Pendleton data. Two genuine changes are indicated at A and B. 88
Figure 5.22: A sample of three spectra across change A in Figure 5.21 89
Figure 5.23: The histogram for difference band 51 of the Camp Pendleton change vecotor. 90
Figure 5.24: A sample of five spectra across change B in Figure 5.21. 91
Figure 5.25: The two-dimensional scatter plot comparing difference bands 28 and 51. 92
Figure 5.26: The change result for the Camp Pendleton data using the second principal component of the difference bands 28 and 51 93
Figure 5.27: The histogram for the PCA result of the Camp Pendleton data. 94
Figure 5.28: The principal component rotation of the scatter plot in Figure 5.25 The change class are now at the top of the plot. 94
Figure 5.29: Spectral angle result for the Camp Pendleton data. 96
Figure 5.30: A tighter view of Figure 5.29. 97
Figure 5.31: A sample of spectra from pixel that exhibit high change in the spectral angle result. 100
Figure 5.32: A sample of pixels representing varying degrees of change 101

LIST OF TABLES

Table 2.1: Summary of the best classification performance for the change detection techniques studied (from Singh, 1989). Bands refer to Landsat MSS. 39
Table 2.2: Accuracy assessment of five change detection techniques used to assess vegetation response to flooding (from Michener and Houhoulis, 1997 39
Table 3.1: Unresponsive LWIR detectors (From Smith and Schwartz, 1997). 51
Table 3.2: Unresponsive MWIR detectors (From Smith and Schwartz, 1997). 51
Table 4.1: Location and description of equipment for scenarios 1 and 2 (after Smith and Schwartz, 1997) 58

ACKNOWLEDGEMENTS

The author would like to thank John Hackwell of the Aerospace Corporation for his guidance and for collecting the Camp Pendleton data used in this thesis. Special thanks to Thomas Hayhurst, Bob Johnson, Brad Johnson, and Cameron Purcell of the Aerospace Corporation for sharing their expertise and providing assistance. The author would also like to thank Craig Schwartz for providing input regarding the CARD SHARP collect. Most of all, the author would like to thank his wife, Dawn, for her unwavering love and support (Philippians 2:1-4).

I. INTRODUCTION

Imaging spectroscopy, the collection of spectral information displayed in spatial form, has widened prospects for image exploitation and intelligence collection and analysis. Broadband images often fail to provide sufficient information to discriminate low contrast targets that might be employing concealment techniques. To date, studies in spectral imagery have explored the detection of anomalies (i.e. the presence of an unnatural objection in a natural background). This would allow the analyst to quickly locate concealed targets by exploiting one image at a time. While many would argue that anomaly detection is sufficient for most military applications, it will only partially reduce the increasingly unmanageable amount of imagery data. To check all anomalies every time they appear in an image would still require a great deal of analyst effort, yet most of those anomalies will not require repeated analysis – unless something about that anomaly changes.

For example, an analyst might be responsible for monitoring the operational status of several ground combatant facilities in a country that is known for a very slow operational tempo. On most days, the majority of military vehicles remain in place indicating no change in operational status; however, each vehicle is considered an anomaly compared to the parking areas, dirt, and vegetation. A reasonably intelligent adversary would attempt to increase operational tempo undetected by replacing each unit with a similar-looking decoy so that no major change is noticed on broadband imagery. The subtle spectral difference may also be overlooked by an analyst who still detects an object that differs little from the past several months. However, if the proper change detection algorithm were employed in this scenario, the analyst would need to spend little time and effort on scenes where little change occurs. Such algorithms could be sensitive to subtle spectral changes which would prompt the analyst at the proper time to take a closer look at the scene. This would significantly reduce the requirement for in-depth analysis on every scene while improving the analyst's ability small but anomalous *changes*.

Similar examples exist in power plant configuration, chemical and biological weapons production, and many other areas in which imagery analysts spend an inordinate amount of time. As the number of targets and the amount of data available for each target increase, interpretation must be streamlined and automated freeing the analyst to investigate images of potentially significant intelligence value. Change detection provides a means for eliminating null target areas – areas in which activity is minimal or does not fit a predetermined profile. Spectral change detection provides the added sensitivity to the change detection process reduces vulnerabilities to camouflage, concealment, and deception (CC&D) techniques.

This study begins to investigate the feasibility of hyperspectral change detection in a military context. It focuses on the ability to employ these methods with hyperspectral imagery collecting in the long wave infrared (LWIR) region of the spectrum. This region comes with a set of unique characteristics and challenges, including a dependence on target temperature. The single most important characteristic is that thermal sensors do not require daylight for operation thus enabling spectral image collection at night. However, the thermal dependence may complicate spectral analysis and reduce the sensitivity of change detection techniques. Also, the spectral features of interest in military operations are more subtle in the LWIR than in the reflective regions of the spectrum such as visible, near infrared (NIR), and short-wave infrared (SWIR).

This study examines change detection techniques currently used in broadband multispectral imagery and summarizes their effectiveness in previous studies. Next an overview of the MWIR/LWIR sensor, the Spatially Enhanced Broadband Array Spectrograph System (SEBASS), is provided. The study consists of data from two collects: the Capabilities and Requirements Development of the SEBASS High Altitude Reconnaissance Project (CARD SHARP) and two consecutive overflights of the Camp Pendleton Marine Corps Air Station. The CARD SHARP data provide insight to the use of spectral change detection of camouflaged vehicles in a heavily vegetated environment. The Camp Pendleton data provide similar insight in a military industrial environment. These data are evaluated for their utility with respect to change detection and aid in the

characterization of problems associated with thermal hyperspectral data with regard to change detection.

The quality of both data sets prohibited side-by-side comparisons of a variety of techniques previously used in multispectral analysis. Instead, the focus of this study is on the sensitivity of the instrument to detect spectral change separate from thermal change in two different collection environments. It also investigates useful ways to detect, identify, and analyze spectral change. Finally, this study will attempt to assess the feasibility of thermal hyperspectral change detection and characterize requirements in signal-to-noise ratio and registration accuracy that would greatly improve the change detection process.

II. BACKGROUND

A. SPECTRAL ANALYSIS

To understand spectral change detection, it is import to first review the development of hyperspectral analysis. Most of the current analysis techniques have been adapted from mulitspectral analysis and the analysis of three-dimensional matrices.

Stefanou (1997) applied a signal processing perspective to hyperspectral analysis and catalogued 18 different techniques organized into families based on the amount of *a priori* knowledge required for each technique. His work is summarized in Appendix A. Certain spectral analysis techniques are well suited for change detection. This section will cover those techniques.

For illustration purposes, this chapter will use Landsat TM images to provide a consistent comparison of all techniques explained here. The images used are of Boulder, Colorado taken in August and October of 1985. They have been subsetted to the same 1000 x 1000 pixel scene (Figure 2.1). A color version of this figure is available in Appendix B. Band 6, the LWIR band, has been omitted.

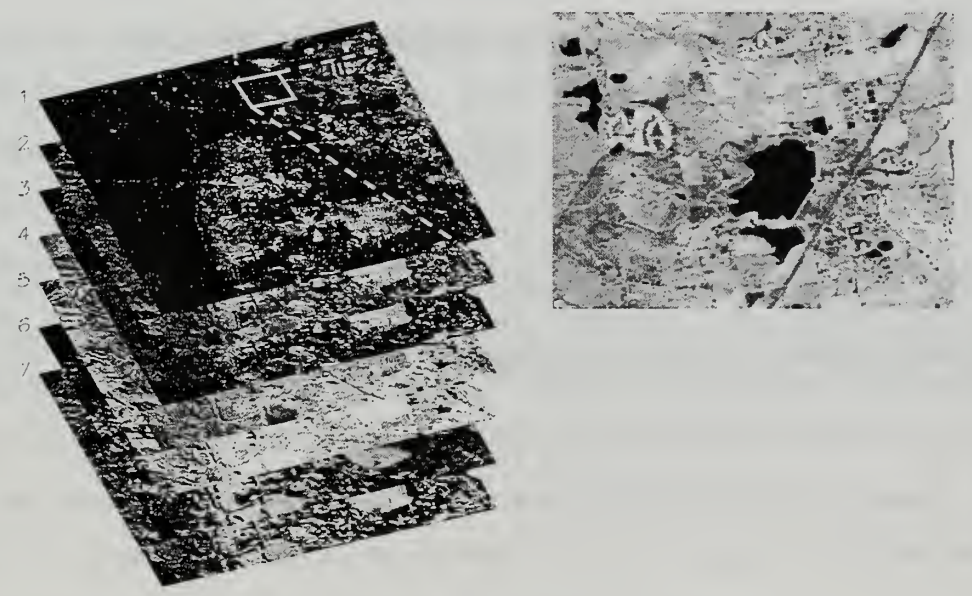

Figure 2.1: A subset of two Landsat TM images of Boulder, Colorado are used as examples in this chapter.

1. Principal Components Analysis (PCA)

Since redundancy exists between spectral bands in a hyperspectral image, principal components analysis (PCA) seeks to transform the observed spectral axes to a new coordinate system ordered according to variance (Stefanou, 1997). The transform decorrelates the original information and orders the bands in a way that allows the information to be represented by a smaller number of bands.

PCA uses the Karhunen-Loeve Transform (KLT) which expands the data set as a weighted sum of basis functions. These basis functions represent the eigenvectors of the covariance matrix of the data set. Therien (1992) describes the discrete form, the DKLT, as following the relation,

$$\kappa_i = \sum_{n=0}^{N-1} \varphi_i^*[n] x[n] \tag{2.1}$$

where κ_i are coefficients of orthonormal basis function, $\varphi_i[n]$, and $x[n]$ is a random sequence of $n = \{0,1, \ldots, N\text{-}1\}$ such that

$$x[n] = \kappa_1 \varphi_1[n] + \kappa_2 \varphi_2[n] + \cdots + \kappa_N \varphi_N[n] \tag{2.2}$$

The basis function, $\varphi_i[n]$, is orthonormal when it satisfies the relation

$$\sum_{n=0}^{N-1} \varphi_i^*[n] \varphi_j[n] = \begin{cases} 1 & i = j \\ 0 & i \neq j \end{cases} \tag{2.3}$$

Figure 2.2 depicts the DKLT. The basis funtions, $\varphi_i[n]$, represent the eigenvectors of $x[n]$ each weighted by the principal component scores κ_i (Stefanou, 1997).

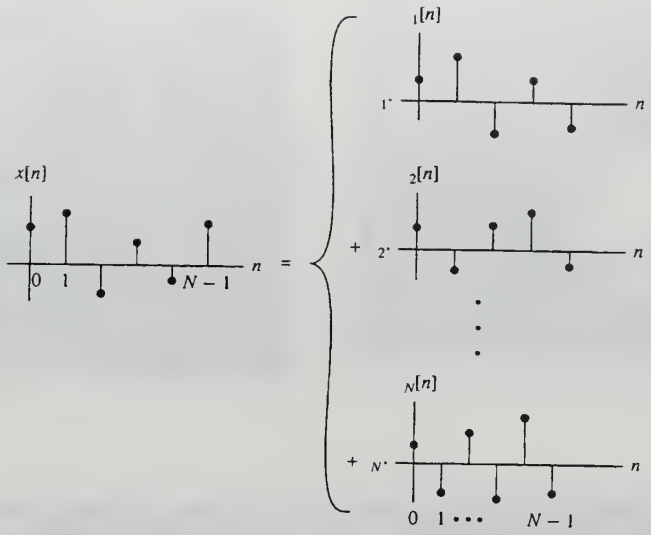

Figure 2.2: A graphical depiction of the eigenvectors produced from a DKLT (from Therrien, 1992).

The basic PCA uses eigenvectors of the covariance matrix to create a unitary transform matrix. This matrix is applied to each pixel vector and transforms it into a new vector with uncorrelated components ordered by variance (Stefanou, 1997). Because PCA depends on scene variance both spectrally and spatially, results depend on features specific to each scene. As certain features differ in a given scene, certain principal components will change while others may not. Figure 2.3 contains the six principal components for the August Boulder image. The bands are numbered such that one is the most significant band (has the highest eigenvalue).

It is also important to note that the first several principal component (PC) bands carry the most information about scene variance; however, they may not always carry the information of interest. The signal-to-noise ratio (SNR) is not the same in all bands which can obscure information in higher PC bands. To improve this situation, standardized principal components analysis (SPCA) was introduced. SPCA causes each spectral band to contribute equal weight by first normalizing the covariance matrix. This transforms the covariance matrix to the correlation matrix. Figure 2.4 contains the six standardized principal components from the August Boulder image.

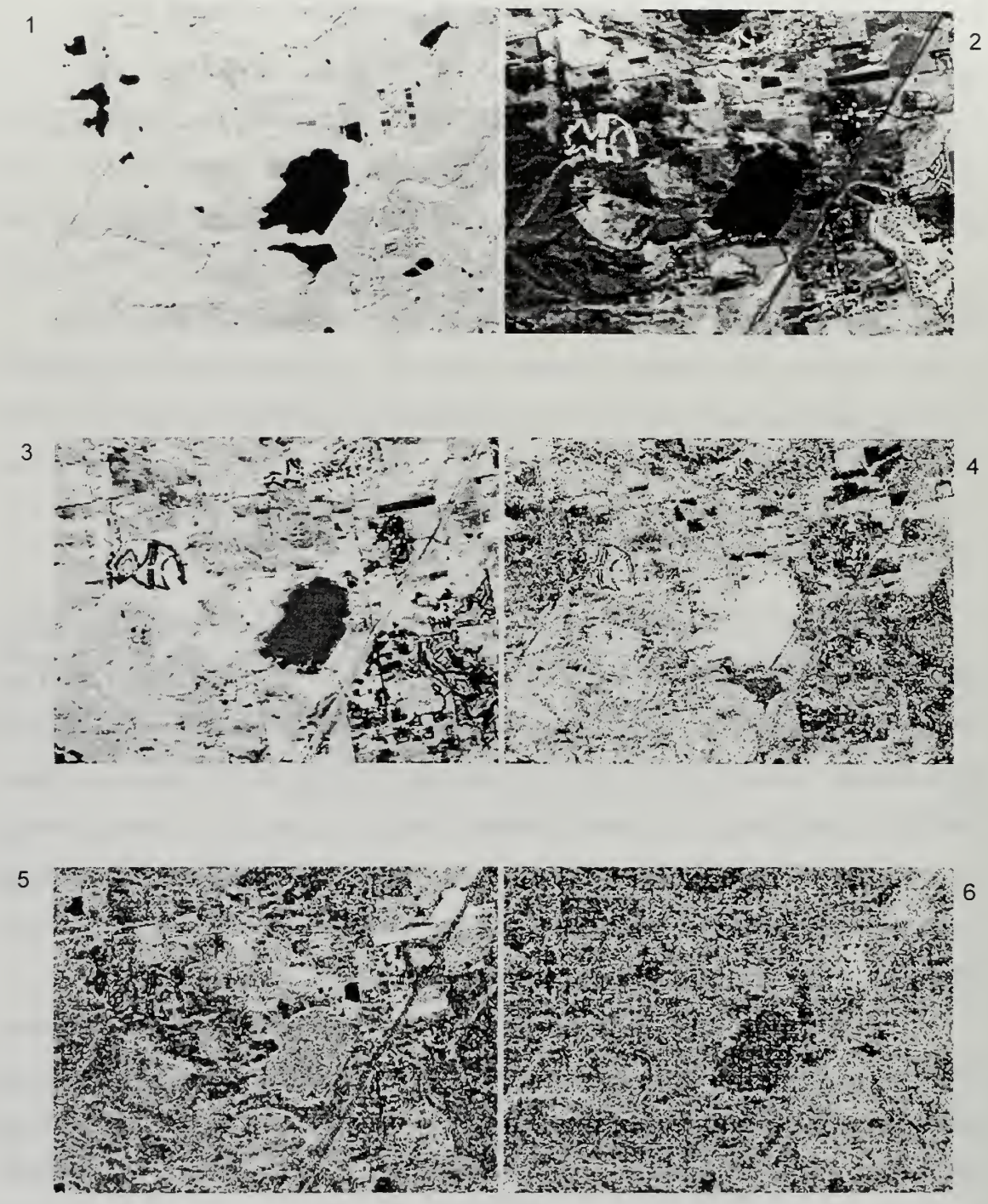

Figure 2.3: Principal component transform a 6-band Landsat TM image of Boulder, Colorado acquired in August, 1985.

Figure 2.4: Standardized principal components produced from the same Landsat image in Figure 2.3.

2. Spectral Angle Mapper

Spectral angle mapper (SAM) measures the spectral similarity between a reference spectrum and the spectra found at a pixel of the image. This assumes that the spectrum of interest is abundant in a given pixel to the extent that it adequately matches a pure reference spectrum. Spectral similarity is manifest as an angle between the pixel vector and the vector of the reference spectrum. This is illustrated in Figure 2.5.

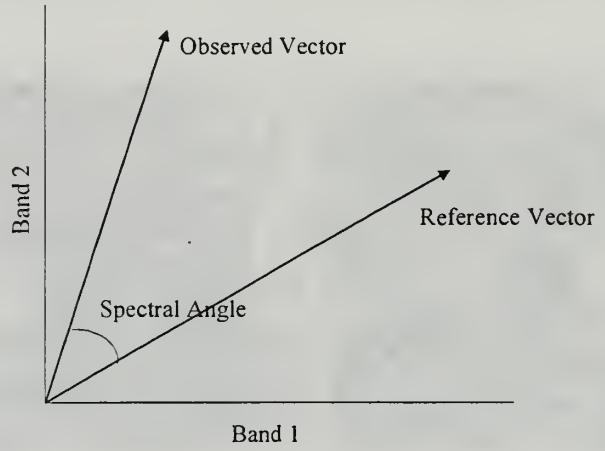

Figure 2.5: A graphical illustration of the spectral angle for a two-band example (after Collins, 1996).

Yuhas, Goetz, and Boardman (1992) express the spectral angle, in radians, as

$$\cos^{-1}\left(\frac{\mathbf{x}\bullet\mathbf{u}}{\|\mathbf{x}\|\|\mathbf{u}\|}\right)=\cos^{-1}\left(\frac{\sum_{i=1}^{l}x_i u_i}{\sqrt{\sum_{i=1}^{l}x_i^2}\sqrt{\sum_{i=1}^{l}u_i^2}}\right) \tag{2.4}$$

Where **x** is the observed pixel vector and **u** is the reference vector. The dot product of **x** and **u** are divided by the product of their Euclidean norms to cancel out the amplitude difference of the two vectors.

The output of a SAM algorithm is a multiband image where the number of bands equals the number of reference spectra used in the algorithm. Pixel brightness indicates

the degree of similarity of the pixel to the given reference spectrum. SAM tends to perform independent of scene illumination and sensor gain (Collins, 1996), but its deterministic approach ignores the natural spectral variability of a species and spectral shifts caused by atmospheric contaminants.

B. THERMAL ANALYSIS

Thermal data come with their own set of characteristics and problems that require specific attention when applying techniques developed for other regions of the spectrum. The first is that radiation from an object is dependent upon temperature. This is expressed in Planck's Radiation Law.

$$B_\lambda(T) = \frac{C_1 \lambda^{-5}}{e^{\frac{C_2}{\lambda T}} - 1} \tag{2.5}$$

Where $B(T)$ is the radiance emitted from a blackbody, C_1 and C_2 are constants (1.191×10^{10} $\mu W/cm^2\mu msr$, 1.143×10^{4} μmK respectively), λ is the wavelength of the radiation observed (in microns), and T is the temperature of the blackbody in degrees Kelvin.

Most issues surrounding thermal data are centered on the confounding of temperature with emissivity. Emissivity is the ratio of the emitted radiance of a real object to that of a blackbody radiating at the same temperature. Equation 2.8 describes the relationship of temperature and emissivity.

$$L = \tau_\lambda \varepsilon_\lambda B_\lambda(T) \tag{2.6}$$

Where L is the radiance at the sensor contributed by the observed object and ε is the object's emissivity. The radiance of the material is also attenuated by the atmospheric transmittance, τ_λ.

Temperature has a dramatic effect on an object's emitted radiance, and therefore makes it difficult to distinguish the type of material observed from its temperature. It then becomes important to separate the two variables by estimating the blackbody radiance and dividing it from Equation 2.6. Before this can be accomplished, we must

estimate the effects of atmospheric attenuation and sources of radiation that reach the sensor not related to the obect's emission. Total at-sensor radiance can be expressed as

$$L_{sensor} = \underbrace{\tau_\lambda \varepsilon_\lambda B_\lambda(T)}_{\text{Object Radiance at the Sensor}} + \underbrace{\tau_\lambda (1.0 - \varepsilon_\lambda) L_{downwelling}}_{\text{Downwelling Radiance at the Sensor}} + \underbrace{L_{upwelling}}_{\text{Upwelling Radiance at the Sensor}} \quad (2.7)$$

In addition to the object radiance, radiance from the atmosphere itself contributes to the total at-sensor radiance. Figure 2.6 illustrates the process of thermal radiative transfer.

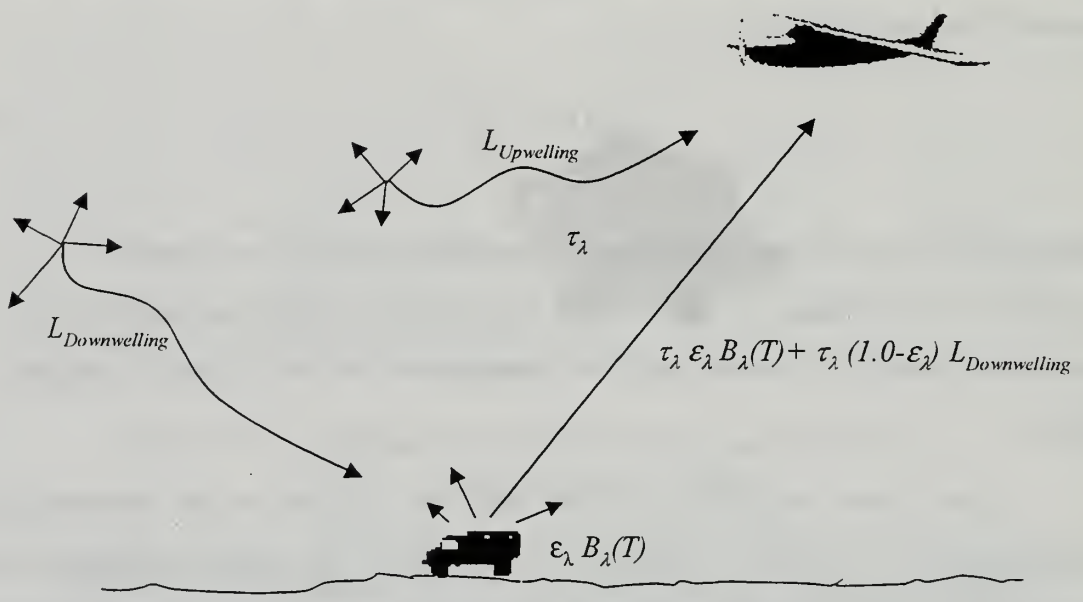

Figure 2.6: A diagram of the components of emitted radiation reaching the sensor.

To compensate for the atmosphere, Hackwell and Hayhurst (1995) developed the plastic ruler technique specifically for infrared hyperspectral remote sensing. This technique assumes an emissivity of 1.0 for some key scene elements thus eliminating the downwelling radiance contribution in Equation 2.9. Collins (1996) provides a more detailed description of the plastic ruler atmospheric compensation technique. In order to accurately use this technique, blackbody emitters with known temperatures must be present in the scene. Vegetation is typically used as a blackbody emitter. Once atmospheric compensation is complete, Plank's Law (Equation 2.7) can be used to determine the temperature of every pixel in the image.

C. MULTISPECTRAL ANALYSIS

Much of the current research on change detection has been applied to multispectral imagery in the context of environmental monitoring. Studies usually focus on a single technique that seems suited to a specific application such as coastal zone monitoring (Weismiller, *et al*, 1997) or land cover change (Suga, *et al*, 1993). What follows is a description of several change detection techniques that frequently appear in the literature and may have application to hyperspectral imagery.

1. Image Differencing

The earliest techniques for comparing two co-registered images acquired at different times has been to perform a point-to-point subtraction. Singh (1989) describes the operation as

$$Dx_{ij}^{k} = x_{ij}^{k}(t_2) - x_{ij}^{k}(t_1) + C \tag{2.8}$$

where Dx_{ij}^{k} is the difference between the images at times t_1 and t_2 of pixel value x at i,j. The superscript, k, represents the spectral band and C is a constant used to prevent negative digital numbers. This produces a difference distribution (Figure 2.7) for each band where areas of change are found in the tails of the distribution while areas of no change fall near the mean. The change threshold is often established by specifying the number of standard deviations from the mean.

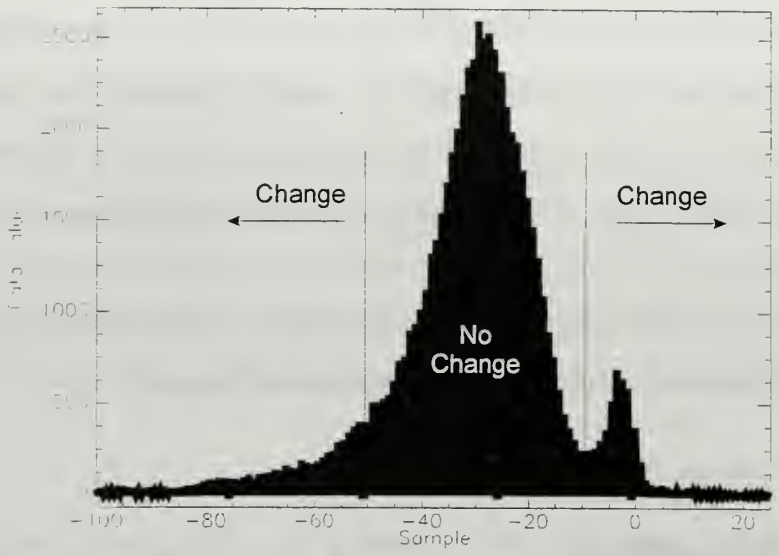

Figure 2.7: A histogram of the differenced image in Figure 2.8.

Figure 2.8 illustrates this technique. Band 4 is shown for August and October in the top two panels, and the difference is shown in the bottom panel. The difference panel has been scaled from –128 to 128. Note that bright areas in the change image represent areas of increased radiance from August to October, and dark areas represent decreased radiance. While it may be useful to threshold the image to highlight the changes, not doing so provides a better view of the degree of change. Note the light region around the reservior, which has decreased in size.

Image differencing is the simplest and most widely used of all techniques (Singh, 1989); however, a number of disadvantages accompany the method. Differencing requires precise registration and does not account for the existence of mixed pixels. It usually fails to consider the starting and ending point of a pixel in feature space. Differencing often loses information. For instance, two differenced pixels can have the same value (degree of change), but this says nothing about the type of change that has occurred (Riordan, 1980). For instance, a change of 40 may be caused by differencing two pixels from 160 to 120 or from 90 to 50. If might be difficult to determine if a lake had receded or urban development had increased.

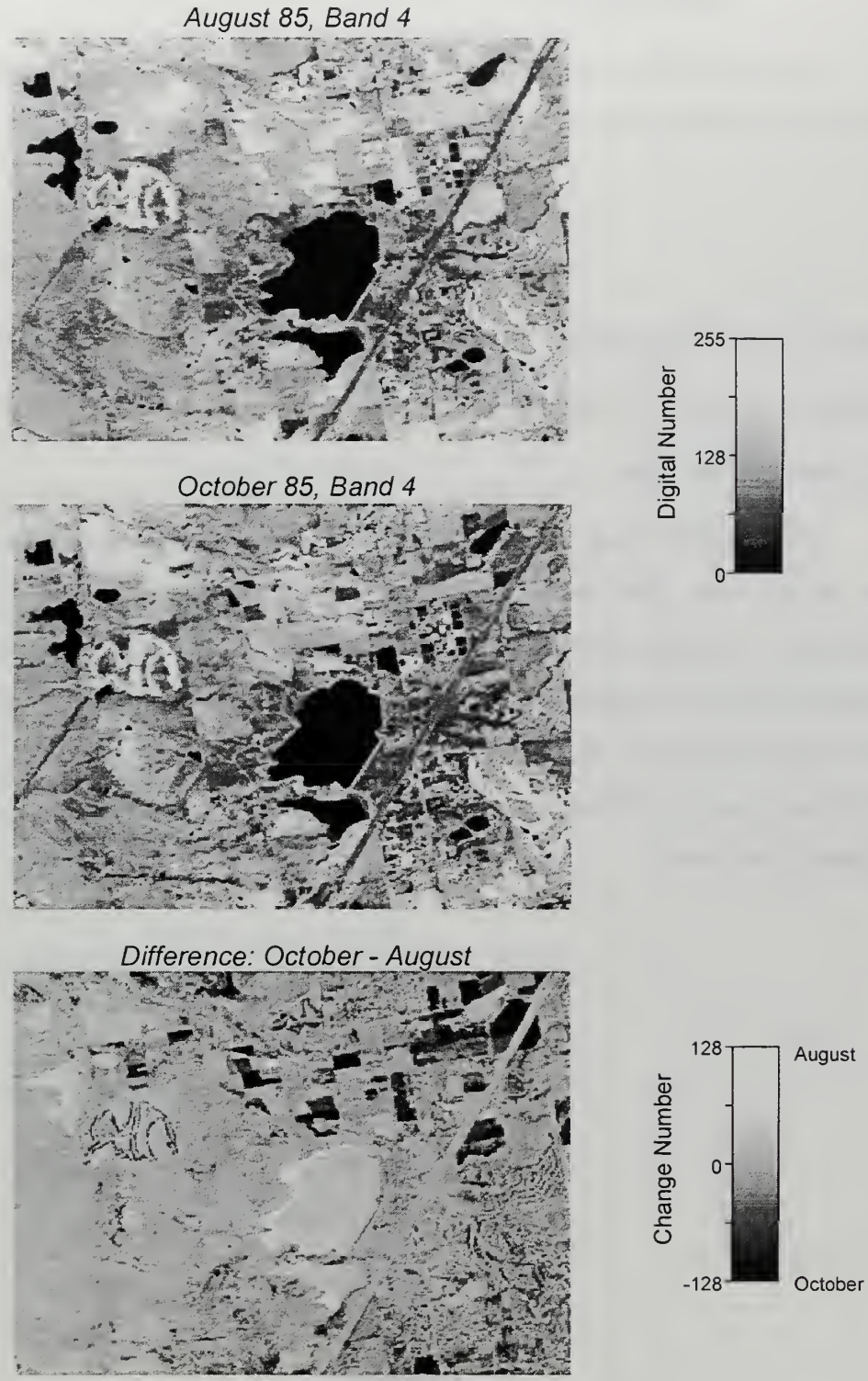

Figure 2.8: Image differencing as applied to Landsat TM images of Boulder, Colorado acquired on August and October, 1985.

2. Image Ratioing

Similar to differencing, image ratioing is a point-to-point operation that compares two images by dividing one by the other. Singh (1989) expresses ratioing as

$$Rx_{ij}^{k} = \frac{x_{ij}^{k}(t_1)}{x_{ij}^{k}(t_2)} \tag{2.9}$$

Where Rx_{ij}^{k} is the ratio of pixel i,j at times t_1 and t_2. When $Rx_{ij}^{k} = 1$, no change has occurred in that pixel. When $\left|Rx_{ij}^{k}\right| > T$, where T is a predetermined threshold, a change has occurred in that pixel.

Unlike differencing, the ratio distribution is non-normal as shown in Figure 2.9. This would mean that change thresholds are seldom equal on both sides of the distribution. If standard deviations are used to determine the thresholds, then the "areas of change" under the distribution curve are not equal, therefore the error rates above and below unity will not be equal. For this reason, ratioing is seldom used. Figure 2.10 depicts image ratioing. Even though a ratio of 1.0 indicates no change, it does not fall on the middle gray value.

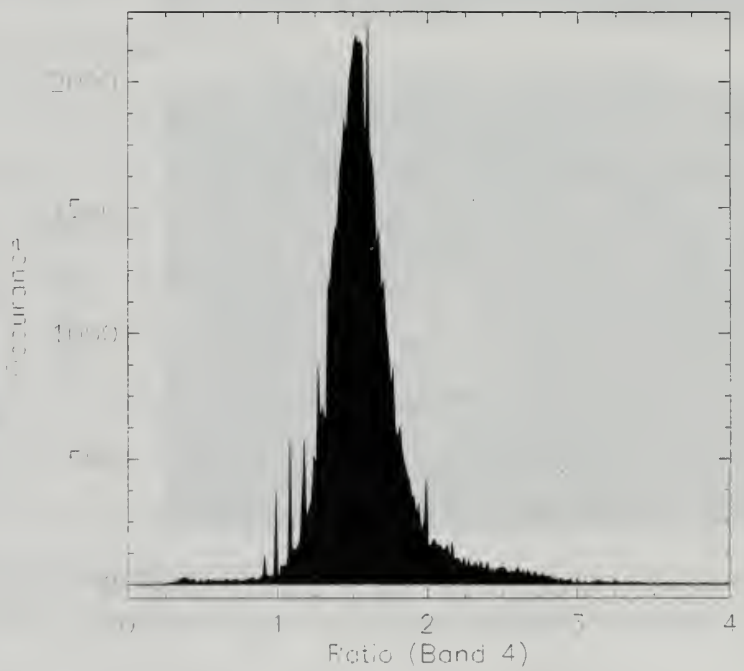

Figure 2.9: The histogram for ratio band 4 of the Boulder scene.

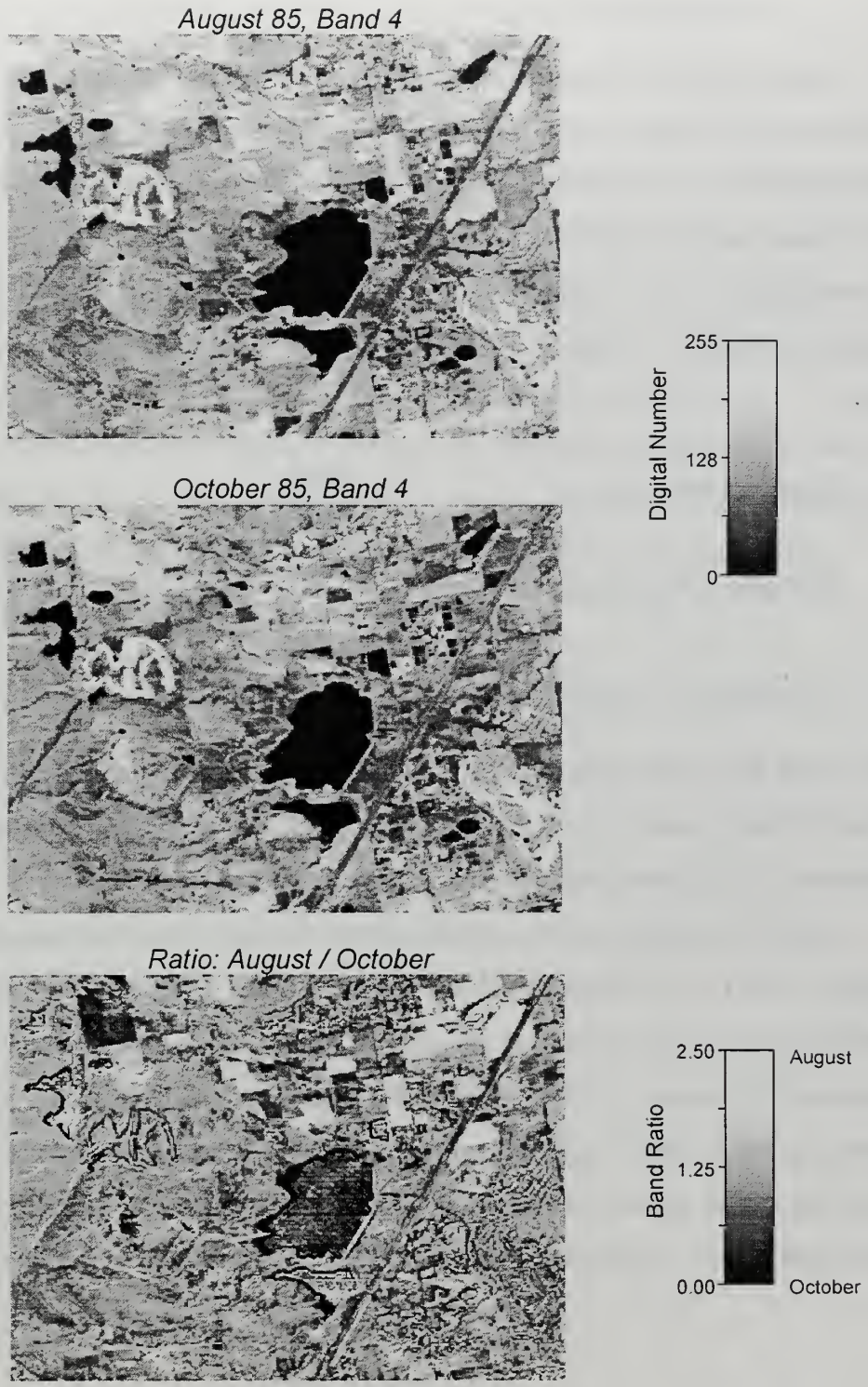

Figure 2.10: The same Band 4 images used in Figure 2.8 applied to ratioing. Note that the center of the ratio scale is not 1.0.

3. Index Differencing

Image differencing compares single bands but does not account for relationships between bands. In order to take advantage of these relationships, an index is created by combining two or more bands into one value. Tucker (1979) introduced vegetation indices which are the most widely used in remote sensing today. A vegetation index takes advantage of the IR ledge, the high radiance difference between visible and near infrared wavelengths. Tucker (1979) used Landsat MSS to create three vegetation indices:

$$\text{Ratio Vegetation Index} = \frac{\text{Band 4}}{\text{Band 2}} \tag{2.10}$$

$$\text{Normalized Vegetation Index} = \frac{\text{Band 4 - Band 2}}{\text{Band 4 + Band 2}} \tag{2.11}$$

$$\text{Transformed Vegetation Index} = \sqrt{\left(\frac{\text{Band 4 - Band 2}}{\text{Band 4 + Band 2}}\right) + 0.5} \tag{2.12}$$

Band 4 is the near infrared band (0.8 – 1.1 μm) and band 2 is the red band (0.6 – 0.7 μm). All three of these indices are commonly used today. The normalized vegetation index is often referred to as Normalized Differenced Vegetation Index (NDVI).

Index differencing is also a point-to-point operation where the indices (instead of raw pixel values) are subtracted from one another. Index differencing negates the effect of multiplicative factors acting equally in all bands such as topographic effects and temperature differences (Lillesand and Kieffer, 1987) and has the advantage of emphasizing differences in spectral response curves. The main disadvantage with index differencing is that it can enhance random or coherent noise not correlated in different bands (Singh, 1989). A generalized form of index differencing would be expressed as

$$DR_{ij} = \frac{x_{ij}^{k}(t_1)}{x_{ij}^{l}(t_1)} - \frac{x_{ij}^{k}(t_2)}{x_{ij}^{l}(t_2)} \tag{2.13}$$

Where DR_{ij} is the index difference of two ratios of bands k and l for pixel i,j of images at times t_1 and t_2.

Michener and Houhoulis (1997) used NDVI differencing for vegetation changes in flooded areas with a high degree of success. They note that, "Interpretability could potentially be facilitated by transforming raw spectral data to an appropriate ratio index that may be correlated with a specific type of change." Creating an appropriate index allows the analyst to emphasize the changes that are important which could inherently reduce erroneous detections caused by changes that are not considered significant. This technique, however, requires *a priori* knowledge about the types of changes of interest.

Figure 2.11 demonstrates NDVI differencing for the Boulder scene. The result is similar to other techniques; however, changes in vegetation are more pronounced. Of particular interest are the fields in the top right corner. The health of the fields appear to have decreased from August to October which is indicated by a low pixel value.

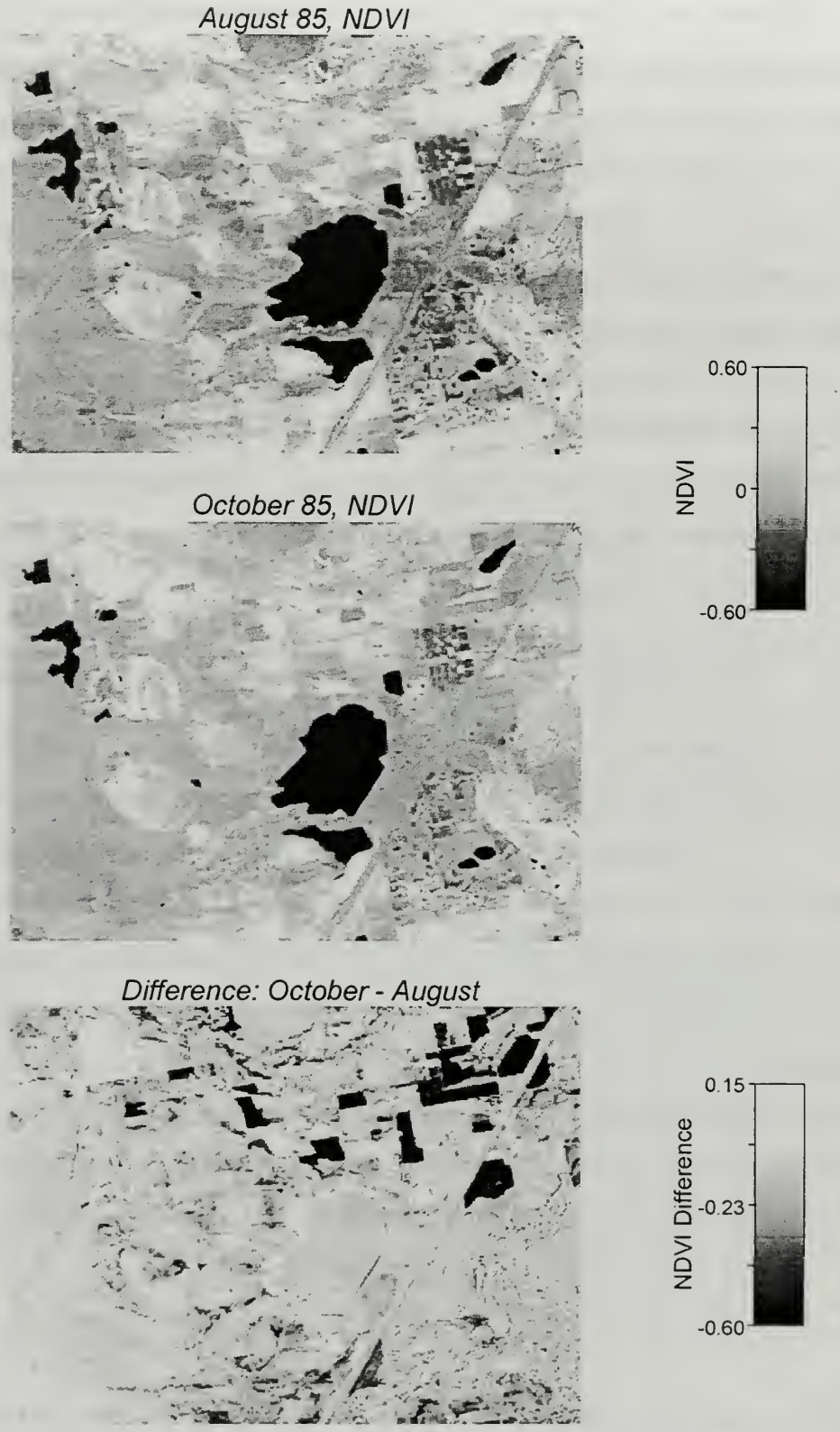

Figure 2.11: NDVI differenced image of the Boulder scene.

4. Principal Components Analysis

Several approaches to PCA are available for change detection. The first approach is the most straight forward. Each image is transformed into its principal components. Then a selected band from each image can be compared using other change detection techniques such as differencing. Figure 2.12 illustrates the progression of this method, and Figure 2.13 apply the technique to the Boulder scene.

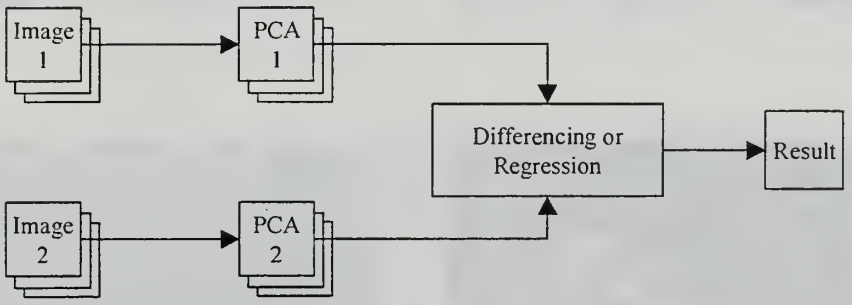

Figure 2.12. Principal components analysis where band-by-band differencing is used.

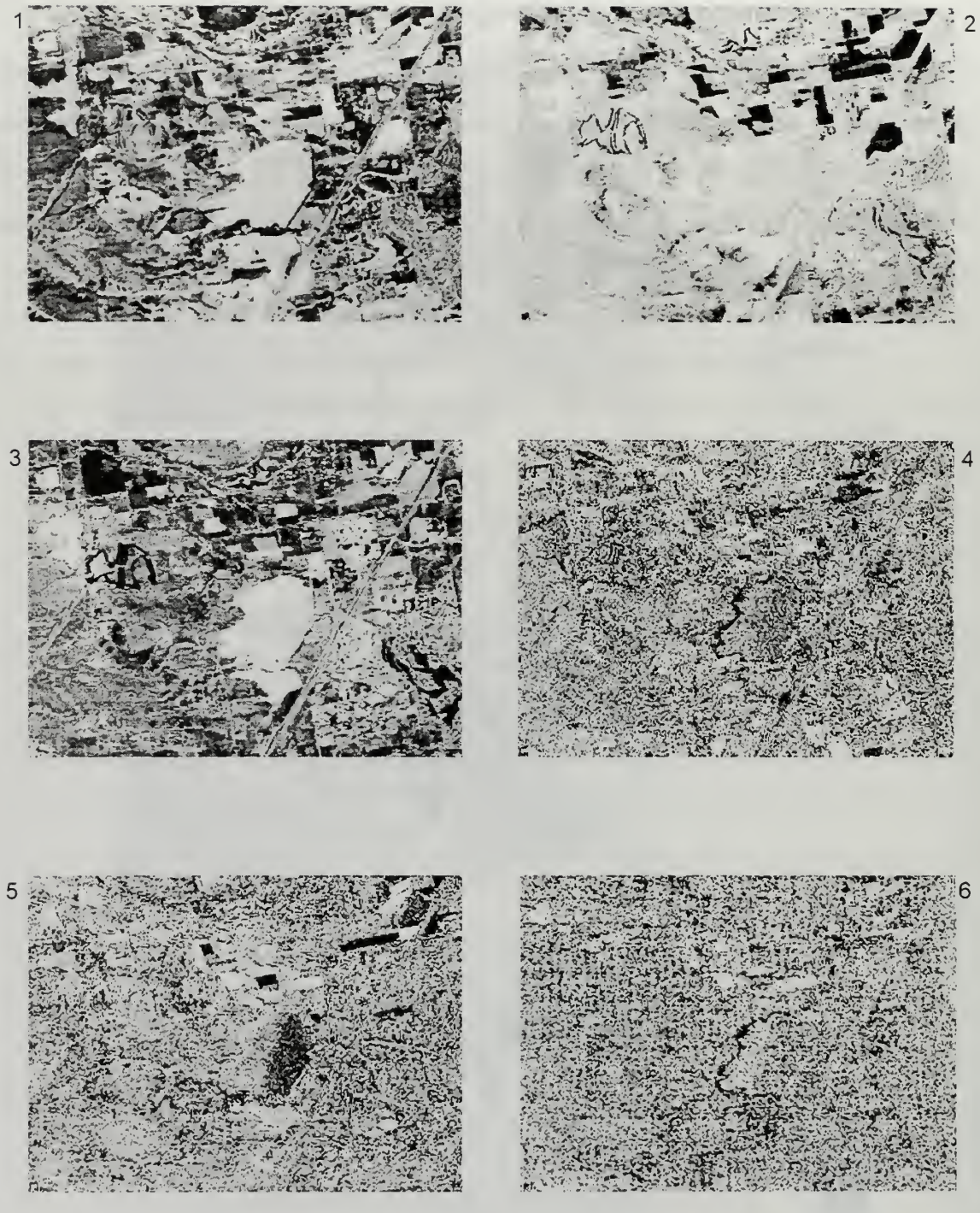

Figure 2.13: Differenced principal components bands of the Landsat Boulder image. Each band represents the difference of the August PC band from the same PC band in October.

The second approach combines both images into one data set. For instance, if both images contained three bands, the combined data set would contain six bands. The new data set is transformed into its principal components which is analyzed to determine which band contains the relevant change information (Singh, 1989). Figure 2.14 illustrates this approach. Finding the appropriate band can be difficult, but once found, will probably remain consistent for similar data sets and targets.

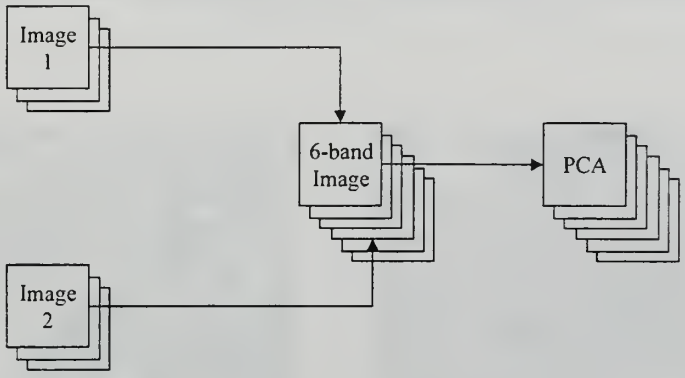

Figure 2.14. Spectral Principal Components Analysis.

Michener and Houhoulis (1997) refer to this approach as spectral principal components analysis. They applied spectral PCA to three three-band SPOT multispectral High Resolution Visible (HRV) images of pre-flood (two images) and post-flood (one image) conditions in southwest Georgia associated with Tropical Storm Alberto in July, 1994. Analysis of the eigenstructure and visual inspection of the PC bands indicated that bands 3 and 4 were attributable to infrared changes caused by the drier vegetation in the pre-flood images. PC bands 6, 8, and 9 accounted for spectral variability among the red and green bands of the three images. PC Bands 1, 2 appeared to be related to overall brightness while bands 5 and 7 were related to changes in the two pre-flood images. Applying the same procedure to the Boulder imagery produced similar results. Figure 2.15 shows the first six bands. Band 1 most closely represents visible overall radiance. Change in the lake water level and vegetation health is most evident in bands 4, and 5. Figure 2.16 shows these three eigenvectors. Each eigenvector was separated into the six bands associated with their respective dates and overlaid to allow for easier comparison.

Eigenvector 1 has all positive weights indicating that all bands have been summed together. In eigenvector 4, the first six bands have positive weights while the last six bands are mostly negative indicating the two dates have been differenced. Only Landsat band 4 (4/10) has the same weight in both images indicating that it was not used to create the change result in PC band 4. Conversely in eigenvector 5, Landsat band 4 is the only band used. In this case, PC band 5 produces a result useful in studying changes in vegetation while PC band 4 provides information regarding other changes..

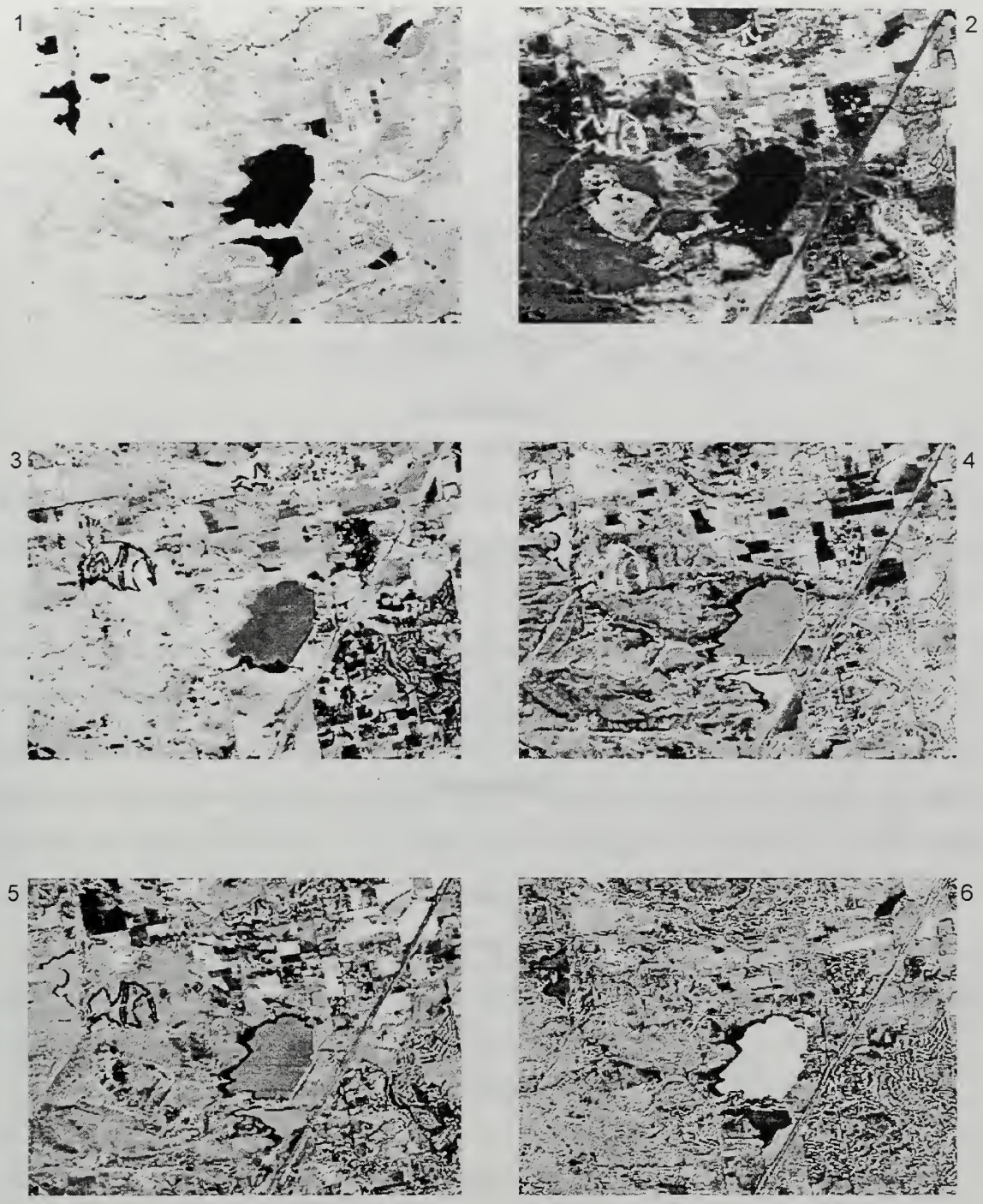

Figure 2.15: The first 6 PC bands produced by combining the two Boulder images and conducting the transform on the 12-band composite image.

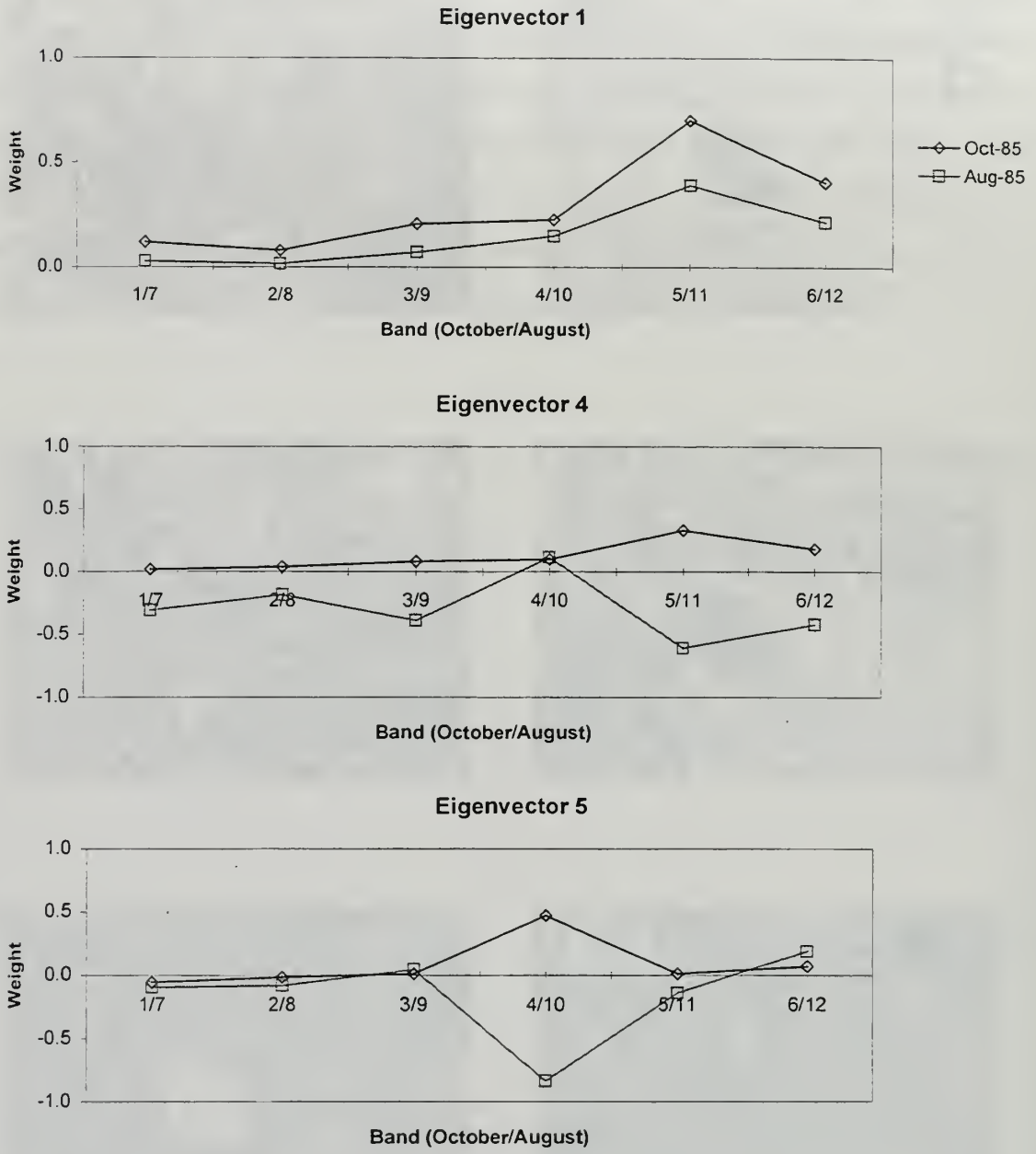

Figure 2.16: A sample of three eigenvectors for the 12-band composite image. The bands are separated into two lines by date and overlaid for a better comparison.

A third approach to PCA-based change detection is to first produce single-band index images of each image, combine the index images into one multi-band data set, and perform PCA on the new data set. Figure 2.17 illustrates this approach. Subsequent analysis of the PC bands is the same as that of the previous approach.

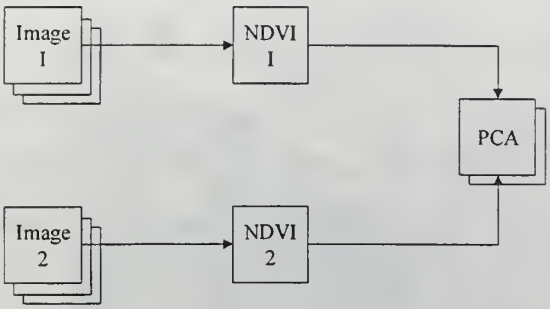

Figure 2.17. NDVI-based Principal Components Analysis.

Michener and Houhoulis (1997) apply this method to "NDVI-PCA". NDVI images were produced from the three SPOT images (two pre-flood and one post-flood). The NDVI images were merged and transformed. Further analysis showed that PC band 1 related to overall brightness in the images. PCA band 2 related to differences between pre-flood and post-flood images, and PCA band 3 related to differences between the two pre-flood images. Similar results were achieved with the Boulder scene (Figure 2.18). PC band 1 used weights of -0.789 (for the first date) and -0.614 (for the second data). The negative values caused the gray scale to invert, but since the signs are the same PC band 1 equates to overall brightness. PC band 2 uses weights of 0.614 and –0.789 which indicates that it contains the change information.

Studies indicate that PCA-based change detection does not perform as well as other simpler techniques (Singh, 1989; Michener and Houhoulis, 1997). It is also computationally intensive and requires sophisticated analyst input.

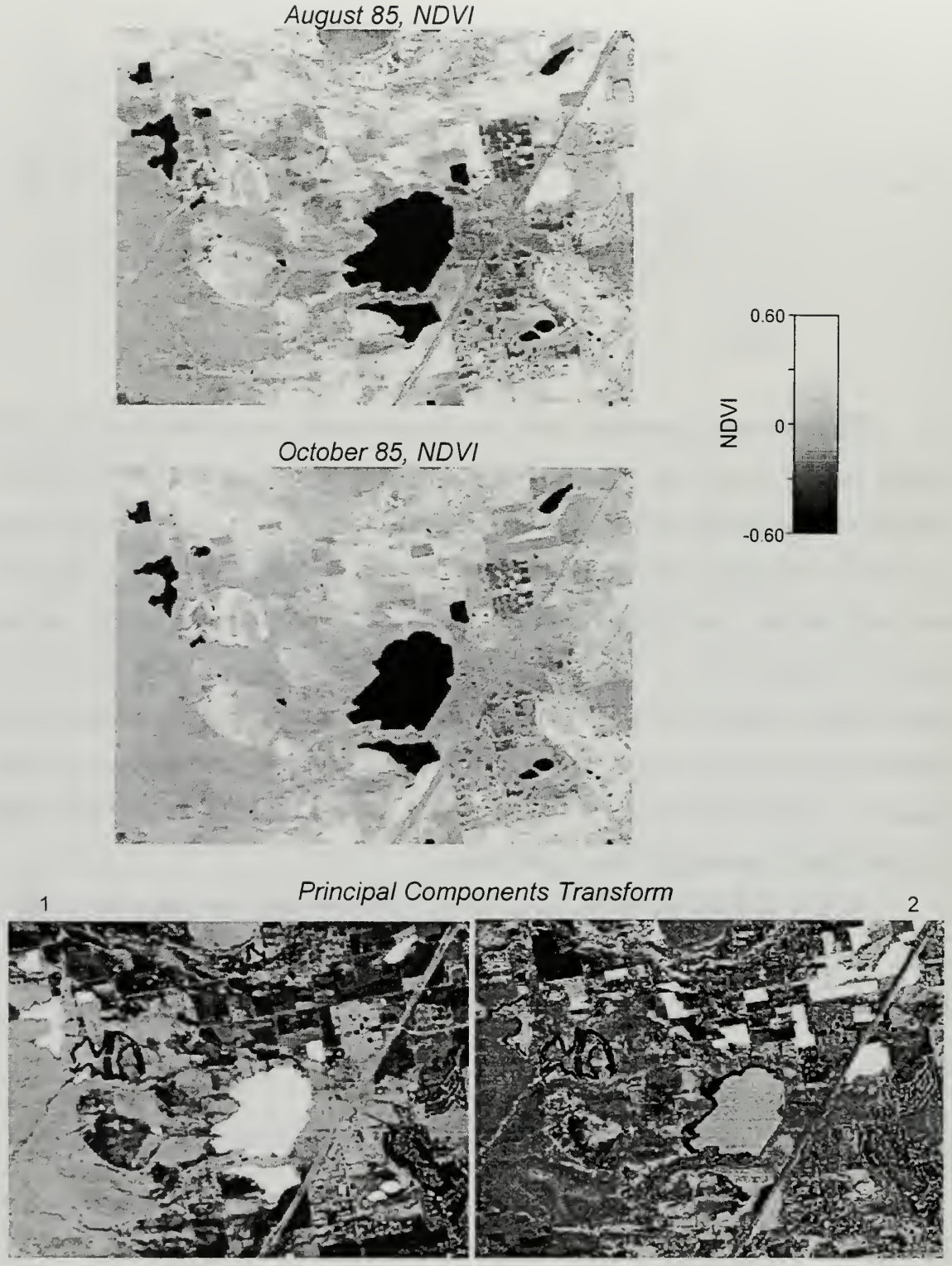

Figure 2.18: Two NDVI images combined and converted to principal components. PC band 2 identifies the areas of change.

5. Post Classification Comparison

Post classification comparison produces change maps by comparing segmented classes produced from two images (Singh, 1989). Figure 2.19 illustrates the technique. Both images undergo supervised or unsupervised classification. Similar classes from both images are differenced to produce change classes which are then merged into one result.

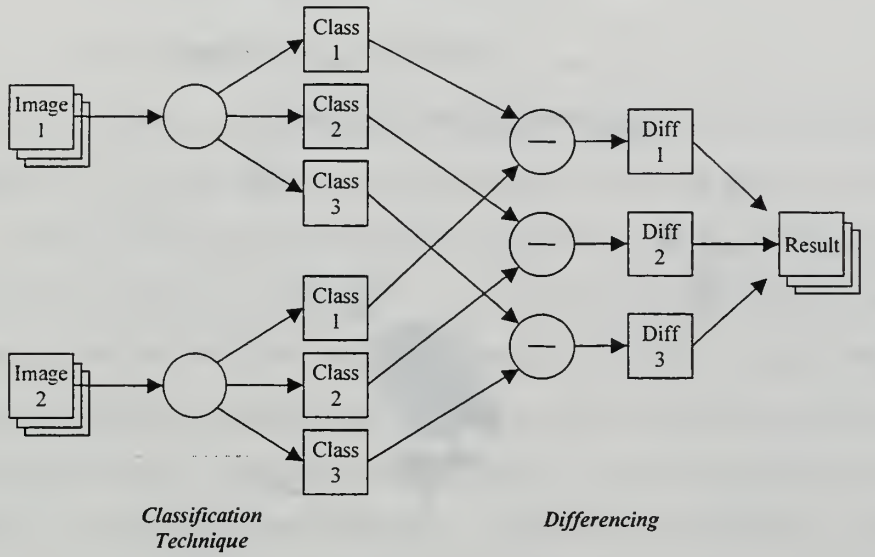

Figure 2.19: A flow diagram illustrating post classification comparison.

This technique minimizes the effects of differences in atmospheric conditions, solar angle, and sensor gain. It also reduces the need for accurate registration because the classes usually represent larger areas (Singh, 1989). It is likely, however, that registration would become more of an issue when attempting to observe smaller targets (i.e. tanks and trucks). Figure 2.20 demonstrates post classification comparison with the Boulder scene.

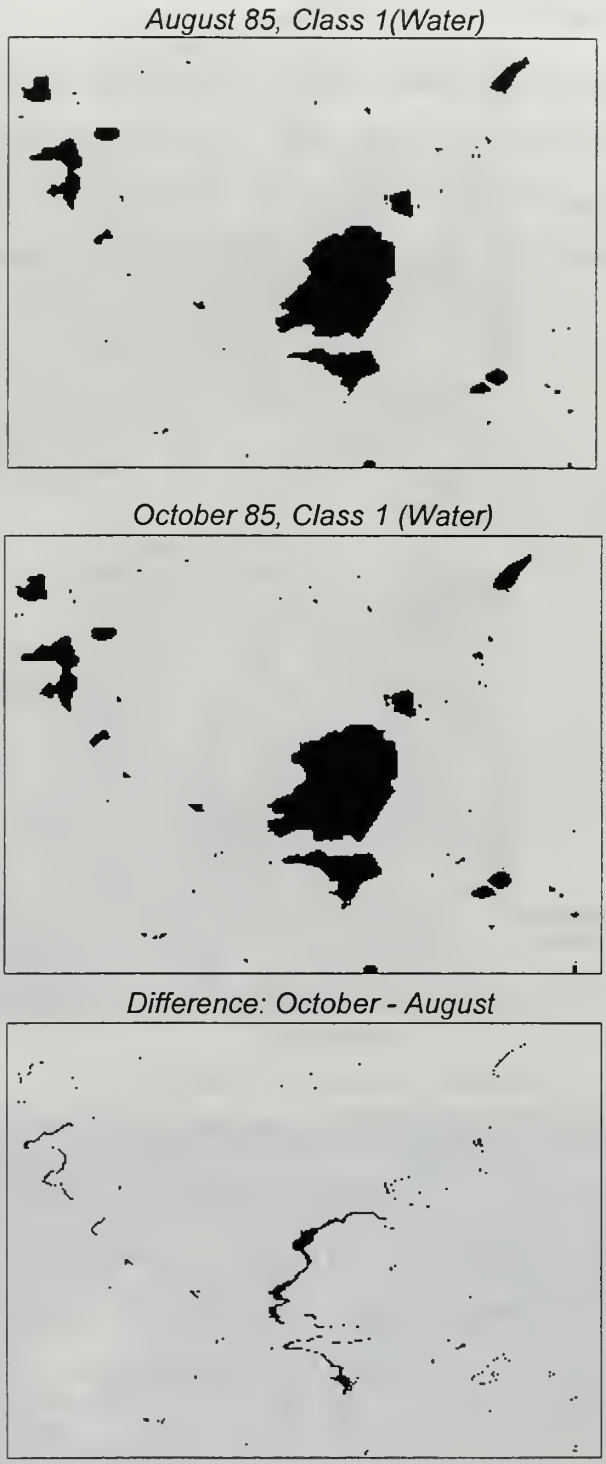

Figure 2.20: Post classification comparison as applied to the water class on the Boulder scene.

The rules of joint probability apply to post classification comparison. Errors can be multiplied through to the change result. For example, the accuracy of a particular classification technique may be 0.8 for both images. When the images are compared, the change detection accuracy becomes $0.8 \times 0.8 = 0.64$ (Singh, 1989). This multiplication of errors causes the post classification comparison to perform badly against the simpler differencing techniques. Singh (1989), found that post classification comparison performed the worst of all techniques tested with an accuracy of only 51.35%.

6. Direct Multidate Classification

Direct multidate classification, sometimes referred to as temporal change classification (TCC), supposes that spectral data from combined sets of images would be similar in areas of no change and noticeably dissimilar in areas of change (Weismiller, 1977) Multiple images are combined into one data set before applying classification. Supervised or unsupervised classification is applied to both images simultaneously.

In the supervised classification, training sets are obtained that represent areas of change and no change. The training sets are used to derive statistics that define the feature space. In unsupervised classification, an analysts must first inspect portions of the scene where known changes have occurred. Classes are then derived using cluster analysis. (Singh, 1989)

Weismiller (1977) introduced this technique for applications in coastal studies. He used clustering and layered spectral/temporal classification. Selected bands were used as input to decision functions that followed a decision tree until a change was detected. Michener and Houhoulis (1997) also employed this technique in their flood study of southwest Georgia. Three SPOT-XS images were combined into one nine-band composite image. They used an unsupervised method, iterative self-organizing data analysis (ISODATA), to generate 50 change classes. In a second approach, Michener and Houhoulis converted the three images to single-band NDVI images thus creating a three-band data set instead of the previous nine. The same unsupervised classification technique was used to produce the change classes. They found that the NDVI approach was successful in detecting changes in vegetation due to flooding, and improved the

accuracy by 6.3% over standard post classification techniques. However, multidate classification did not perform as well as differencing and PCA.

Overall, multidate classification proved to be "very complex and computationally intensive" (Singh, 1989). It has also been difficult to label change classes and redundancy in spectral information is often present in some bands (Michener and Houhoulis, 1997). Weismiller (1997) also concluded that the technique performed poorly.

Figure 2.21 demonstrates the technique with the Boulder Landsat data using ISODATA classification in ENVI. In this case, the procedure was iterated three times and seven classes were created. A color version of this figure is contained in Appendix B. Class 3 contains change information pertaining to increased vegetation such as that caused by that surrounding the receding lake. Class 7 contains change information pertaining to decreased vegetation health in the fields in the top right corner; however, this class also includes data that cannot be attributed to areas of change. Without *a priori* information, it might be difficult to discriminate areas of change in these seven classes.

Figure 2.22 illustrates how three of these classes are distributed using difference band 3 and band 4 of the October image. A color version of this figure is included in Appendix B. Class 4 represents non-natural objects that have exhibited minimal change. The scatter plot shows that there is sufficient separation of class 4 and the two change classes, 3 and 7. While difference band 3 would not be able to discriminate between classes 3 and 7, band 4 from the October image provides additional information that aids in describing the type of change that took place.

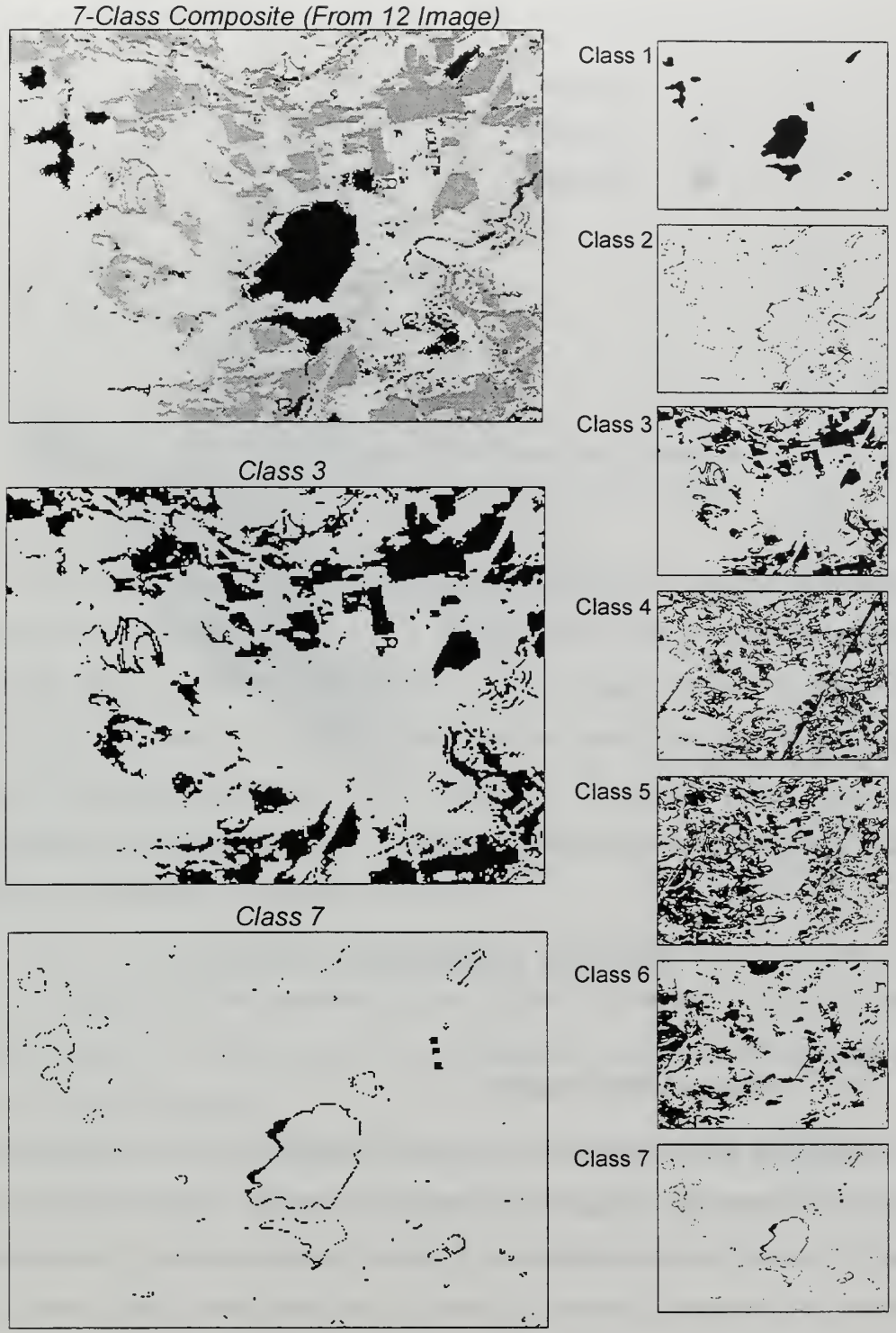

Figure 2.21: Direct multidate classification. The right side is a breakout of the various classes. Classes 3 and 7 contain change information.

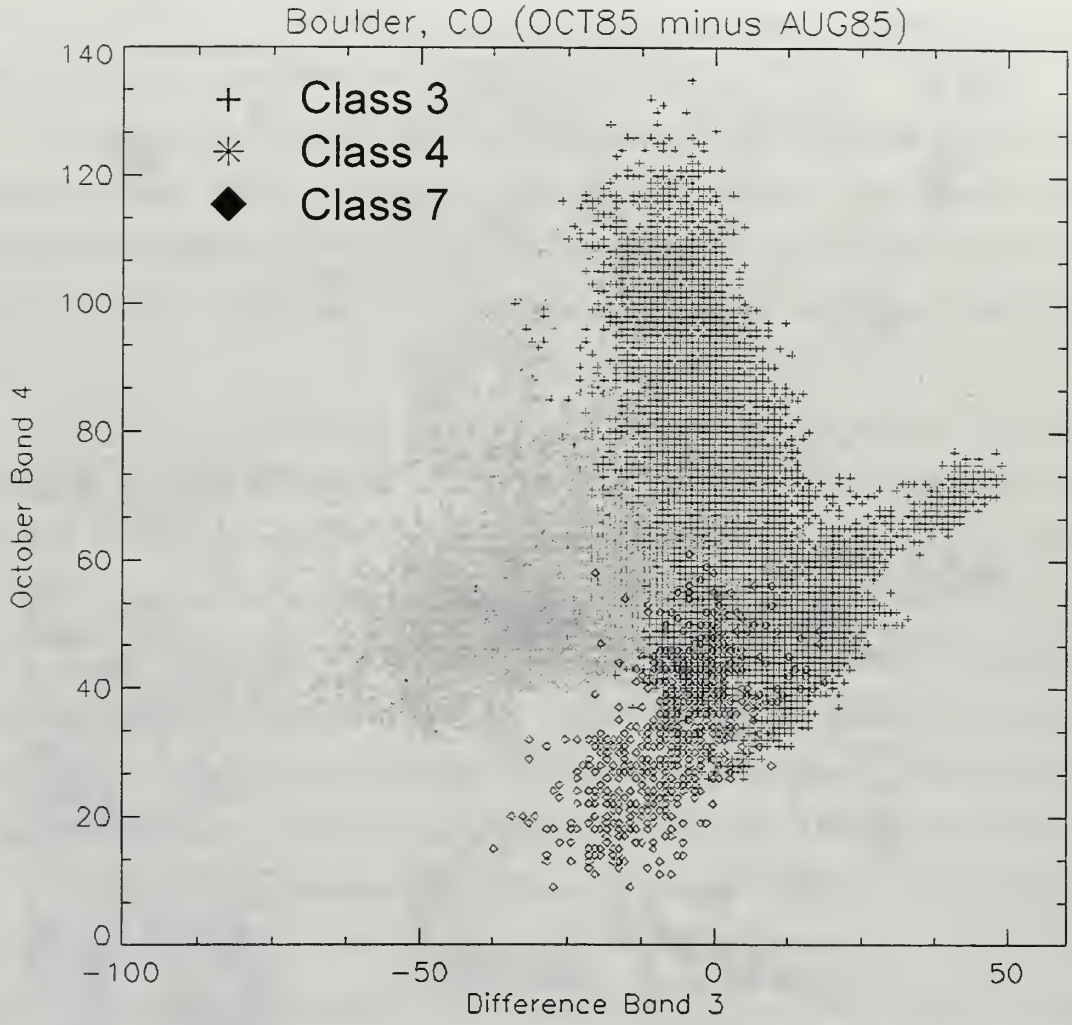

Figure 2.22: A scatter plot of three classes.

7. Change Vector Analysis

In change vector analysis, each pixel is described as a vector in N-dimensional space where N represents the number of bands in the image. This method is illustrated in Figure 2.23 using a two-band example. From two images, a change vector is derived by subtracting the vector of the image at time, t_1, from the vector of the image at time, t_2. The direction of the resultant vector contains information about the type of change that has occurred. This usually equates to spectral change. The magnitude of the resultant vector contains information about changes in radiance (Singh, 1989).

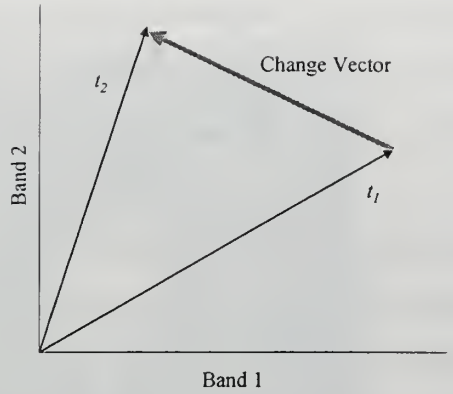

Figure 2.23. An illustration of the formation of a change vector using two-band image vectors (after Deer, 1995).

In essence, change vector analysis consists of two parts. The first is nothing more than band-by-band image differencing. A change vector can be created by making an N-band image where each band is the difference of two images of the same band. This is the only way to represent all dimensions of a change vector; however, displaying more than three dimensions is difficult – if not impossible. Since the direction of the change vector describes the type of change, it is often preferred to represent the change vector as a one-band spectral angle image.

This is similar to the spectral angle mapper (SAM) described in Section 2.2, but instead of using a reference spectrum, the dot product is obtained between both images. The final result is a change image that is dependent on spectral change and not on changes in overall brightness.

A simpler means of obtaining the same result is to use a common reference spectrum for both images in creating individual SAM results. The difference in the two SAM results is the spectral angle difference and represents spectral change. Figure 2.24 illustrates this technique on the Boulder scene using a mean vegetation spectrum as a reference. The spectral angle for each image was obtained using the vegetation spectrum. The change image shown is the difference between the two SAM results. The August and October images shown in Figure 2.24 are the individual SAM results. The vegetation closest to the mean spectrum appears dark in those images while areas spectrally different

from vegetation, like water, appear bright. The difference image shows areas of increased vegetation health as dark and decreased vegetation health as bright. It is apparent that even areas spectrally different from vegetation are cancelled if they are common in both images. The result is identical to that of obtaining the dot product between the two images.

The spectral angle difference also removes mean differences in radiance such as that associated with sensor gain differences, but since vector magnitude is not accounted for, it is possible that important changes could be missed. It may be necessary to have amplifying information from the N-band change vector image in order to conduct a full analysis.

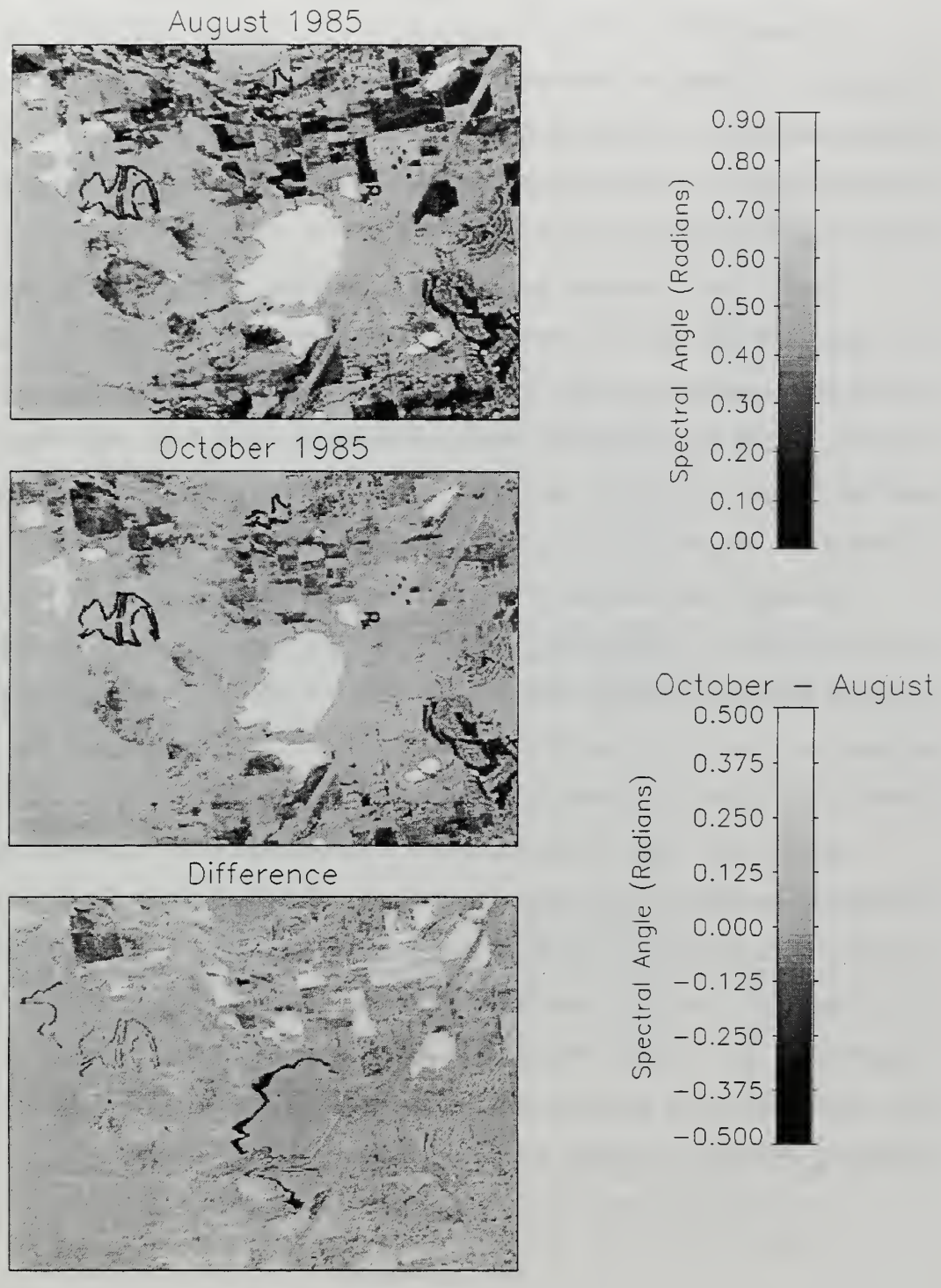

Figure 2.24: Spectral angle mapper using a mean vegetation spectrum as the reference.

8. Previous Studies

Because of the difficulty in acquiring well understood data, few studies have attempted to quantitatively determine the performance of each technique. Instead, most studies qualitatively compare techniques or study only one technique. Singh (1984, 1986) and Michener and Houhoulis (1997) have determined change detection accuracies in the context of their specific data sets.

Singh (1986) concluded that regression produced the highest accuracy followed by image ratioing and differencing. Mulitspectral classification such as post-classification comparison and direct multidate classification produced the lowest accuracy. Singh also attempted local processing (i.e. smoothing, edge enhancement, standard deviation texture) in conjunction with a variety of change detection techniques but found that they offered little or no improvement in change detection accuracy.

Michener and Houhoulis (1997) used logistic multiple regression and probability vector modeling to evaluate five techniques. They also concluded that differencing produced the highest accuracy followed by PCA. While there was little difference in accuracy between S-PCA and NDVI-PCA, NDVI-TCC performed better than S-TCC. Table 2.1 and Table 2.2 summarize the results of both studies.

Singh (1984, 1986, 1989), Michener and Houhoulis (1997) arrived at the same fundamental conclusion. They determined that various techniques yield different results and that simple techniques outperform sophisticated ones. More advanced techniques are being introduced, but as the complexity of the algorithms increase, so does the required computation. This is not a desired result since the increased dimensionality of spectral data is also driving up computational requirements. It is possible that the most useful techniques are already available, and this study focuses on those methods.

Techniques	*Accuracy (%)*
Univariate image differencing, band 2	73.16
Univariate image differencing, band 4	63.33
Image ratioing, band 2	73.71
Image ratioing, band 4	64.99
Normalized vegetation index differencing	71.05
Image regression, band 2	74.43
Low pass filtered image differencing, band 2	72.09
Background subtraction, band 2	72.32
High pass filtered image differencing, band 2	70.07
Standard deviation texture (3 x 3) differencing, band 2	69.95
Principal components, image differencing (unstandardized)	71.49
Principal component-2, image differencing (standardized)	64.32
Post-classification comparison	51.35
Direct multidate classification	57.29

Table 2.1: Summary of the best classification performance for the change detection techniques studied (from Singh, 1989). Bands refer to Landsat MSS.

	No. Dead Sites		No. Live Sites		
Method	Correct	Incorrect	Correct	Incorrect	Accuracy
(a) S-TCC	36	10	32	34	0.607
(b) NDVI-TCC	38	8	37	29	0.670
(c) S-PCA	33	13	46	20	0.705
(d) NDVI-PCA	41	5	37	29	0.696
(e) NDVI-ID	29	17	57	9	0.768

Table 2.2: Accuracy assessment of five change detection techniques used to assess vegetation response to flooding (from Michener and Houhoulis, 1997

III. THE SPATIALLY ENHANCED BROADBAND ARRAY SPECTROGRAPH SYSTEM (SEBASS)

This thesis deals with data from the thermal imaging spectrometer, SEBASS. SEBASS, under development by the Aerospace Corporation, El Segundo, CA, filled the gap in imaging spectroscopy by providing a two-channel system that collected in the MWIR and LWIR regions. The instrument (pictured in Figure 3.1) collects 128 bands in the MWIR (2.1 – 5.2 μm) and 128 bands in the LWIR (7.8 – 13.4 μm) using a bushbroom scanner (Hackwell, 1997).

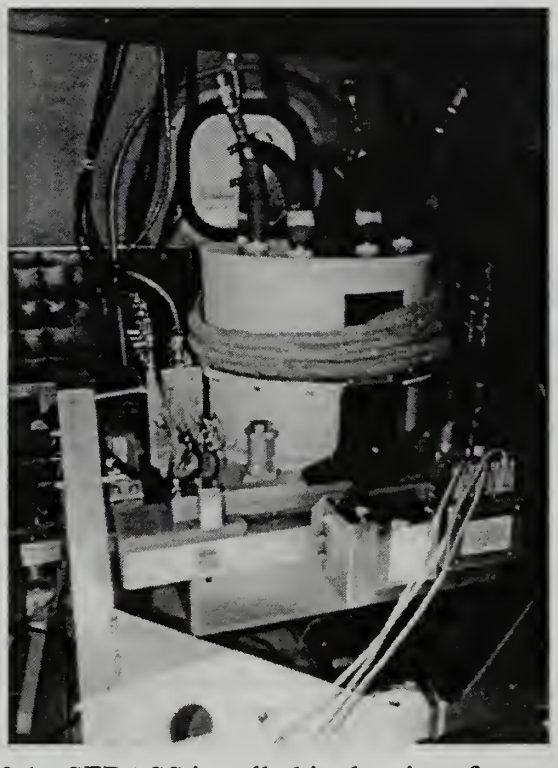

Figure 3.1: SEBASS installed in the aircraft atop the roll compensator.

A. DESIGN

SEBASS employs a pushbroom collection concept by imaging through a thin slit. Light from the slit is split to two spectrographs as depicted in the optical layout in Figure

3.2. Two spherically shaped salt (LiF for the MWIR channel and NaCl for the LWIR channel) prisms disperse the light on two 128 x 128 element silicon arsenide (SiAs) blocked impurity band (BIB) focal plane arrays (FPAs). These FPAs are placed so that one dimension of the array captures the dispersed spectrum while the other dimension captures across-track spatial information. Along-track spatial information is collected in all bands simultaneously as the sensor moves in the direction indicated by Figure 3.3. Each element on the array has an instantaneous field of view (IFOV) of 1 mrad (0.057°). This provides a 128 mrad (7.30°) total field of view (FOV). The ground sample distance (GSD) for a typical altitude of 6000 feet is 6 feet.

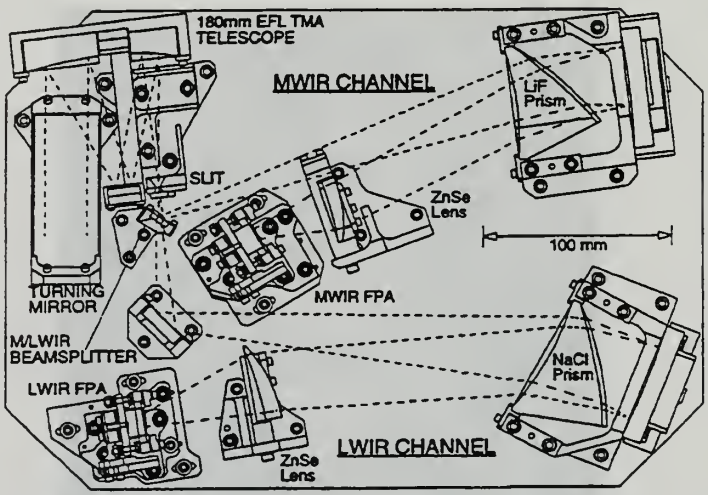

Figure 3.2: The SEBASS optical layout (From Hackwell, 1997)

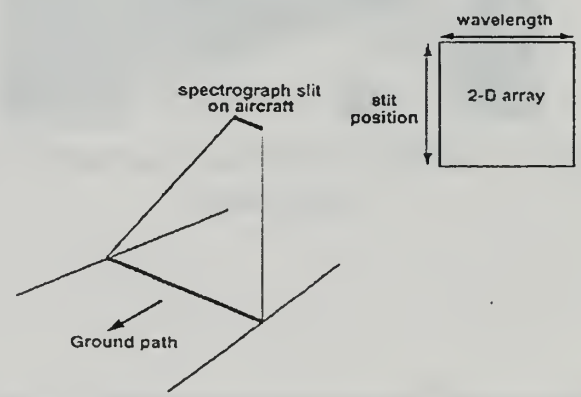

Figure 3.3: The SEBASS FPA configuration (From Hackwell, 1997).

Spectral resolution, the spacing between the center wavelengths for each band, varies across both the MWIR and LWIR arrays (see Figure 3.4). The MWIR spectral resolution varies from 0.064 μm at the low edge to 0.014 μm at the high edge. Likewise, the LWIR spectral resolution varies from 0.070 to 0.040 μm (Smith and Schwartz, 1997).

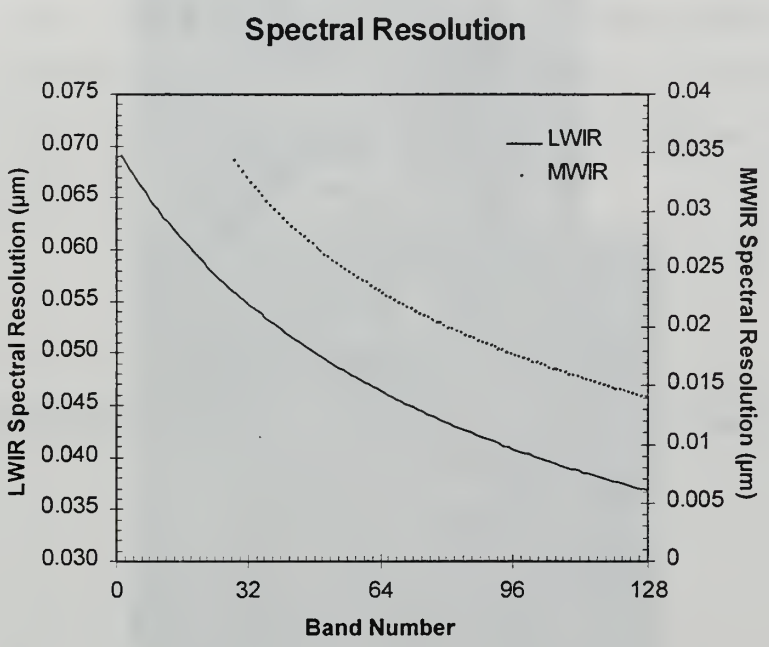

Figure 3.4: A plot of the band width of each spectral band for the LWIR channel.

Each FPA has a maximum acquisition rate of 240 Hz; however, at least two consecutive frames must be coadded to achieve an acceptable SNR. Therefore, the maximum frame rate for SEBASS is 120 Hz. This is adjustable to achieve a desired SNR or to account for major differences in aircraft speed and altitude.

The sensitivity of the sensor is improved by cooling it to 4°K in a helium-cooled dewar (Figure 3.5). The FPAs are then heated to 11°K for improved temperature stability. This provides a single frame noise equivalent spectral radiance (NESR) of 1.0 $\mu W/cm^2$ sr μm (μ flick) in both channels. Coadding frames reduces the NESR. For example, 240 coadds improves the NESR to 0.2 μ flicks (Hackwell, 1997). Figure 3.6 is a plot of the NESR for calibration runs of two flights.

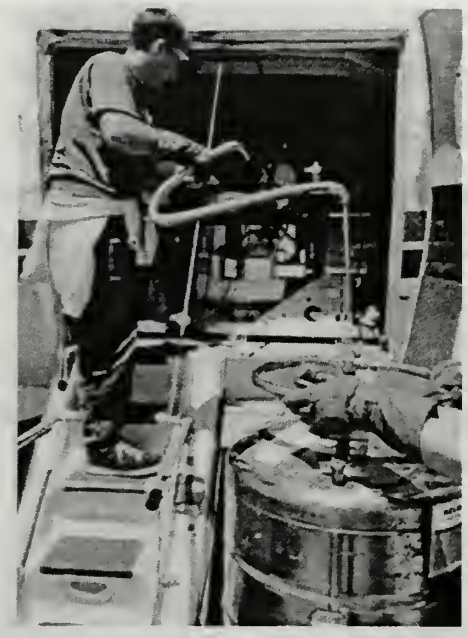

Figure 3.5: The flight crew maintains a sufficient liquid helium level to keep the FPAs at 11°K.

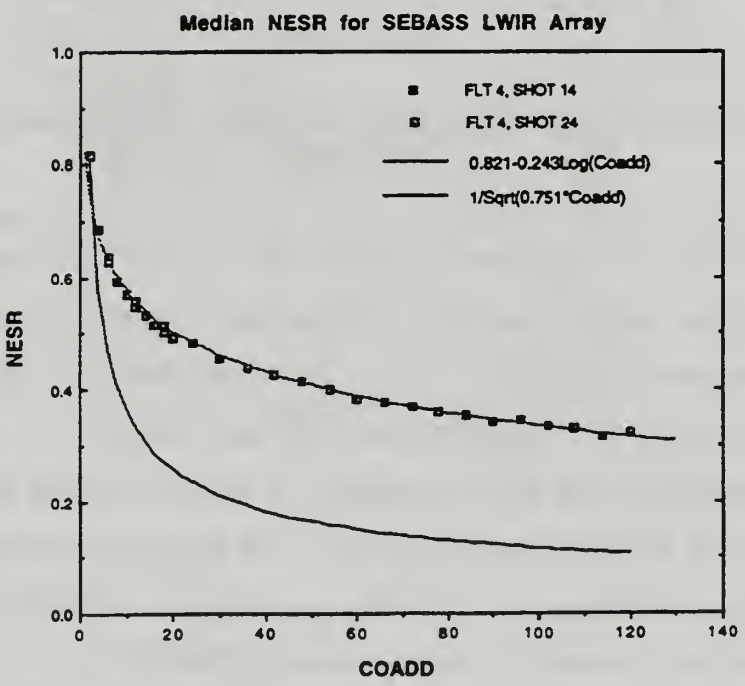

Figure 3.6: The effects of coadding frames on the noise equivalent spectral response (from Hackwell, 1997).

The instrument is operated in flight by a Sun SPARCstation 20. The flight crew monitors data collection from a waterfall display on the SPARC20 monitor. Figure 3.7 is a photograph of the SEBASS control console installed in the aircraft. The waterfall output is dispayed on the top monitor. The two LCD monitors provide attitude and status information as well as video output from a forward-looking video camera. Roll correction is provided mechanically by a 1 Hz roll compensator. This adequately reduces low frequency roll errors, but high frequency errors (above 1 Hz) are not corrected. Pitch and yaw errors are not corrected.

Figure 3.7: The flight crew monitors SEBASS status and operation from this console.

Initially, the data are collected in 4 byte integer format with a 64 Kb embedded binary header. They are converted to 4 byte floating point during preprocessing. The data are oriented as band-interleave by pixel (BIP) such that the spectral dimension is read first, then the across-track spatial dimension, and finally the along-track (temporal)

dimension. Data values are often represented as $N(i, j, k)$ where i, j, and k represent the spectral band, across-track position, and along-track position respectively.

B. CALIBRATION

Raw sensor data are stored on two hard disks (18 gigabytes total) onboard the aircraft. After a collect, the data are downloaded to a SparcUltra 2 and stored on either of two 20 GB hard disks. The data must be calibrated spectrally and radiometrically before it is useful to the user. The instrument has been altered since the initial work reported by Collins (1996) and some of the details in the material given here will differ from the earlier report.

1. Spectral Calibration

Spectral calibration is the process of determining the center wavelength of the energy that falls on each pixel in the array. The distribution of the spectrum is neither linear across the array nor constant over time, so it is necessary to calibrate the sensor periodically - usually prior to a collection exercise.

The dispersive properties of the prisms in SEBASS cause the image of the slit aperture to curve slightly at the focal plane. This curvature varies with position along the slit. The spectrum undergoes a similar phenomenon in which the wavelength shifts along the in-track (wavelength) dimension of the array. Figure 3.8 and Figure 3.9 depict the shape and magnitude of the slit and spectral curvature. In either case, the variation is less than one pixel. Both slit and spectrum curvature are corrected through the wavelength calibration which applies a two-dimensional second-order polynomial function to determine the center wavelength at each pixel position (Johnson, 1997).

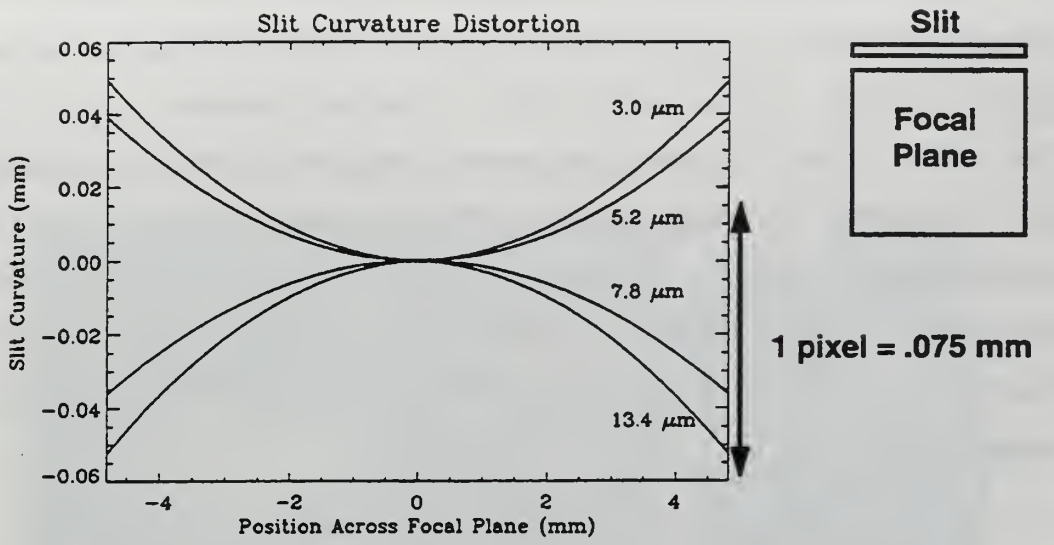

Figure 3.8: This graph depicts the shape of the slit image at the FPAs for four wavelengths. The variation is less than one pixel. The FPA diagram (right) orients the array. (From Hackwell, 1997)

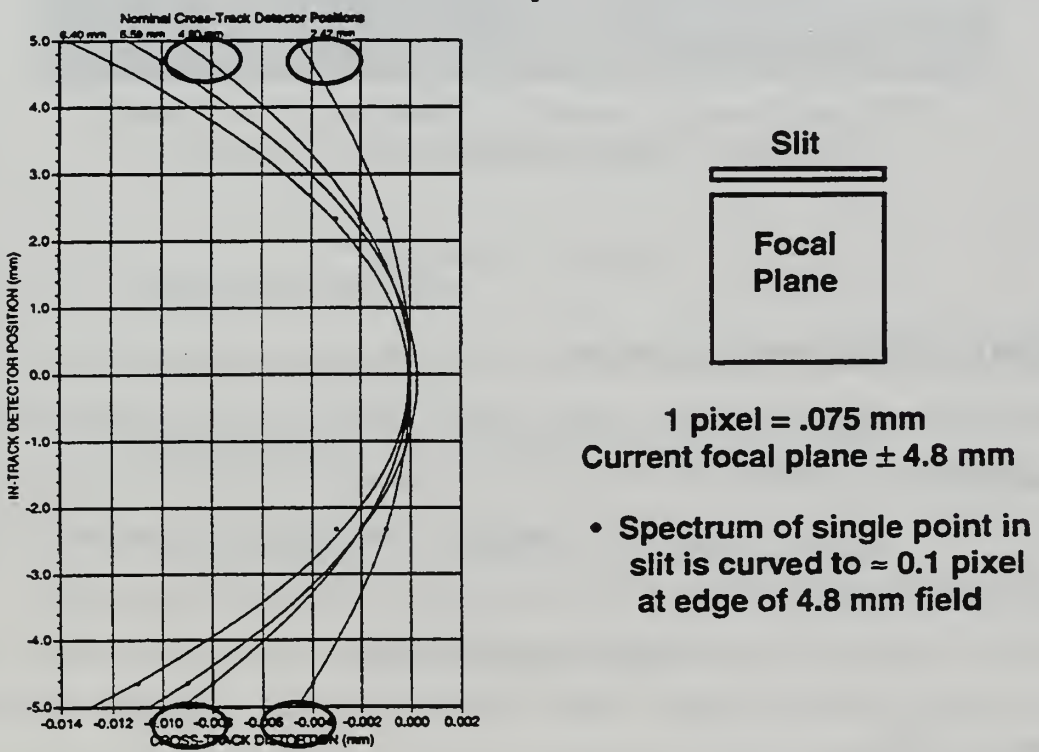

Figure 3.9: This graph depicts the shape of the slit image across the spectral dimension. The FPA diagram (right) orients the graph. (from Hackwell, 1997)

Polymer films are used as calibration standards for the LWIR wavelength calibration (Figure 3.10). SEBASS first acquires a 256-frame data set of hot and cold blackbody sources, and then acquires similar images after placing one of the polymer films in front of the slit aperture. The measured transmittance spectrum of the polymer film is the ratio of the images with and without the film (Collins, 1996). A similar technique is used for the MWIR channel, but instead of polymer films, a xenon reference lamp is used. The location of known absorption bands from the image are compared with observed values from the FPA. A wavelength map is generated using the following equation:

$$\lambda(i,j) = \sqrt{A_2(i)j^2 + A_1(i)j + A_0(i)} \tag{3.1}$$

where the coefficients $A_n(i)$ are functions of the spatial index, *i*, and for the LWIR channel are given as:

$$A_0(i) = 5.795215 \times 10^{1} - 2.357859 \times 10^{-2} i + 1.222431 \times 10^{-4} i^2 \tag{3.2}$$

$$A_1(i) = 1.042670 \times 10^{0} - 1.700715 \times 10^{-5} i + 2.397566 \times 10^{-7} i^2 \tag{3.3}$$

$$A_0(i) = -1.419449 \times 10^{-4} \tag{3.4}$$

and for the MWIR channel, are given as:

$$A_0(i) = 3.123135 \times 10^{0} + 4.640077 \times 10^{-4} i - 2.853933 \times 10^{-5} i^2 \tag{3.5}$$

$$A_1(i) = 2.227641 \times 10^{1} + 3.827485 \times 10^{-6} i + 6.551992 \times 10^{-8} i^2 \tag{3.6}$$

$$A_0(i) = -3.186248 \times 10^{-4} \tag{3.7}$$

(Johnson, 1997).

The spectral calibration only documents the position of the center wavelength for each pixel. While this is sufficient for most spectral analyses, some approaches may require the removal of the spectral curvature. To do this, the image is resampled spectrally using a cubic spline interpolator (Smith and Schwartz, 1997).

Figure 3.10: The polymer film is inserted in place for the LWIR wavelength calibration.

2. Radiometric Calibration

Two Santa Barbra Infrared (SBIR) blackbody sources are used during flight to provide calibration data of SEBASS between shots. The blackbodies are maintained at 23.5C and 35.0 °C to provide hot and cold sources for the calibration encompassing the range of temperature values expected in the scene.

The Aerospace Corporation upgraded the FPAs in SEBASS which has eliminated early problems with sensor nonlinearity concerning radiometric calibration. This has simplified calibration to a two-point linear scheme. Before this linear scheme can be implemented, a spectral radiance truth map is computed for each calibration source. This is given as

$$L_C(i,j) = L_{BB}\left[\lambda(i,j), T_C\right] \tag{3.8}$$

$$L_H(i,j) = L_{BB}\left[\lambda(i,j), T_H\right] \tag{3.9}$$

where $\lambda(i,j)$ is the instrument wavelength map (from Equation 3.1), T_C is the cold blackbody temperature (°K), and L_{BB} is the Planck blackbody function (from Equation 2.5).

To provide a low-noise data set for the blackbody calibration measurements, the frames (in the k dimension) are averaged together to reduce the measurement to two dimensions:

$$N_C(i,j) = \frac{1}{N_k}\sum_{k}^{K-1} N_C(i,j,k) \tag{3.10}$$

and

$$N_H(i,j) = \frac{1}{N_k}\sum_{k}^{K-1} N_H(i,j,k) \tag{3.11}$$

where $N(i,j,k)$ represents the original K calibration measurements and $N(i,j)$ represents the frame-averaged calibration data which is used for radiometric calibration.

The spectral radiance truth maps are applied to the radiometric calibration which is given as:

$$L(i,j,k) = G(i,j)N(i,j,k) + O(i,j) \tag{3.12}$$

where $N(i,j,k)$ is the original uncalibrated scene data, $G(i,j)$ is the sensor calibration gain given as:

$$G(i,j) = \frac{L_H(i,j) - L_C(i,j)}{N_H(i,j) - N_C(i,j)} \tag{3.13}$$

and $O(i,j)$ is the sensor calibration offset given as:

$$O(i,j) = \frac{N_H(i,j)L_C(i,j) + \left[-N_C(i,j)\right]L_H(i,j)}{N_H(i,j) - N_C(i,j)} \tag{3.14}$$

(Smith and Schwartz, 1997).

The result is data calibrated for radiance *at the sensor*. If it is necessary to have the data calibrated for ground radiance, then atmospheric calibration such as the plastic ruler method (Chapter 2) must also be applied.

C. CHARACTERISTICS

1. Thermal Drift

SEBASS experiences a slight thermal drift that occurs during operation. With the previous FPAs, this drift was nonlinear and required an exponential interpolation (Collins, 1996). The current FPAs exhibit linear characteristic, therefore, the drift can be corrected using linear interpolation. Runs are invalidated if the thermal drift rate exceeds a given threshold, but unacceptably high drift rates seldom occur.

2. Unresponsive Detectors and Pixel Slip

Of the 32,768 detectors in the FPAs, 30 are known to be unresponsive. Table 3.1 and Table 3.2 list the locations of the unresponsive pixels. If not corrected, these elements exaggerate the NESR and make radiometric calibration inaccurate. Various interpolation schemes are used to remove them from the data. For normal aerial operations, linear interpolation corrects the unresponsive pixel using two adjacent pixels in the across-track (j) dimension (Hackwell, 1997). During CARD SHARP, SEBASS made four scans of the target area where the instrument was moved 1 mrad in the across-track direction between each scan (Smith and Schwartz, 1997). The additional dimensionality of the data was reduced by applying a median filter which interpolated the data in the temporal dimension. In either case, the result is similar, and the unresponsive elements do not affect the data.

Bad Detector Element Number	Spatial (*i*) Location (1-128)	Spectral (*j*) Location (1-128)
1	75	18
2	80	23
3	81	23
4	44	47
5	118	58
6	118	59
7	118	73
8	119	63
9	9	74
10	10	74
11	113	91
12	48	100
13	104	103
14	19	106
15	20	106
16	125	120

Table 3.1: Unresponsive LWIR detectors (From Smith and Schwartz, 1997).

Bad Detector Element Number	Spatial (*i*) Location (1-128)	Spectral (*j*) Location (1-128)
1	21	27
2	22	27
3	63	28
4	16	42
5	102	43
6	102	44
7	56	47
8	51	65
9	110	69
10	49	72
11	117	110
12	13	111
13	14	111
14	14	112

Table 3.2: Unresponsive MWIR detectors (From Smith and Schwartz, 1997).

IV. DATA COLLECTION

The change detection algorithms tested in this study were applied to two data sets. Images on multiple dates from the Capabilities and Requirements Demonstration for the SEBASS High Altitude Reconnaissance Project (CARD SHARP) were used because the sensor was terrestrial based during the demonstration providing stable images with nominally high SNR. No geometric corrections or registration were required for these data. The second data set consisted of images taken at multiple times during the same day of Camp Pendleton Marine Corps Air Station. These data were collected in flight and contain the artifacts associated with aerial collects. These latter data illustrate the shortcomings of change detection in realistic scenarios.

A. CARD SHARP

In October, 1996, the Environmental Research Institute of Michigan (ERIM), in conjunction with The Aerospace Corporation conducted the Capabilities and Requirements Demonstration for the SEBASS High Altitude Reconnaissance Project (CARD SHARP). The primary goal of CARD SHARP was to demonstrate the utility of MWIR and LWIR imaging spectrometry for detecting camouflaged targets in a vegetated environment (Smith and Schwartz, 1997). CARD SHARP was jointly sponsored by the U. S. Air force Wright Laboratories, (WL/AAJS), the Central MASINT Technology Coordination Office (CMTCO), the U. S. Army Missile Command (MICOM), the Naval Research Laboratory (NRL), and the Hyperspectral MASINT Support to Military Operations (HYMSMO) Program.

From 9 October 1996 through 17 October 1996, SEBASS recorded MWIR and LWIR measurements at the Redstone Arsenal in Huntsville, Alabama. The instrument was mounted on a 300 foot tower in a panoramic configuration such that each scan could be made by steering the sensor azimuthally using a rotating mirror. Comparing this to the aerial pushbroom configuration, azimuth equates to the along-track dimension (j) while

elevation equates to the across-track dimension (k). High counting statistics were attained by using relatively large numbers of samples (coadds) compared to those typically attainable during airborne collects.

The CARD SHARP collection was intended to demonstrate target detection in a concealed, vegetation environment. Both U. S. and foreign military equipment were deployed in the collection area. Foreign equipment included a ZIL-131 transport, a T-72 tank, a BTR-70 armored personnel carrier (APC), an SA-13 GOPHER surface-to-air missile (SAM), and an SA-4 GANEF SAM. U.S. equipment includes an M1E1 main battle tank (MBT), an M2 Bradley APC, an M35 2.5-ton truck, an M60A3 MBT, and an M60A2 MBT.

1. The Collection Scenario

Three target deployments were conducted during the demonstration – each with a set of scenarios. Based on target availability and the type of scenarios, the target deployments occurring at sites S1 and S2 were chosen for our purposes. S1 and S2 were adjacent to each other and were included together in the same images. S1 contained U.S. equipment while S2 contained foreign equipment. SEBASS collected both sites on 10 October 1996 and 11 October 1996. During scenario 1, collected on the 10th, all targets were concealed using the appropriate camouflage, concealment, and deception (CC&D) techniques. During scenario 2, collected on the 11th, the CC&D was removed while leaving the equipment in place. The subtle changes that these scenarios provide make them well suited for testing change detection algorithms. Figure 4.1 is a photograph showing the positions of sites S1 and S2 with respect to the SEBASS field of view. A color version of this figure is available in Appendix B.

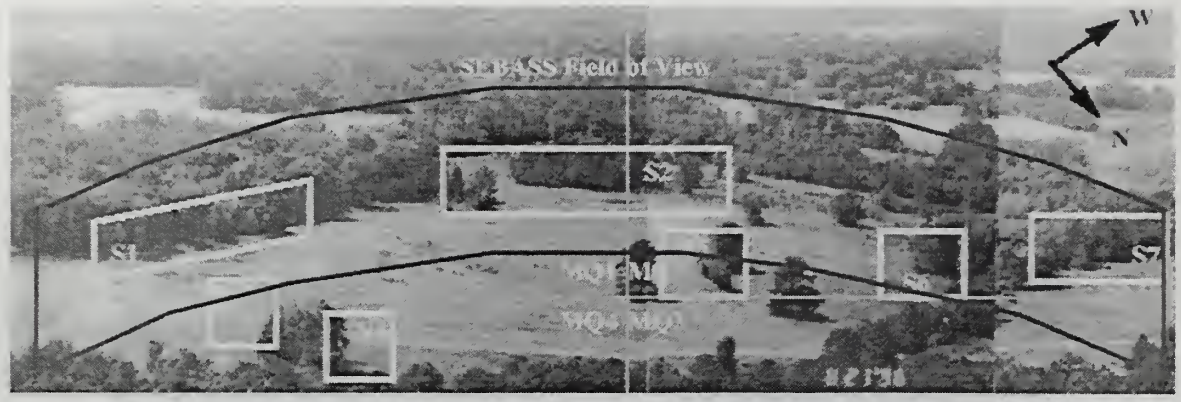

Figure 4.1: Site layout at Redstone Arsenal (from Smith and Schwartz, 1997).

The SEBASS field of view also contains sites S6 and S7. Activity in these areas includes the deployment of a Hawk surface-to-air missile, an M-35 truck, a distribution van, and an SA-4 surface-to-air missile. These vehicles are not directly connected to scenarios 1 and 2, but any activity taking place during the scenarios was still considered in this study. Figure 4.2 identifies the vehicle positions using a SEBASS band 64 image acquired on 11 October 1996 when the vehicle were uncamouflaged. Figure 4.3 and Figure 4.4 are photographs of the M1E1 MBT during scenario 1 (camouflaged) and scenario 2 (uncamouflaged). Color versions of Figure 4.2, Figure 4.3, and Figure 4.4 can be found in Appendix B. Table 4.1 lists the location and activity of each vehicle during each scenario.

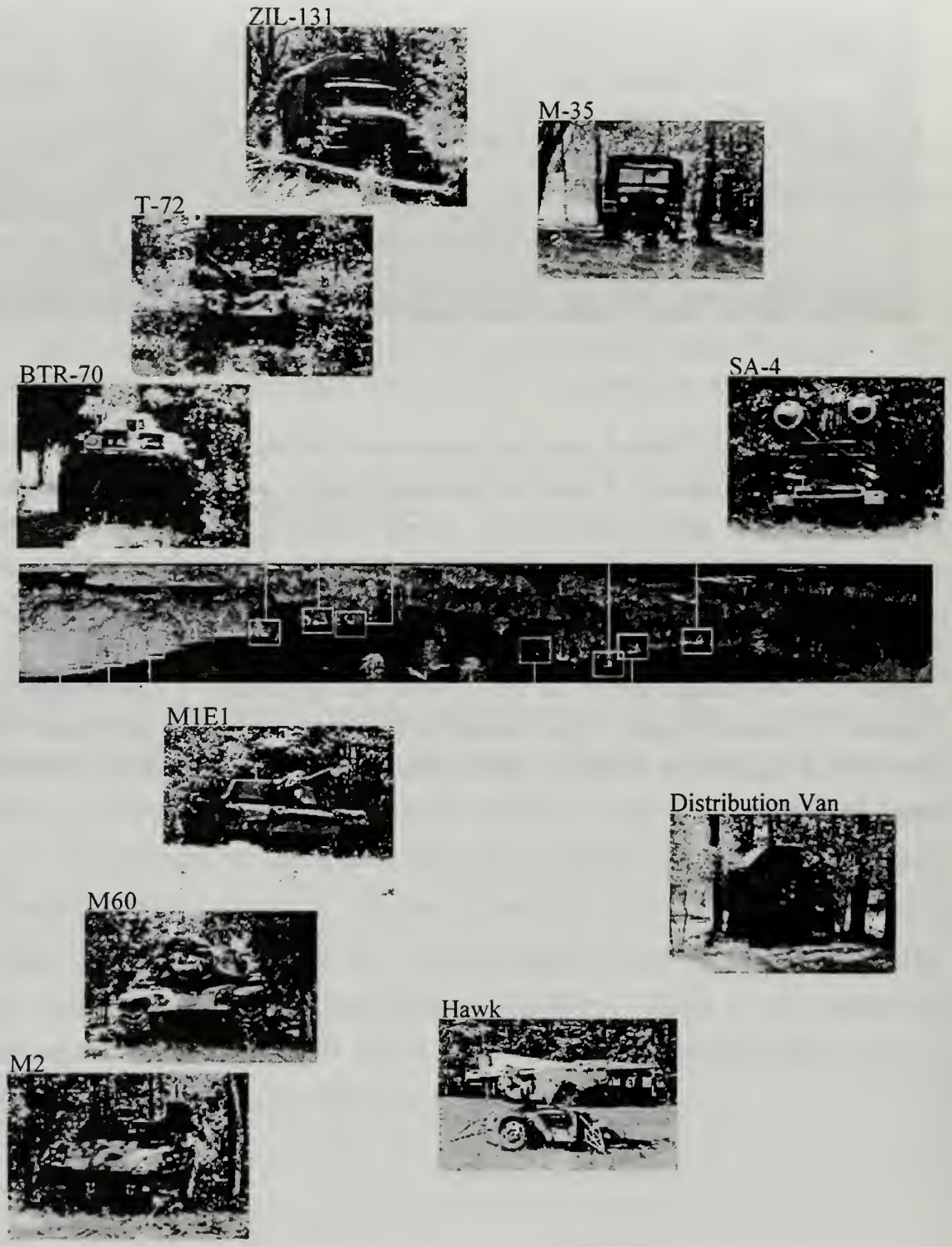

Figure 4.2: Vehicle positions in the CARD SHARP field of view.

Figure 4.3: The M1E1 Abrams MBT positioned at site S1 with woodland camouflage.

Figure 4.4: The M1E1 Abrams MBT positioned at site S1 without camouflage.

Scenario Time/Date	Site	Vehicle Description	CC&D
Scenario 1			
2200 10-9-96 thru 1400 10-10-96	S1	M1E1 Abrams MBT	LCSS woodland
2200 10-9-96 thru 1400 10-10-96	S1	M60A3 MBT	LCSS woodland
2200 10-9-96 thru 1400 10-10-96	S1	M2 Bradley APC	LCSS woodland
2200 10-9-96 thru 1400 10-10-96	S2	T-72 MBT	British with thermal blankets
2200 10-9-96 thru 1400 10-10-96	S2	BTR-70 APC	West German woodland
2200 10-9-96 thru 1400 10-10-96	S2	ZIL-131	East German woodland
Scenario 2			
1400 10-10-96 thru 1100 10-11-96	S1	M1E1 Abrams MBT	none
1400 10-10-96 thru 1100 10-11-96	S1	M60A3 MBT	none
1400 10-10-96 thru 1100 10-11-96	S1	M2 Bradley APC	none
1400 10-10-96 thru 1500 10-13-96	S2	T-72 MBT	none
1400 10-10-96 thru 1500 10-13-96	S2	BTR-70 APC	none
1400 10-10-96 thru 1500 10-13-96	S2	ZIL-131	none

Table 4.1: Location and description of equipment for scenarios 1 and 2 (after Smith and Schwartz, 1997).

2. Data

Scans for both days began and ended at the same azimuth to eliminate the need for registration. Each scan consisted of 1000 lines (57.3° azimuthal FOV). In order to exclude unresponsive sensor elements from the data set, four scans were acquired for each measurement. Each scan was offset in elevation by the instrument's IFOV (1 mrad). During preprocessing, the four scans were combined using a median filter. The final LWIR hypercubes consisted of 128 bands by 131 pixels (elevation) by 1000 pixels (azimuth).

While both MWIR and LWIR channels were available, only the LWIR hypercubes were used in this study. To minimize noise, 20 frames were coadded for each scan. Merging the four scans using the median filter technique further minimized noise creating the effect of coadding 80 frames. The instrument scan rate was 12 Hz and took 83.3 seconds to complete each scan. Preprocessing consisted of calibrating the data to at-sensor radiance in accordance with Chapter 3 of this thesis. Calibration source data files were not available for accurate atmospheric correction using the plastic ruler method.

Because the data were collected on a stable platform, they do not contain the typical problems associated with aerial collection (i.e. roll error, vibration, noise, coadd constraints). Furthermore, the demonstration was well executed with numerous target types all concealed in a challenging, vegetated scene. This provided an ideal setting for testing change detection techniques.

B. MCAS CAMP PENDLETON

On 10 December 1997, data from Camp Pendleton MCAS was collected to provide a realistic data set for change detection. This site was well suited because recent ground truth information was available from EXERCISE KERNEL BLITZ conducted at Camp Pendleton from 10 June 1997 to 7 June 1997. It also provides a busy, military-urban scene with which to test a variety of techniques. Much of the activity entails the

movement of large equipment, such as helicopters, which also may allow the use of change detection to discriminate different types of thermal scarring.

1. Collection Parameters

On 10 December 1997, troops at Camp Pendleton MCAS were conducting training exercises. The SEBASS flight crew were permitted to collect on the LCAC facility, air field, and train depot before (1000) and after (1400) the training exercises. No coordination took place between the flight crew and marine units. The expectation was that the activity between the two collects would be sufficient to provide a change-rich scene.

All flight operations were restricted to 3000 feet. This provided a nominal GSD of 3 feet (0.9 meters) and an swath width of 384 feet (117 meters). Multiple passes were made on each target area to ensure the full area was collected. Figure 4.5 shows how the passes were flown. A color version of this figure is located in Appendix B.

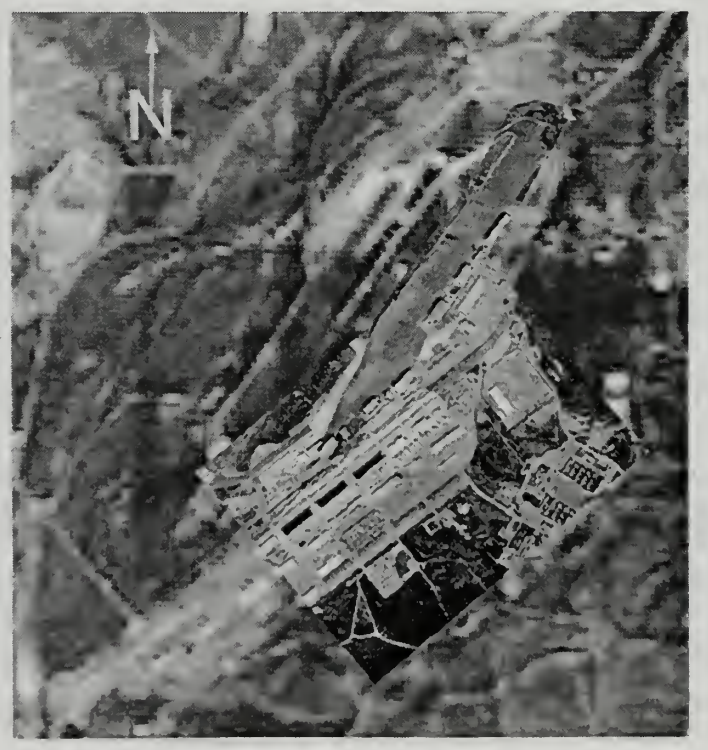

Figure 4.5: A composite image consisting of Landsat TM (bands 1, 2, and 3), a color aerial photograph mosaic, and the two SEBASS images used for this study.

2. Target Description

The airfield at Camp Pendleton MCAS consists of a cement parking apron and an asphalt runway. Most of the aircraft on the parking apron are H-53 helicopters. Since little activity was expected on the runway, it was not imaged for this study. Images of the parking apron were acquired before and after a major flight operation; therefore, it was presupposed that aircraft would not be returned to their exact previous positions.

The supply depot consists mostly of large warehouse-like buildings, parking lots, and staging areas. The building use a variety of roofing materials including tin and tar. The parking lots and staging areas consist of cement and asphalt. Since these images were acquired during a week day, automobiles occupy a large majority of the parking lots. Vandergrift Boulevard separates the supply depot from the airfield and consists of asphalt.

3. Considerations

Winds were high during the collection periods making the aircraft difficult to control. The roll compensator was unable to correct for the high degree of roll error. This is manifested in the data as skewing (or squiggle). Because the squiggle was such a high frequency, it was imperative to remove the squiggle before the data could be registered. The data were "de-squiggled" by cross correlating each scan line with one adjacent to it and determining the line offset from the maximum correlation. A polynomial function was derived from the correlation data and applied to the squiggle pattern. Figure 4.6 illustrates the technique graphically, and Figure 4.7 demonstrates the technique on real data.

Once the error correction was removed, each hypercube was registered to a rectilinear aerial photograph of Camp Pendleton using the triangulation-based registration procedure available in ENVI. In order to compensate for roundoff error in the roll

correction and to minimize the effects caused by along-track stretching and compression due to sampling rate errors, close attention was paid to proper registration. Each image

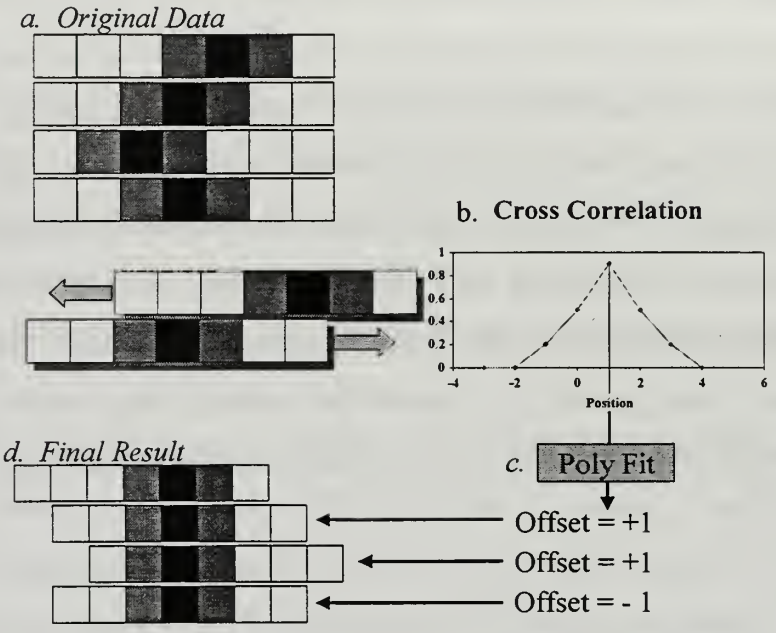

Figure 4.6: The cross-correlation technique for removing error correction. (a) The uncorrected image. (b) The technique by finding the offset with the highest correlation. (c) The corrected (straightened) image.

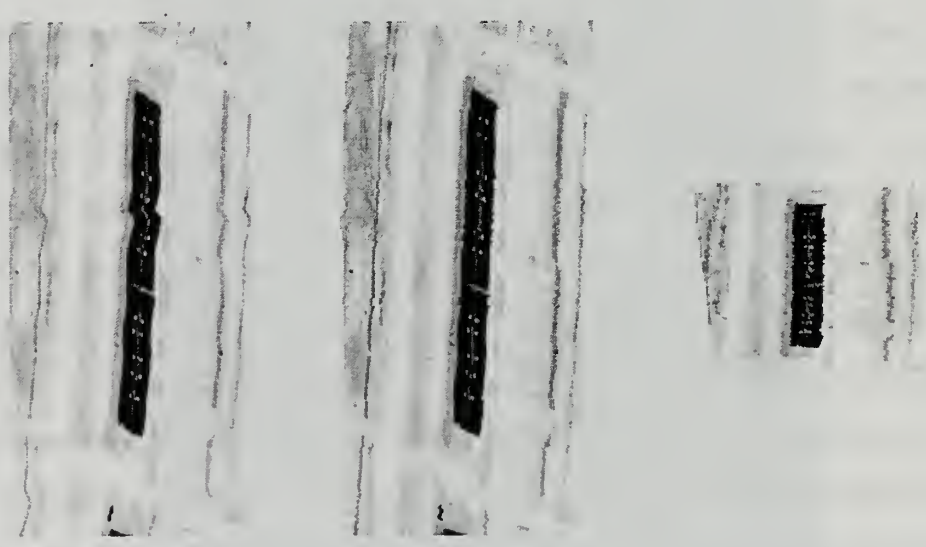

Raw Image Desquiggled Image Registered Image

Figure 4.7: A subset of the Camp Pendleton supply depot where roll correction and registration has been applied.

required at least 50 ground control points to ensure accurate registration. Nearest neighbor interpolation was used to maintain radiometric integrity.

A high degree of roll error was introduced into the airfield scenes. This, coupled with a lack of geographic features that could be used for ground control points, prevented adequate registration. Aircraft parking locations were not sufficiently aligned to enable change detection. Therefore, it was necessary to remove the airfield data from consideration in this study.

The Camp Pendleton data could also be used in the analysis of thermal scarring. Thermal scarring is defined as any change in the appearance of an object which is associated with the proximity of another object. Thermal scarring is usually associated with thermal changes in cement parking areas such as airfields and parking lots. For instance, an aircraft may leave a thermal scar when is has been parked in one place through most of the night. When the aircraft leaves its position, the cement beneath it will be warmer than the surrounding cement leaving a thermal scar that resembles the shape of the aircraft. Thermal scarring is used by imagery analysts to determine the recent departure of vehicles from a given position.

It is not always clear, however, that thermal scarring is caused by temperature differences. Vehicles tend to leak hydraulic fluid which can change the emissivity of the surface below. This can also appear brighter or darker than the surrounding area. This type of scarring is created over time, but it can be interpreted incorrectly as a thermal scar associated with aircraft or vehicle operations. For this reason, it is important to differentiate a true thermal scar (indicating vehicle movement) from other types of scarring. The airfield data provides a number of thermal scarring examples; however, since the data are not conducive to change detection, further study is recommended at a later time.

C. CONSIDERATIONS FOR SPECTRAL CHANGE DETECTION

The quality of spectral data can vary widely, and it is important to avoid restriction of this study to only one data set. As mentioned previously, a number of undesirable characteristics accompany the analysis of aerial data. These characteristics can preclude accurate analysis; however, they highlight the problems associated with aerial data and warrant study concurrent with a study under more controlled conditions.

Although the CARD SHARP data do not contain artifacts associated with attitude errors, they do contain instrument-related errors which require a closer look. These data allow the scope of the analysis to narrow to the evaluation of techniques without considering how certain artifacts might affect those techniques. It also allows the analysis to consider other problems with change detection that might be associated with thermal spectral imagery in general that otherwise might be masked by platform-specific issues.

One example is the noticeable variability in the data between dates. It is expected that changes in air temperature, humidity, and other weather conditions will affect overall scene brightness as well as affect some local areas in different ways; however, local variations in these data appear to be unnatural. Figure 4.8 shows band 64 on 10 October. A brightness gradient is present such that the left side of the image is brighter than the right side. PC band 5 of the 10 October data isolates some of the gradient.

10 October 96, Band 64

10 October 96, PC Band 5

Figure 4.8: These images show that an along-track gradient exists where the left side of the image is brighter than the right side.

Gain inconsistencies are also present in the across-track direction. Figure 4.9 shows the first 200 lines of three principal components (PC bands 1, 7, and 15) for both dates and the result of differencing those PC bands (11 October minus 10 October). For both dates, band 1 contains overall brightness information and is provided for orientation. PC bands 7 and 15 contain distinct periodic noise that cannot be attributed to natural causes. It would appear that the gain fluctuates along the spatial dimension of the LWIR FPA. The differenced images demonstrate that this fluctuation is not consistent between dates because the periodic pattern is not minimized or eliminated. These gain inconsistencies add to the noise making it difficult to identify small spectral changes.

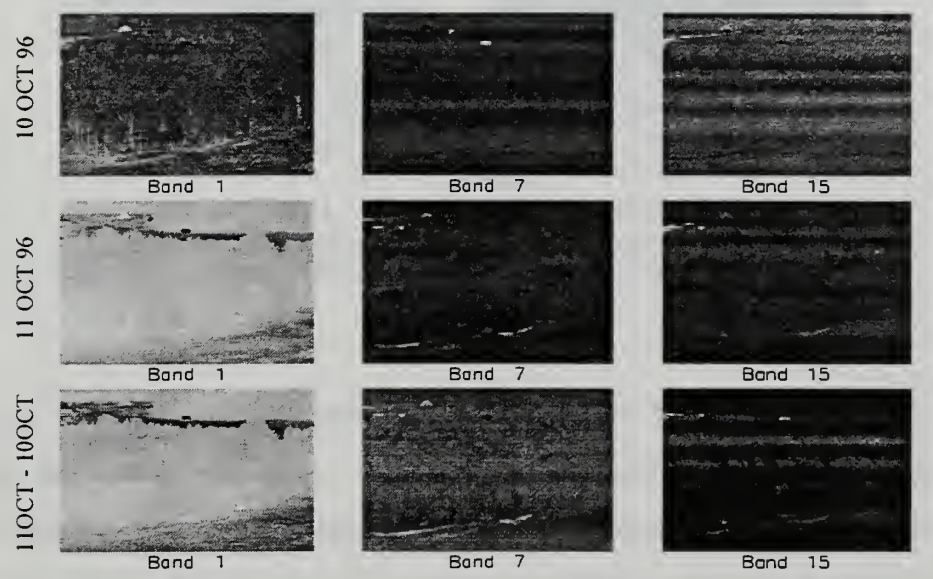

Figure 4.9: A comparison of PC bands 1, 7, and 15 for both dates and the difference between the two dates.

Since much of the signal in thermal spectral data is caused by thermal emission, converting the data to emissivity removes much of the information content and has the effect of exaggerating the noise. To demonstrate this the data were converted to emissivity using the plastic ruler method and atmospheric data from MODTRAN. Figure 4.10 depicts this result. When the data are converted to emissivity, a brightness gradient is easily observed in scenario 1 that is not introduced from the natural local environment.

Scenario 2 contains no gradient. In both images, the across-track periodic pattern is present. This phenomenon appears to be specific to SEBASS, but may not be a recurring artifact in the instrument. Its impact on the ability to conduct change detection is profound. Such brightness gradients can hide subtle changes within noise and increases the potential for false alarms. For this reason, using data converted to apparent emissivity proved unreliable. Since the noise was not as evident in the unconverted data, the at-sensor radiance data was used in this study. This example suggests that tighter sensor gain control is required to improve change detection capability.

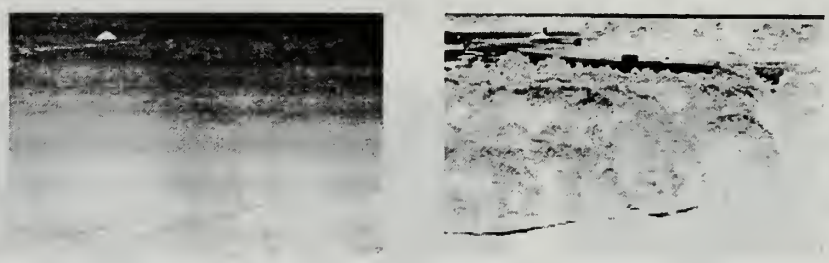

10 OCTOBER 98 11 OCTOBER 98

Figure 4.10: A comparison of CARD SHARP images converted to emissivity.

To further investigate the difference in emissivity data, Figure 4.11 plots the histograms from emissivity band 64 of both dates. It is easy to see that the drastic difference in the two histograms would make it impossible to use for change detection. Based on Figure 4.10 above, it appears that the 11 October data more closely resembles apparent emissivity data. Another conclusion can then be drawn from its histogram. The majority of the material in the image has an emissivity greater than 0.995 which suggest that most objects in the image are nearly blackbody emitters. Therefore, spectral change in heavy vegetation will occur within 0.5 percent of the total signal. This further suggests that a very high SNR is required to accurately conduct change detection.

These problems appear to be unique to the CARD SHARP collect and are not evident in other data as SEBASS development continues. Further improvements to the

thermal spectral program will increase the sensitivity and utility of such an instrument for change detection.

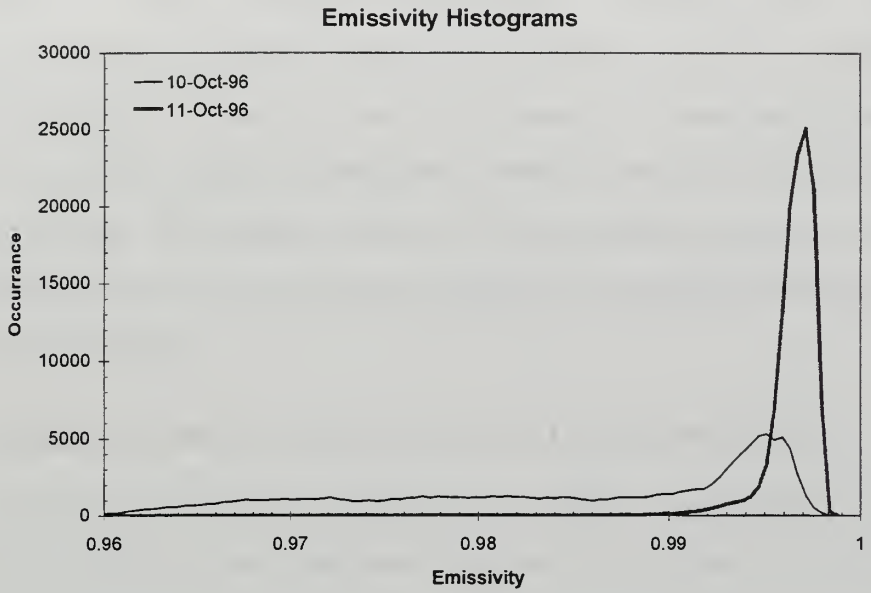

Figure 4.11: Histograms of band 64 from both dates converted to emissivity

V. DATA ANALYSIS

Before the value of various change detection techniques can be studied it is necessary to characterize spectral change and consider the value of spectral change detection in general. The analysis here does not attempt to categorize current methods, but rather performs an in-depth examination of spectral change in these data using simple analysis techniques. The desired result is to detect spectral change, to evaluate these analysis methods, and to classify sources of error that reduce the effectiveness of spectral thermal change detection.

A. METHODS FOR HYPERSPECTRAL CHANGE DETECTION

Not all of the methods illustrated in Chapter 2 are useful for this work. Classification techniques were eliminated from this study because of their complexity. Generally, post classification comparison and direct multidate classification work well when a scene provides a relatively small number of large areas such as vegetation, water, and urban. When trying to identify a very small number of pixels that represent a change class, the task becomes difficult. It is further complicated when the changes of interest are a subset of a larger class such as vegetation as is the case with the CARD SHARP data. To attempt a proper study of classification techniques would require many iterations and extensive analyst intervention. This defeats the purpose of seeking techniques that would reduce such intervention and the amount of time required to analyze a scene. It is possible that further study will reveal that classification techniques are useful and accurate, but they have been considered outside the scope of this introductory study of change analysis for thermal hyperspectral imagery.

The emphasis of this study is on simple techniques and determining the feasibility of detecting spectral change. With that in mind, the analysis of the CARD SHARP data is strictly an analysis of spectral change in thermal imagery in the context of a heavily vegetated environment. Change vector techniques such as differencing and spectral angle

will be the primary means for identifying change. A similar analysis is provided for the Camp Pendleton data; however, a different set of challenges exists with these data thus further testing the techniques in a more realistic environment.

B. CHANGE DETECTION: CARD SHARP

1. Image Differencing and the Target-to-Background Separation (TBS)

A goal of this work is to utilize the spectral character of the data to detect changes that are often not detected in broadband imagery. The intent is to find subtle changes in a scene that equate to spectral features where, in broadband imagery, these features are averaged and removed.

To begin, we must first look at change detection in simulated broadband imagery. Two CARD SHARP hypercubes were converted to pseudo forward looking infrared (FLIR) images by averaging all bands equally. The result is a single broadband image for each date. The images were differenced to determine if the change in the vehicles could be discerned without the spectral information. Figure 5.1 is the resulting change image scaled to enhance the identification of the changed targets. The 1000 line image has been divided into two segments beginning at the top left and ending at the bottom right. The image is expressed in difference in radiance measured in μflicks. The image gray scale is set such that white represents a small change and black represents a large change. Note that most of the vehicles are discernable without the need for the spectral dimension. This suggests that the largest amount of change associated with the targets is caused by the thermal difference of using camouflage and not using camouflage.

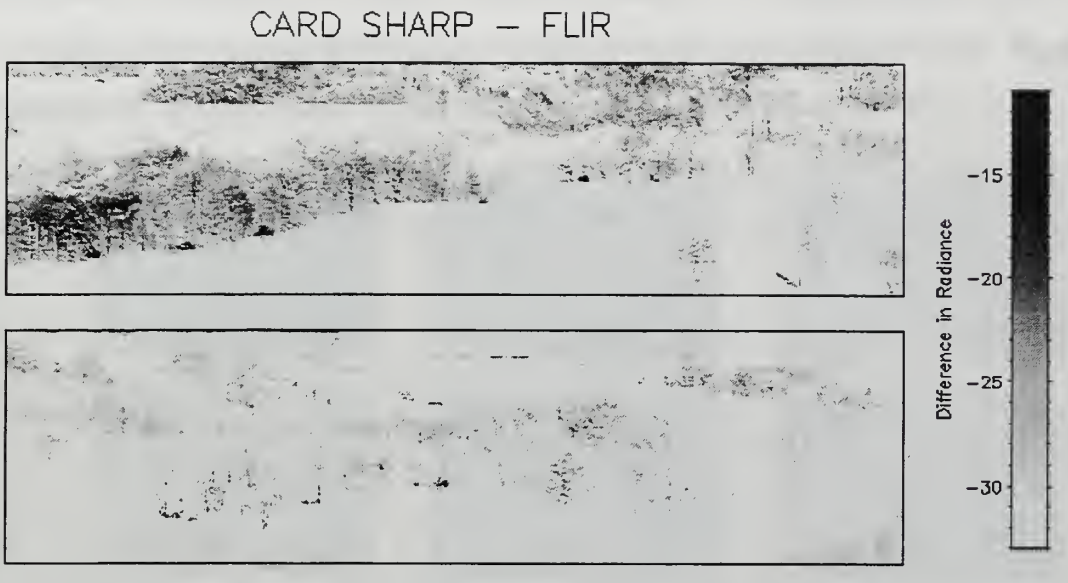

Figure 5.1: A change image created by first averaging all bands of each hypercube and then differencing the two resulting images.

To further illustrate the concept of change, it is appropriate to discuss the difference distribution as done in Chapter 2. Recall that areas of no change will remain close to the mean of the distribution while areas of change will appear in the tails. Figure 5.2 is a comparison of the histogram of the entire change image and the histogram of the pixels that contain target information (indicated in black). The vertical and horizontal lines represent the mean (-39.32) and standard deviation (13.96) respectively of the entire scene. The subset of target pixels will include a small number of background pixels adjacent to the targets and small number of mixed target/background pixels. The mean of the target pixels is 1.96 standard deviations to the right of the mean of the entire change image. This measure will be referred to as the target-to-background separation (TBS). Also note that a large portion of the target pixels fall completely outside the distribution of the non-target pixels. These pixels are highly discernable and do not resemble background. Target pixels that fall inside the overall distribution compete with background and may be less discernable.

The image in Figure 5.1 is scaled over the distribution of target pixels such that any target pixels outside the overall distribution appear black and all other pixels with values from –10.0 to –35.0 are scaled from black to white. This illustrates the mixing in the distribution of background and target pixels. All pixels that appear as non-white are in the same distribution as the leftmost target pixels depicted in the histogram.

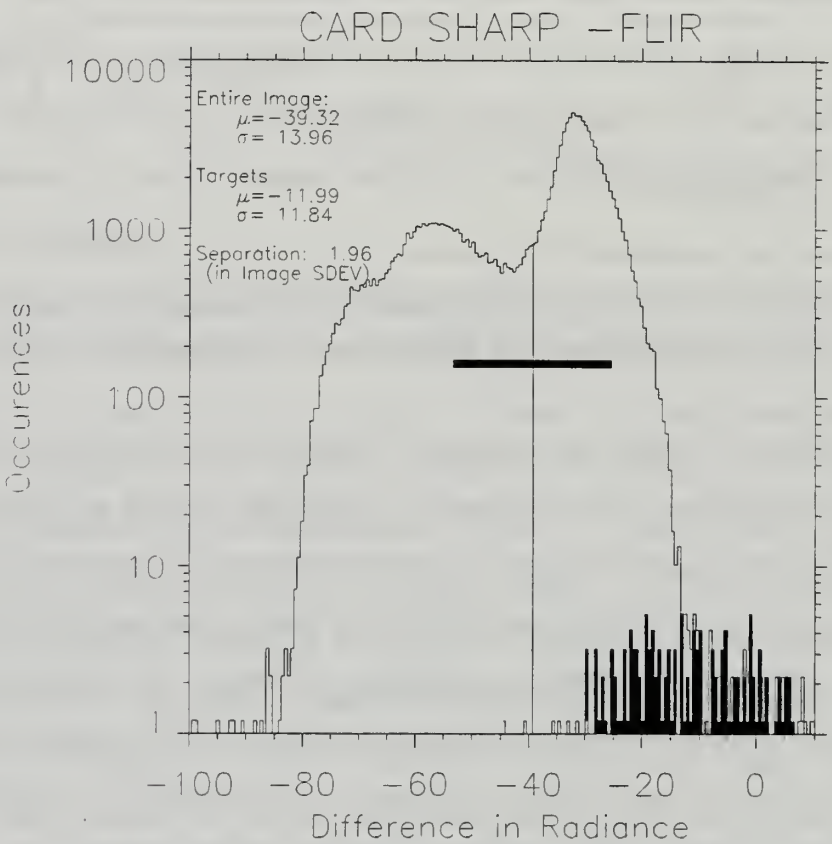

Figure 5.2: A histogram of the CARD SHARP change image in Figure 5.1 produced from the pseudo FLIR images.

Such a result in a broadband image seems to negate the need for spectral change detection. In fact, the CARD SHARP data set appears to be void of significant spectral change that is independent of thermal change. Figure 5.3 illustrates 18 bands of the first 200 lines of the change vector image. Note that the three vehicles in the image are visible in every band which indicates that removing the camouflage corresponded to an overall

increase in target radiance. This suggests that it might be an inappropriate data set for an in-depth study of spectral change techniques. This unexpected result for the heavily vegetated Huntsville scene requires a more careful consideration.

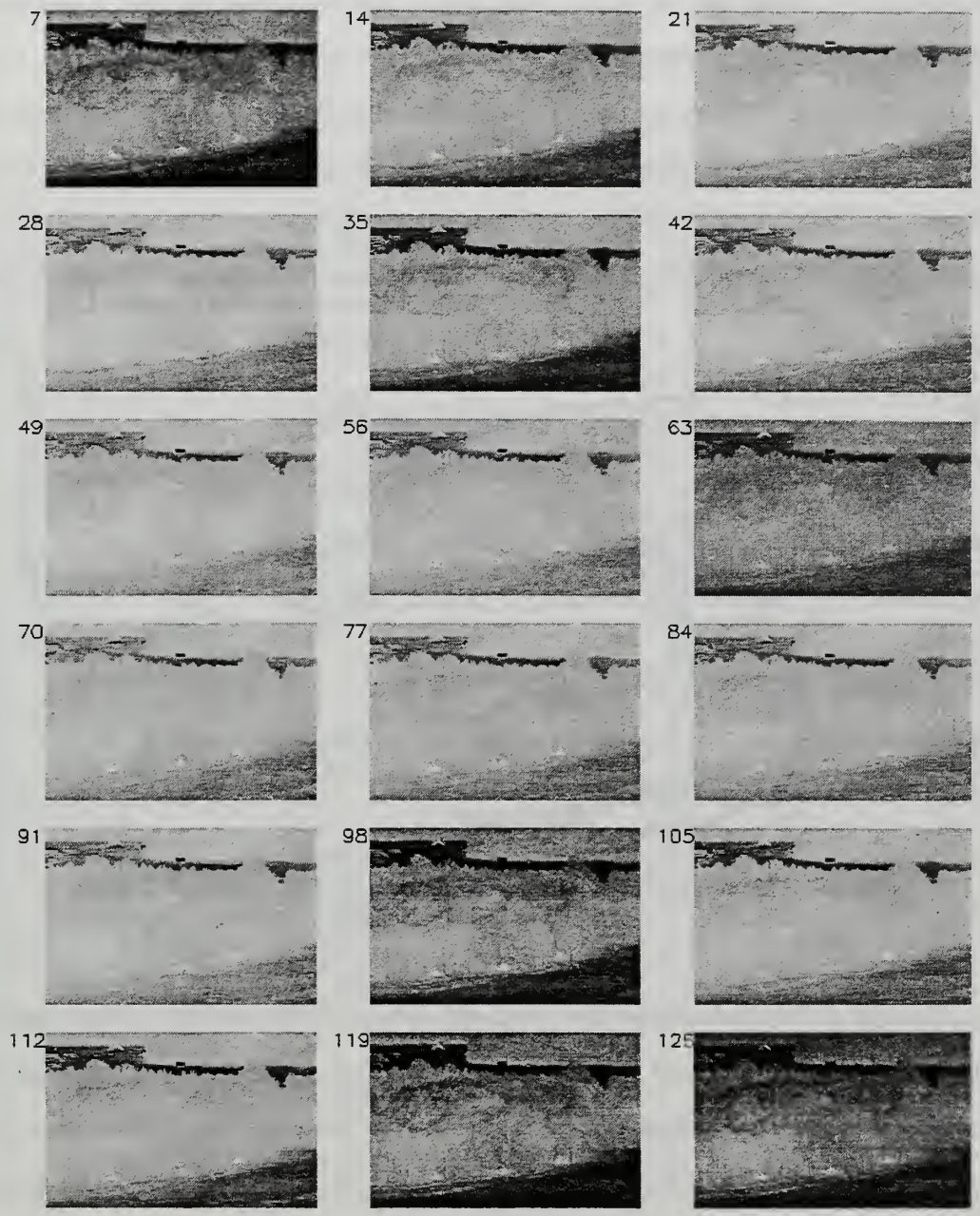

Figure 5.3: The first 200 lines of the CARD SHARP change vector - eighteen bands spaced seven bands apart.

Figure 5.4 is a plot of the ground truth spectra of the M-60 tank with and without camouflage. A color version of this figure is available in Appendix B. This plot also includes the difference of the two spectra. A significant spectral feature is visible at 9.50 μm where there is a relative decrease in radiance of the camouflaged tank. This equates to band 31 in the SEBASS dates.

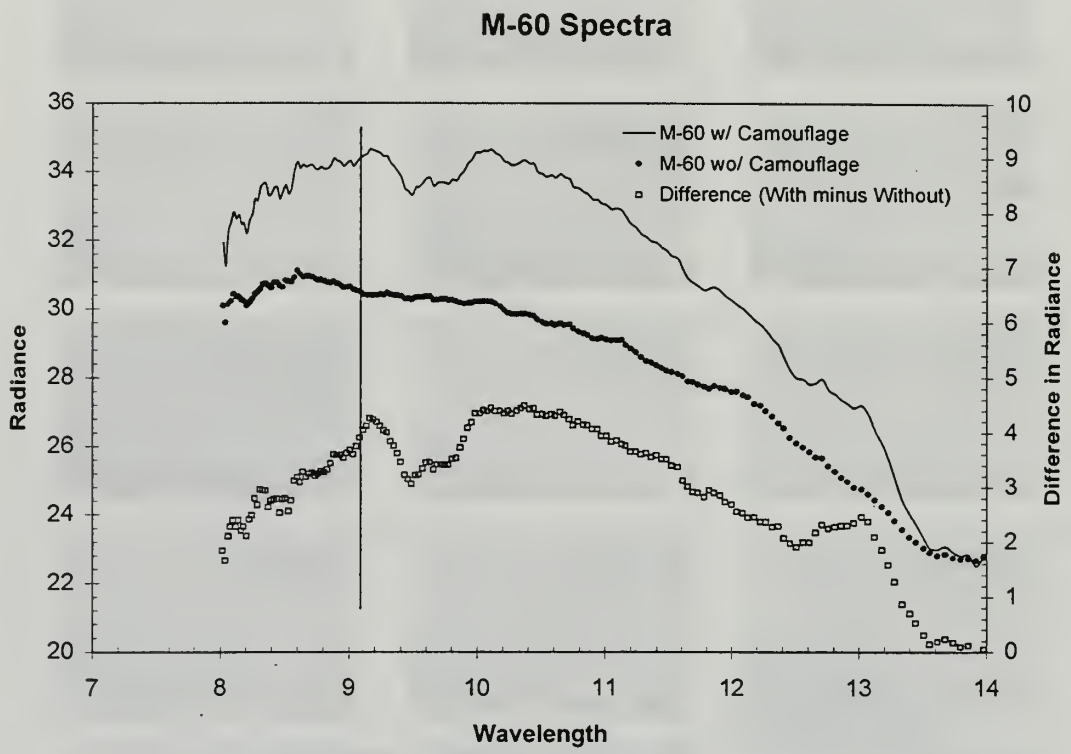

Figure 5.4: Ground truth spectra acquired during CARD SHARP for the M-60A MBT.

Ground truth spectra were not available for all of the vehicles in the scene, so a variety of pixels were sampled from the image and their spectra are presented in Figure 5.5. There are two major features that stand out in these spectra. There is a feature located at 9.16 μm (band 27) and one located at 12.52 μm (band 98). The feature at 12.52 μm is an atmospheric absorption band and is not actually a true target spectral feature. Figure 5.6 depicts the MODTRAN output for Huntsville, Alabama during

October. An absorption band is present at 12.52 μm, and the change here is associated with the fluctuation of the humid Huntsville atmosphere.

The feature at 9.16 μm appears to be the compliment to the feature previously identified in the camouflaged M-60 spectrum. Close comparison of Figure 5.4 with Figure 5.5 shows that both the 9.45 μm and 9.16 μm features are present in the ground truth and SEBASS data. A more revealing plot of this relationship is presented in Figure 5.7. This feature is present in the image in all three camouflaged U.S. vehicles but not present in the foreign vehicles or vegetation. This appears to be the only truly discernable spectral feature available in the CARD SHARP scene. Color versions of Figure 5.5 and Figure 5.7 are available in Appendix B.

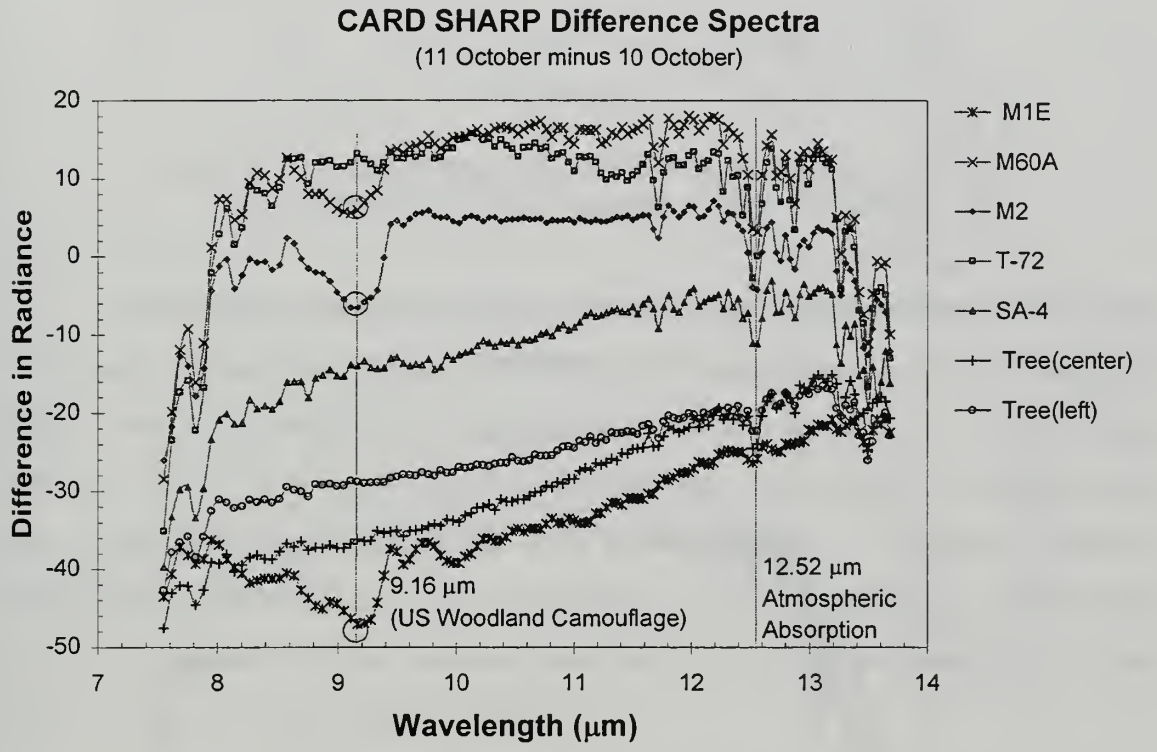

Figure 5.5: A variety of difference spectra produced by subtracting the spectrum at a given pixel location in the 10 October image from the spectrum at the same pixel location in the 11 October image.

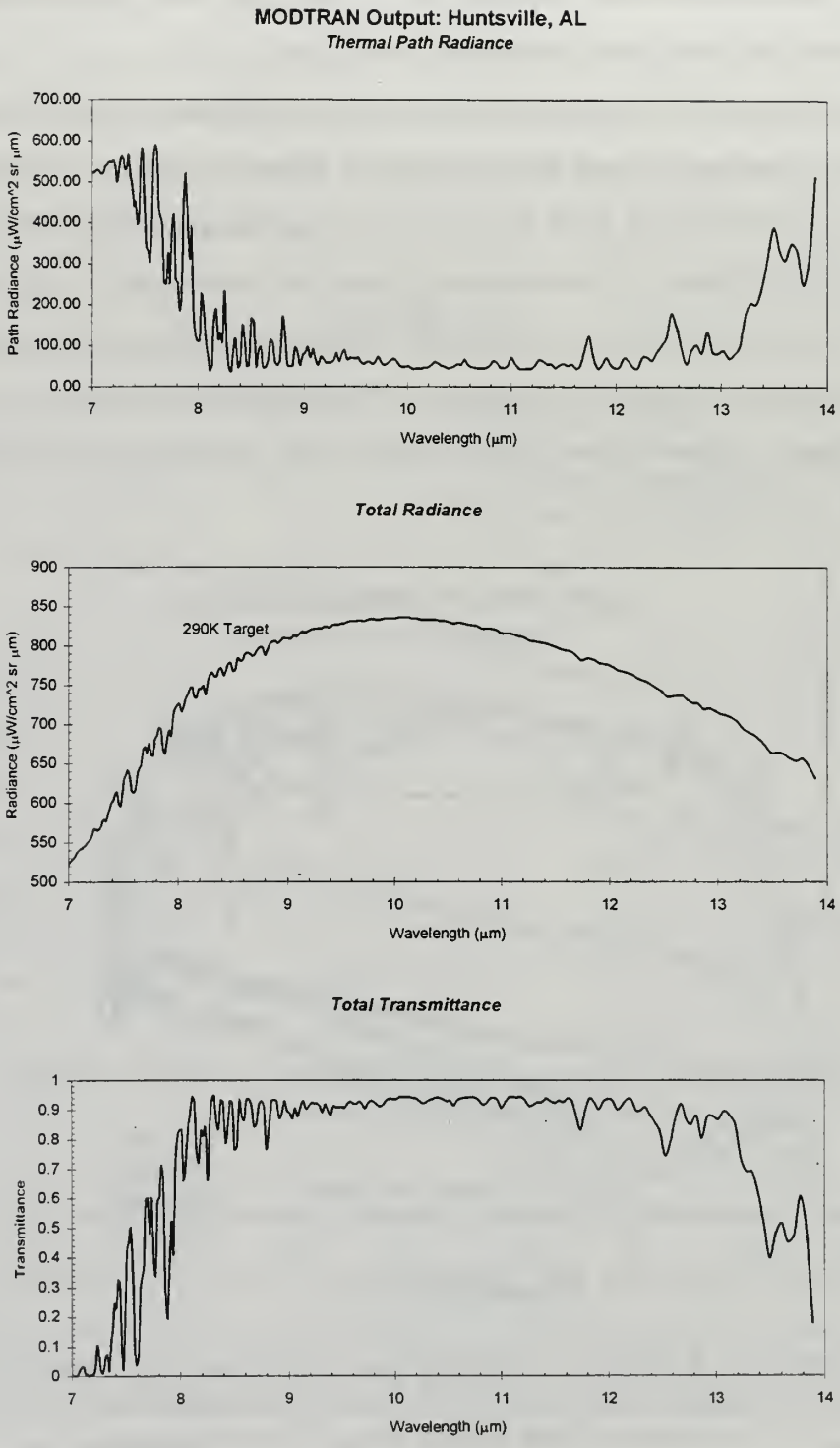

Figure 5.6: MODTRAN output for Huntville, Alabama during October.

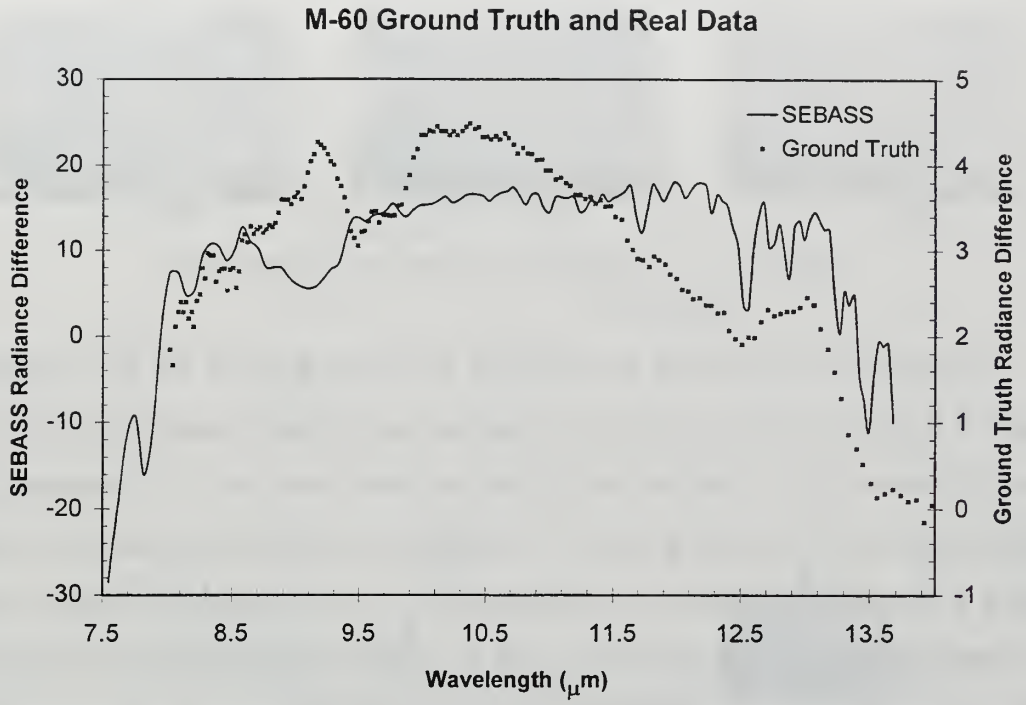

Figure 5.7: A comparison of SEBASS and ground truth *difference* data for the M-60A MBT with and without camouflage.

These differenced spectra suggest the data should be compared at these spectral wavelengths. The uncamouflaged vehicles in the image from 11 October should be brighter than the camouflaged vehicles in the 10 October image. In a change image, where 10 October is subtracted from 11 October, this would appear as a brighter value than pixels that do not exhibit the same spectral change. While this feature is distinguishable in the spectra, it does not produce a noticeable difference in the images. Figure 5.8 compares 200 lines containing the three U.S. vehicles for Band 27 (9.16 μm), band 33 (9.50 μm), and band 98 (12.52 μm).

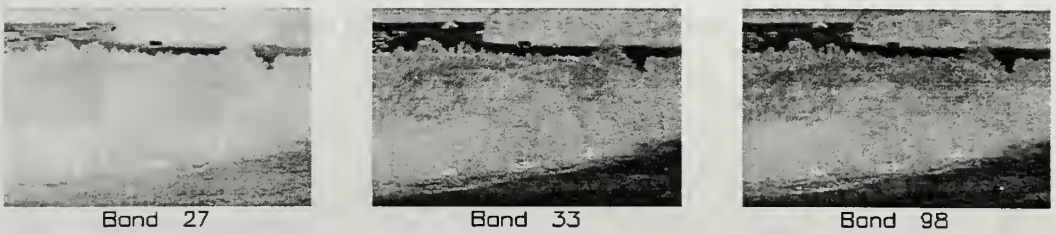

Figure 5.8: A comparison of three significant bands.

This qualitative result can be quantified by further study of the data distribution. Figure 5.9 through Figure 5.16 are the histograms and change images for bands 27, 33, 86, and 98 respectively. The most significant indication that there is a difference in the vehicles from the two bands is that, in band 33, the target-to-background separation (TBS) is 1.99 standard deviations, and in band 86, it is 1.90 standard deviations. This is not an appreciable difference considering that the TBS for the simulated FLIR image was 1.97, but it does demonstrated that relatively small spectral changes are detectable using TBS. Note that band 98 has a TBS of 2.17. This is the highest of all four selected bands but is associated with an atmospheric absorption feature instead of a spectral feature. The vehicles are plainly visible in all images which further illustrates the dominance of the thermal change over the small spectral change.

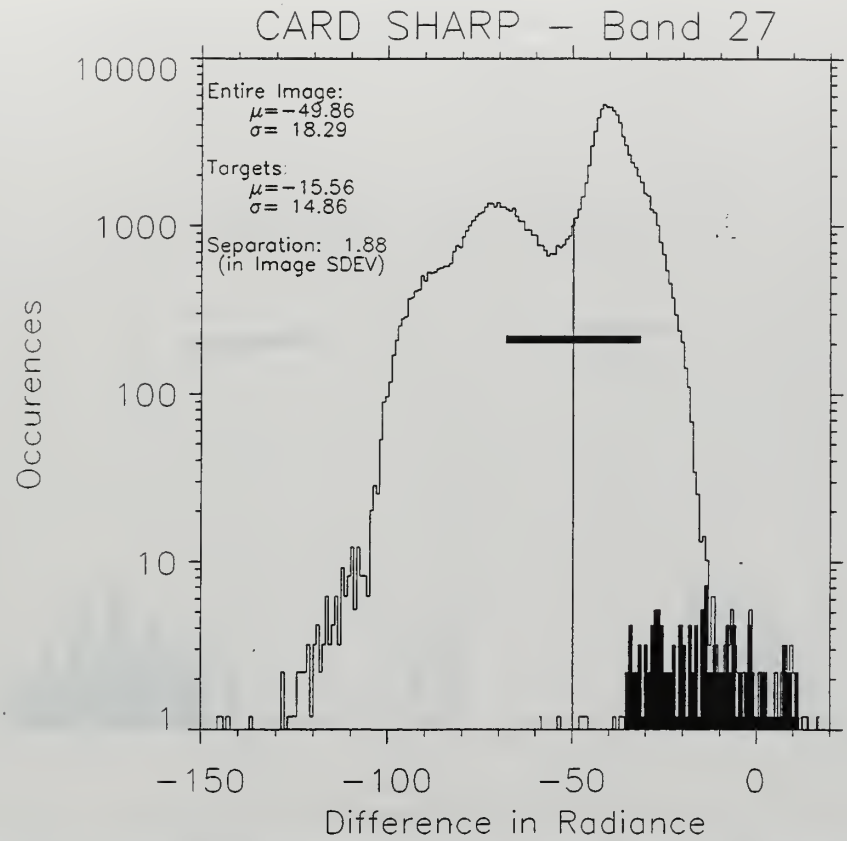

Figure 5.9: Histogram for CARD SHARP difference band 27 (9.16 μm).

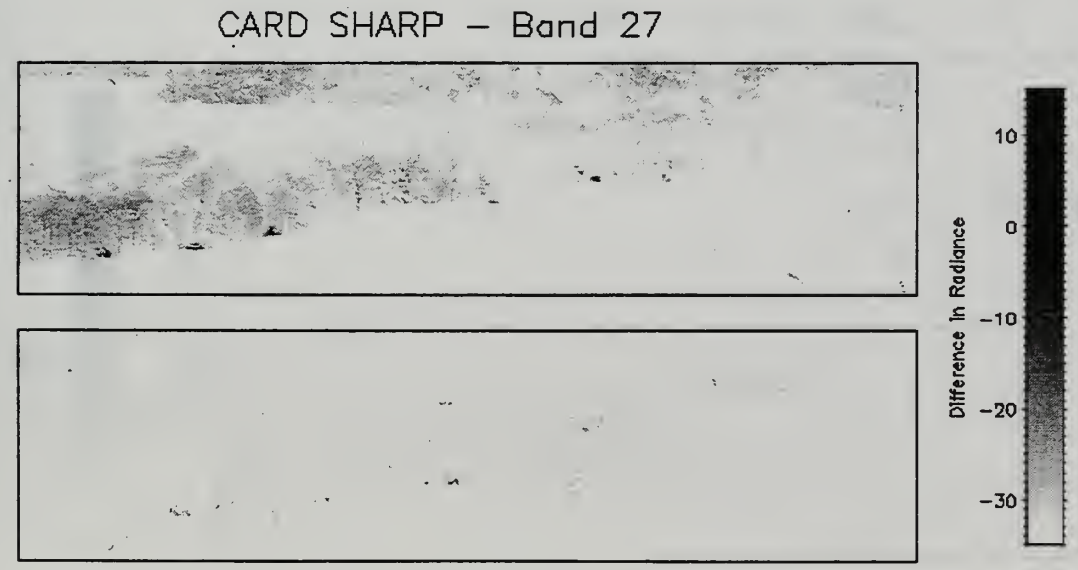

Figure 5.10: Change image for CARD SHARP difference band 27 (9.16 μm).

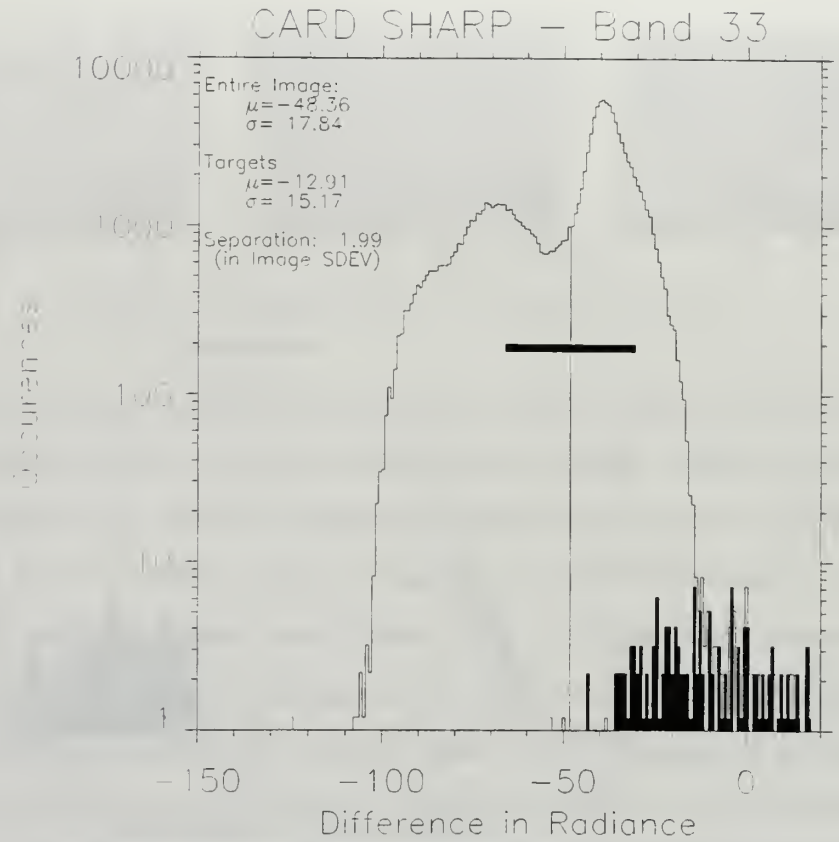

Figure 5.11: Histogram for CARD SHARP difference band 33 (9.50 μm).

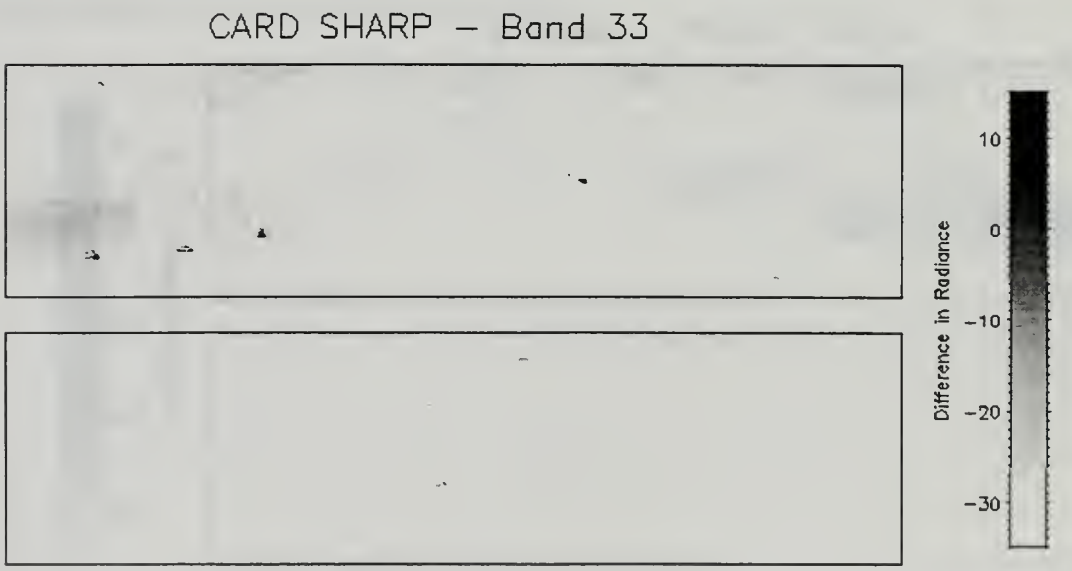

Figure 5.12: Change image for CARD SHARP difference band 33 (9.50 μm).

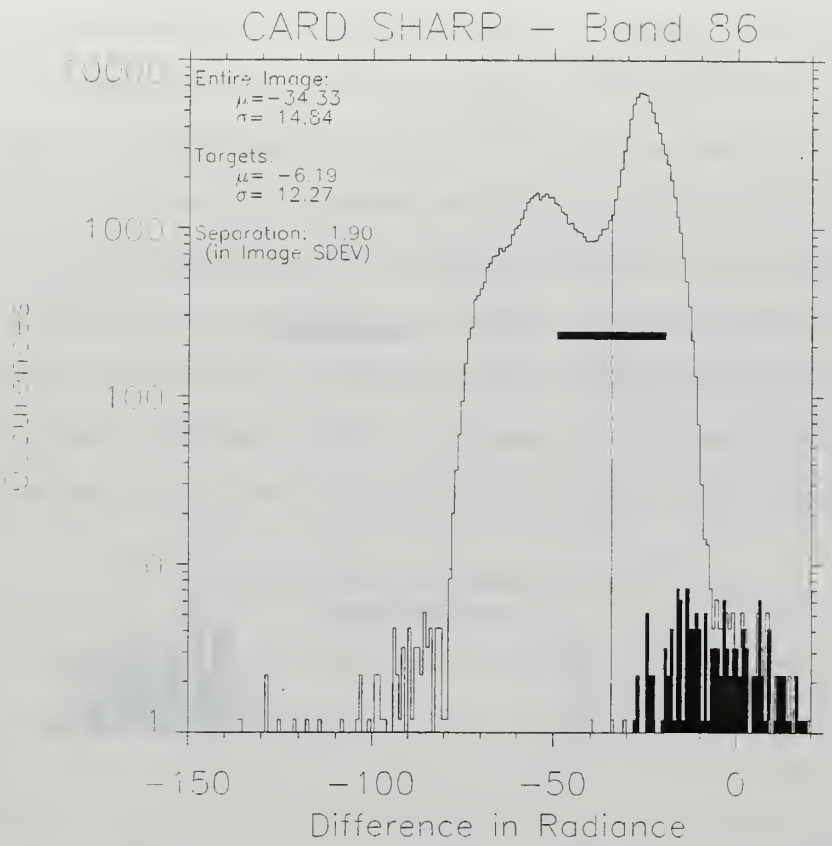

Figure 5.13: Histogram for CARD SHARP difference band 86 (12.02μm).

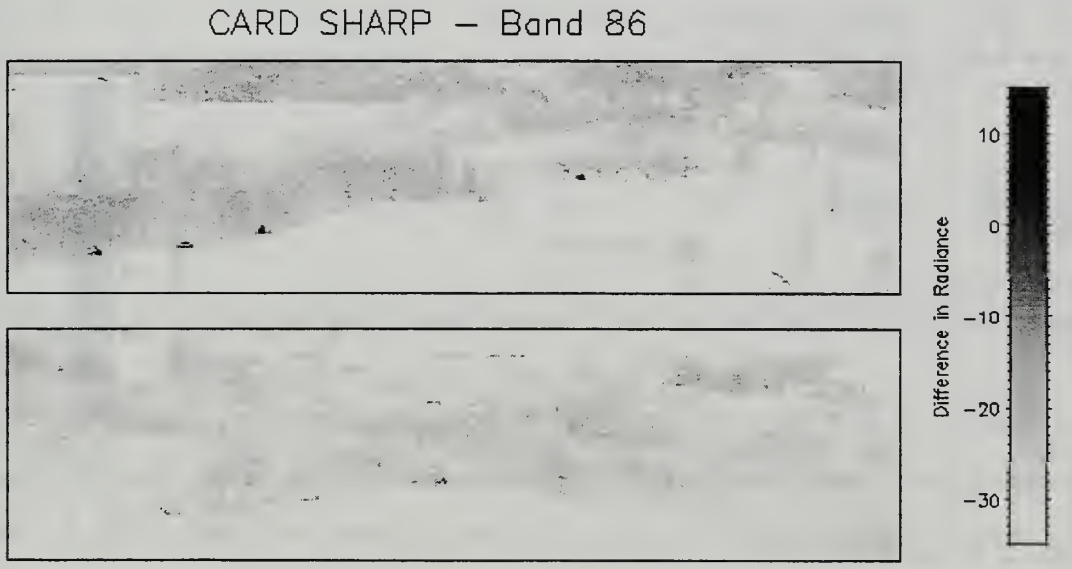

Figure 5.14: Change image for CARD SHARP difference band 86 (12.02 μm).

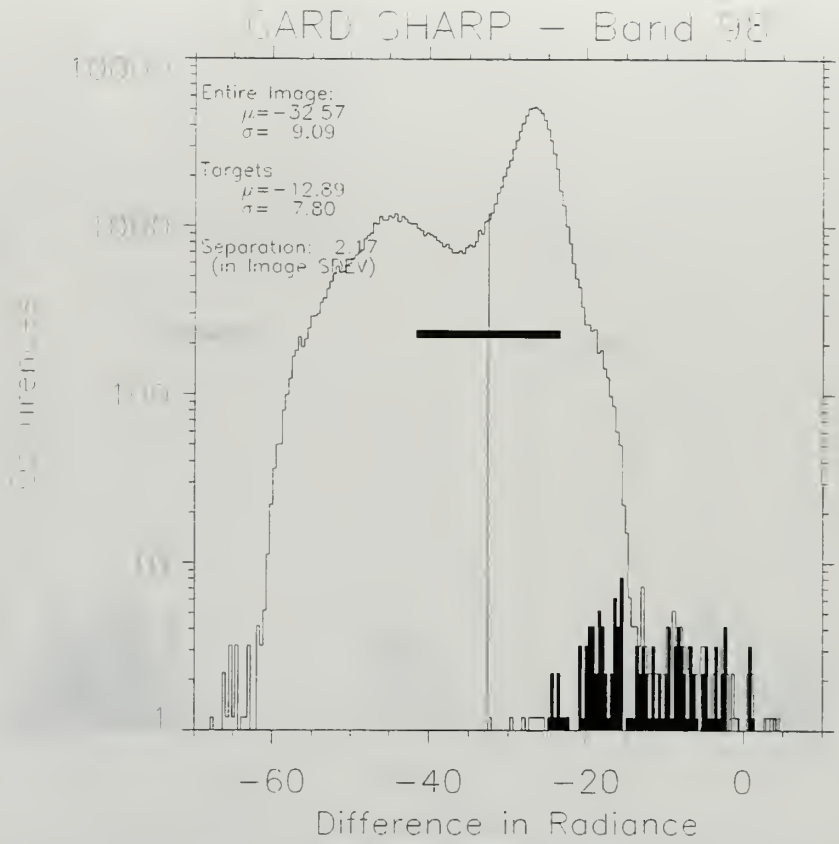

Figure 5.15: Histogram for CARD SHARP difference band 98 (12.52 μm).

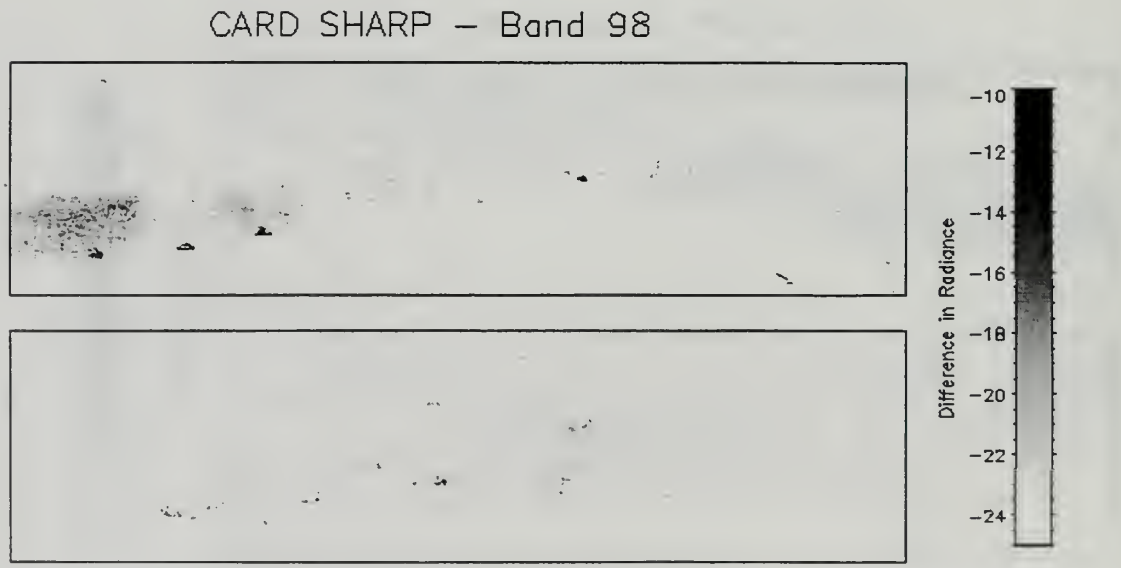

Figure 5.16: Change image for CARD SHARP difference band 98 (12.52 μm).

The TBS proves to be an adequate measure of spectral change. To better understand the relationship of all bands in the change image, Figure 5.17 plots TBS against wavelength. A useful band with a highly discernable spectral feature would have a TBS much higher than the random fluctuations in the other bands. Note that 9.16 and 9.50 μm maintain their distinct feature but do not appreciably improve change detection. Band 98 (12.52 μm), the atmospheric absorption band, has a much greater TBS than the majority of the data. This may be caused by contrast-enhancing effects created by the water absorption and the moisture present in vegetation but absent in the camouflage. Other absorption bands, at 9.77 and 13.50 μm appear to produce a similar effect.

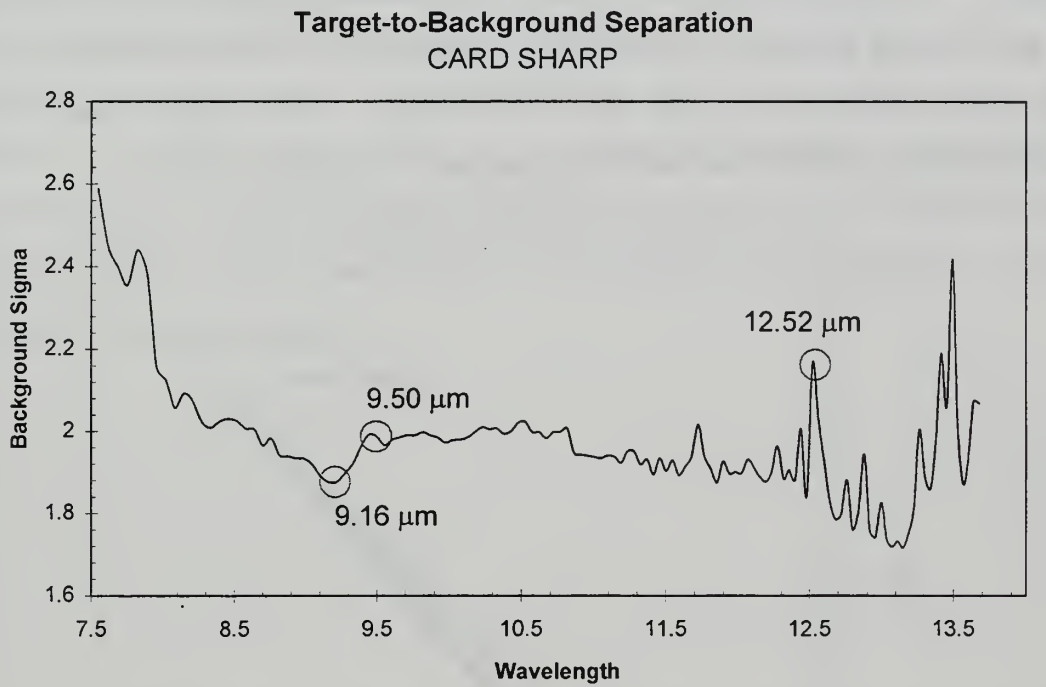

Figure 5.17: Target-to-background separation for the CARD SHARP change image.

This plot indicates that there is no sufficient proof that spectral change information is present and detectable in the CARD SHARP data. Simple techniques, such as differencing, are useful in identifying thermal change in these data but provide little utility in detecting spectral change. It is possible, however, that the most useful

bands in detecting CC&D changes in a heavily vegetated environment are the atmospheric absorption bands.

Further indication of the absence of spectral information in the CARD SHARP data can be found by plotting the histograms simultaneously on a scatter plot. Figure 5.18 depicts such a plot for bands 27 and 33 (chosen to include the 9.16 and 9.50 μm feature). A color version of this figure is available in Appendix B. The strong linear relationship of the data represent the radiometric similarity of the two bands. In other words, bright pixels in band 27 are also bright in band 33. Points plotted off axis from this linear relationship behave differently in the two bands and may represent a spectral change. The highlighted points in Figure 5.18 represent the target pixels. A color version of this figure is available in Appendix B. Although, the points are clustered together, they do not depart from the linear relationship. This indicates that they are radiometrically different from the background but not spectrally different.

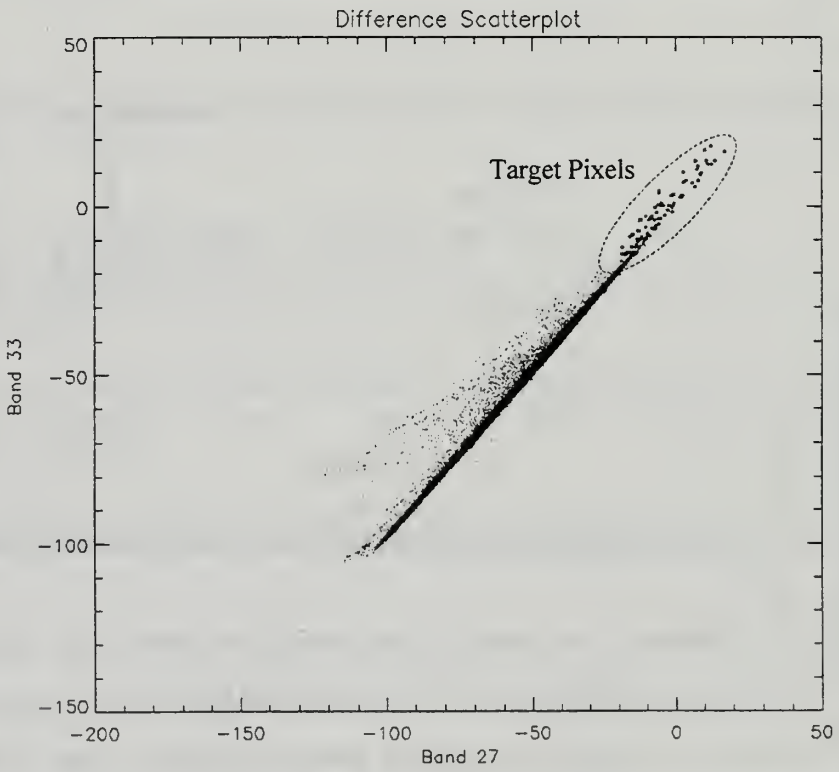

Figure 5.18: A scatter plot for CARD SHARP difference band 27 (9.16 μm) and band 33 (9.50 μm).

2. Spectral Angle

The spectral angle of the change vector was also studied. The spectral angle result was created from the dot product of the two images as described in Chapter 2. Figure 5.19 presents the histogram of this change result. This figure plainly demonstrates the spectral blandness of the data. The target pixels fall in the heaviest part of the distribution. The TBS of 0.27 means very little because areas of change will have a higher spectral angle regardless of their position with respect to the background mean. Two major change distributions are present in this result. The forest makes up the distribution to the left of the mean while the grass makes up the distribution to the right. Therefore the grass appears to have changed the most. This is likely caused by a difference in moisture on the two days. (It had rained in the interval.) The majority of the target pixels fall within the change distribution for the forest which would make them difficult to discern. Without examining the change image, one can see that it would be difficult to discern these targets.

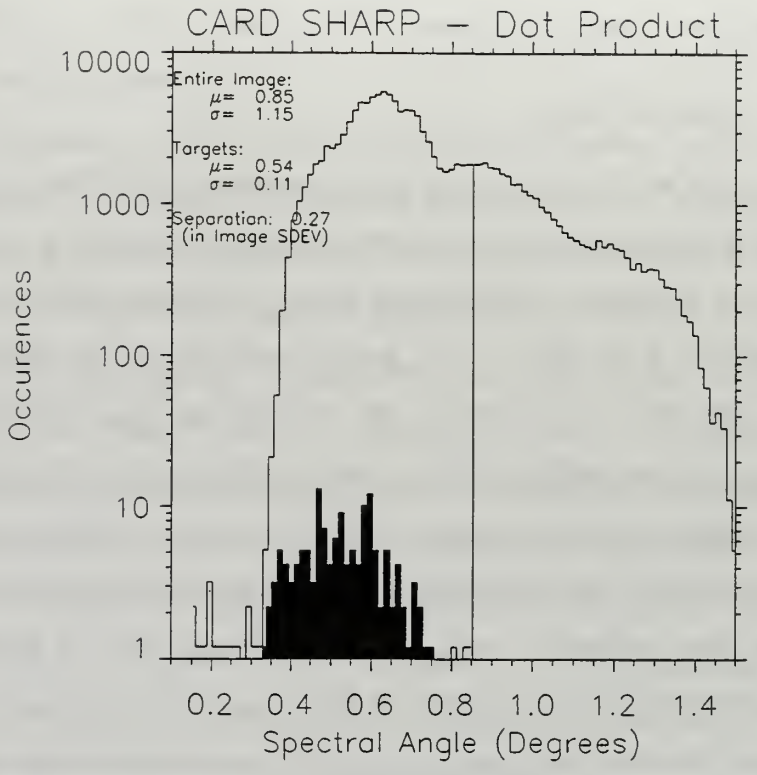

Figure 5.19: Histogram for the CARD SHARP spectral angle result.

Figure 5.20 is the change image for the dot product. The image has been converted to spectral angle in degrees and displayed such that the darkest pixels have the highest spectral angle. The three U.S. vehicles and the T-72 are barely visible in the image. They are visible only because they are darker than their local background. This suggests that there is some difference between the vehicles and the surrounding vegetation; however the change is minimal and many of the target pixels have spectral angles between 0.35 and 0.50 which causes them to blend with the surrounding vegetation. For this result, spectral angle appears to provide marginal utility to the change analysis. This is likely due to the lack of spectral change. Since the only discernable spectral feature was available in the U.S. camouflage, it would make sense that the only changes truly discernable in this result come from the U.S. vehicles.

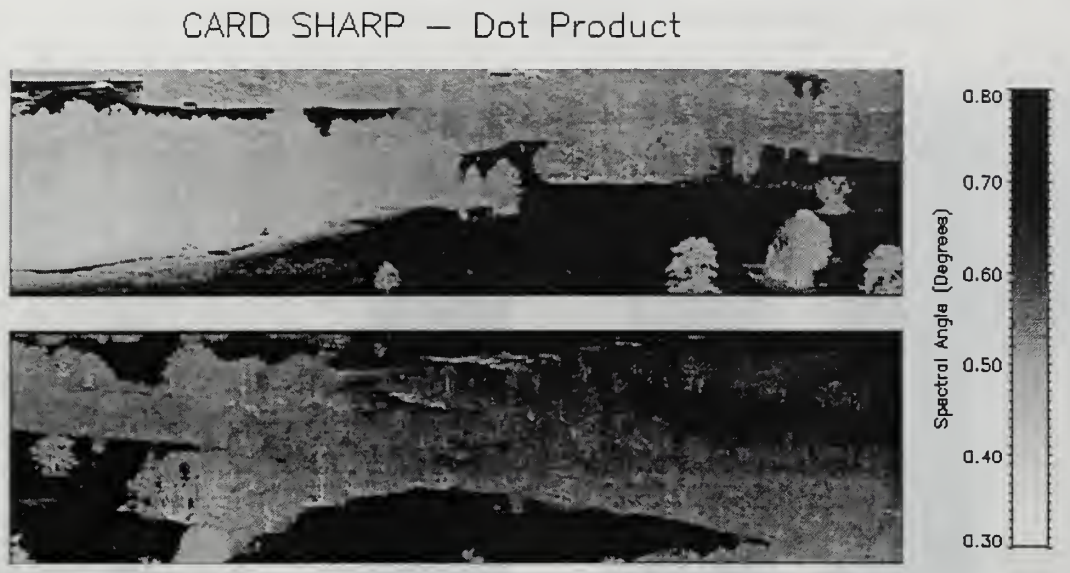

Figure 5.20: Change image for the CARD SHARP spectral angle result.

C. CHANGE DETECTION: CAMP PENDLETON

1. Image Differencing

Similar change vector techniques were applied to the Camp Pendleton data. Change images were obtained by subtracting Run 1 (obtained at 1000 on 10 December) from Run 2 (obtained at 1400 on the same date). Figure 5.21 depicts the result for band 51 (10.28 μm). A color version of this figure can be found in Appendix B. The difference image is busy and difficult to interpret. Numerous misregistration errors make it difficult to identify genuine changes. By comparing all three images side-by-side, two changes appear to stand out. One appears to be the existence of a cool object in run 1 that is not present in run 2 located to the right of the third warehouse (Change A). The second is the existence of a warm object in run 2 that is not present in run 1 located to the right of the second warehouse (Change B). Both changes appear as positive (bright) pixels in the change image; however, they are still difficult to distinguish from the busy background.

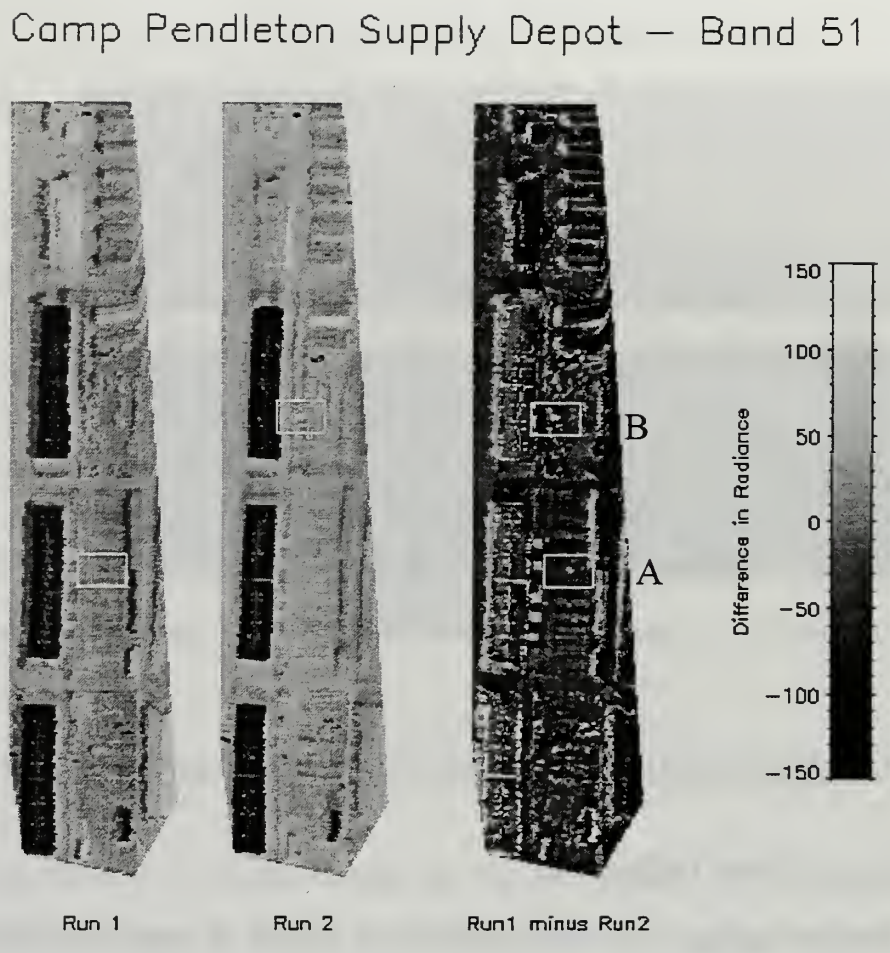

Figure 5.21: Image differencing result for band 51 (10.28 μm) of the Camp Pendleton data. Two genuine changes are indicated at A and B.

Figure 5.22 examines the spectra of three pixels across change A in the vertical direction. A color version of this figure is available in Appendix B. While the change is discernable in the image, it appears to be caused by an increase in temperature at that location. Note that the temperature of the second pixel is higher for run 2, but the temperature of the two adjacent pixels is lower for run 2. The spectra at all three pixels is similar for run 1 and run 2 which suggests that new material has not been introduced at this location.

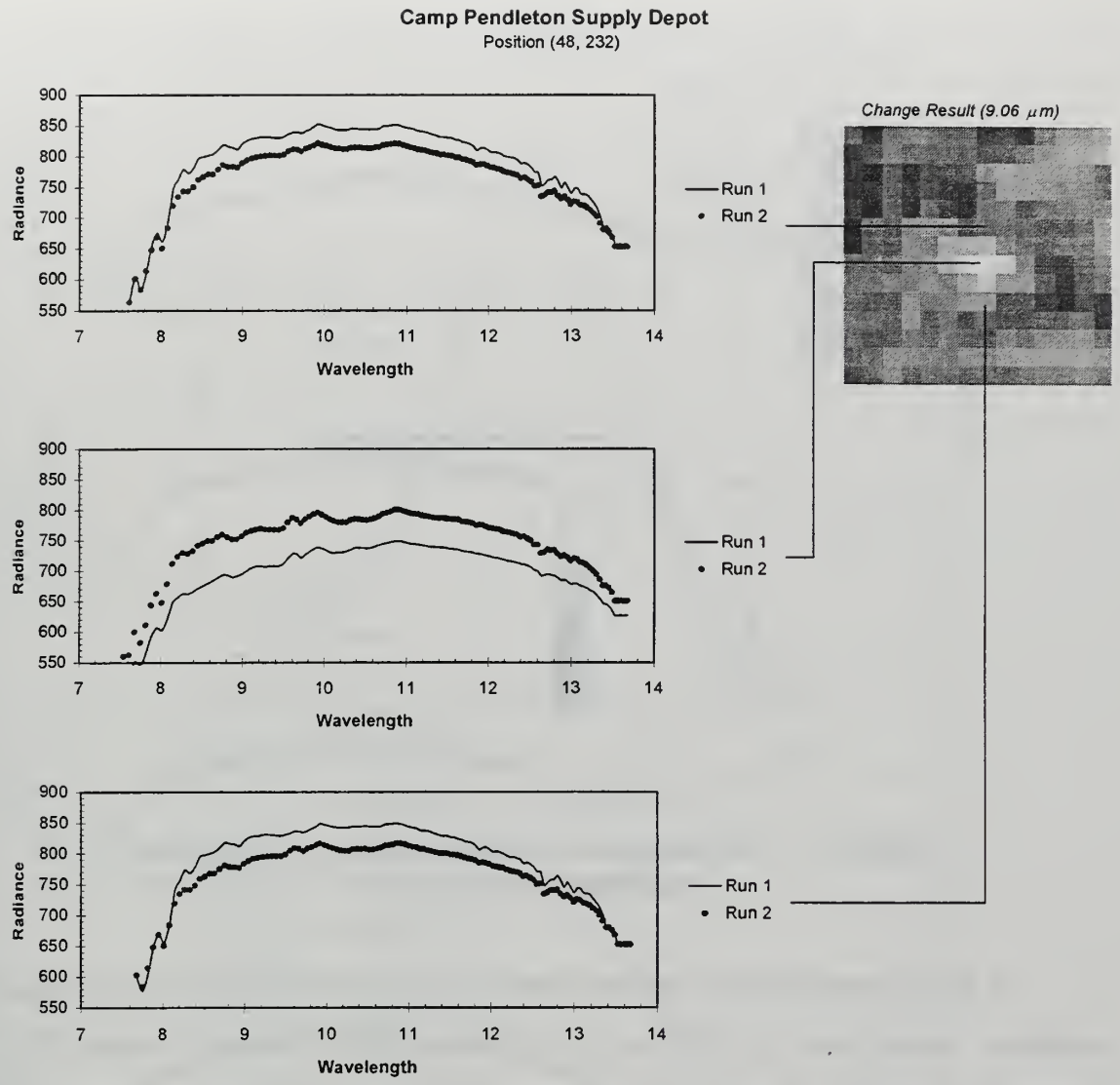

Figure 5.22: A sample of three spectra across change A in Figure 5.21.

Figure 5.23 is the histogram of difference band 51. The black histogram represents the pixels from the second change mentioned previously. The TBS for this change is less than one standard deviation and competes with a large portion of the background (presumably due to registration errors). In this case, it would seem that a one-dimensional histogram is insufficient for describing the change and that TBS may not be a useful measure in this context.

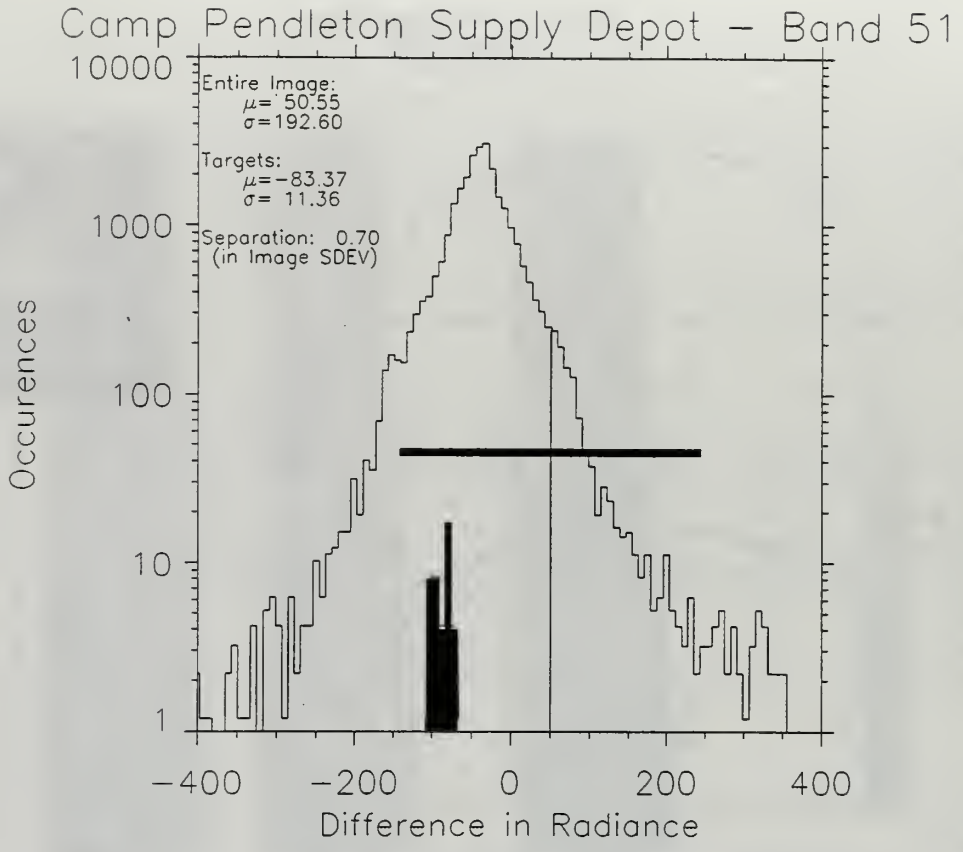

Figure 5.23: The histogram for difference band 51 of the Camp Pendleton change vecotor.

If this change identifies the introduction of an object into the scene, its spectral signature would likely be different from scene-to-scene and with respect to the surrounding material. Figure 5.24 illustrates five adjacent pixels across the horizontal dimension. A color version of this figure is available in Appendix B. The first two pixels appear to be both spectrally and radiometrically similar from run 1 to run 2, and the last pixel appears to be spectrally similar but radiometrically dissimilar. The third and fourth pixels are identified as change pixels Figure 5.21. In both pixels, there is a broad spectral feature at band 28 (9.06 μm) present in run 2 that is not present in run 1. It is interesting to note that this appears to be a similar spectral feature to that of the U.S. camouflage in the CARD SHARP data. It is likely that this is the same type of material (perhaps a synthetic fabric). A lack of ground truth for these data preclude confirmation.

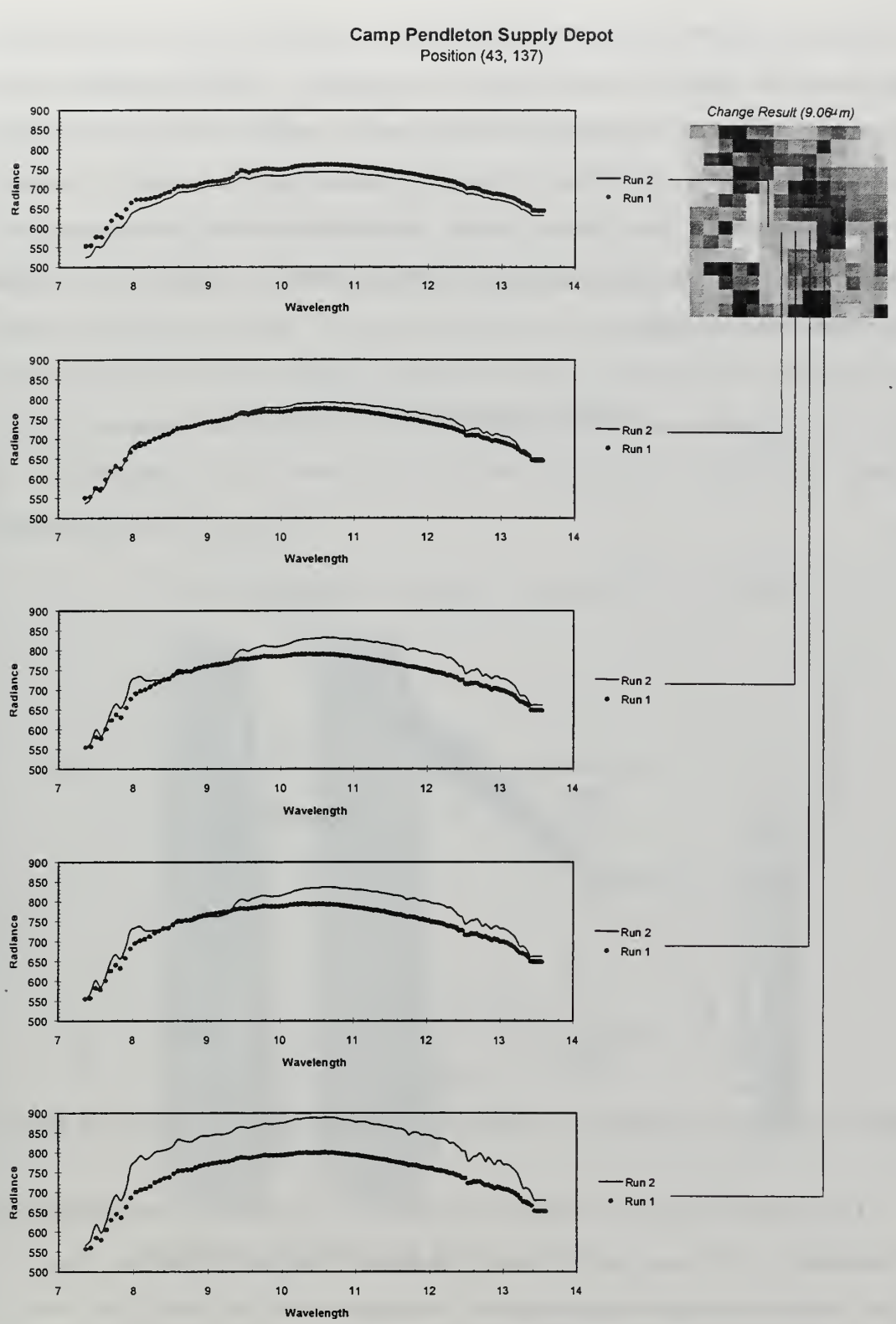

Figure 5.24: A sample of five spectra across change B in Figure 5.21.

Since a spectral feature is definitely present at band 28, it now makes sense to compare bands 28 and 51 in a two-dimensional scatter plot. Figure 5.25 shows a strong linear relationship in the two difference bands, but two small groupings of pixels fall below the background. The leftmost cluster represents "spectral changes" caused by gross misregistration. The rightmost cluster represents the change of interest. This suggests that there is spectral change present at this location. A color version of Figure 5.25 is available in Appendix B.

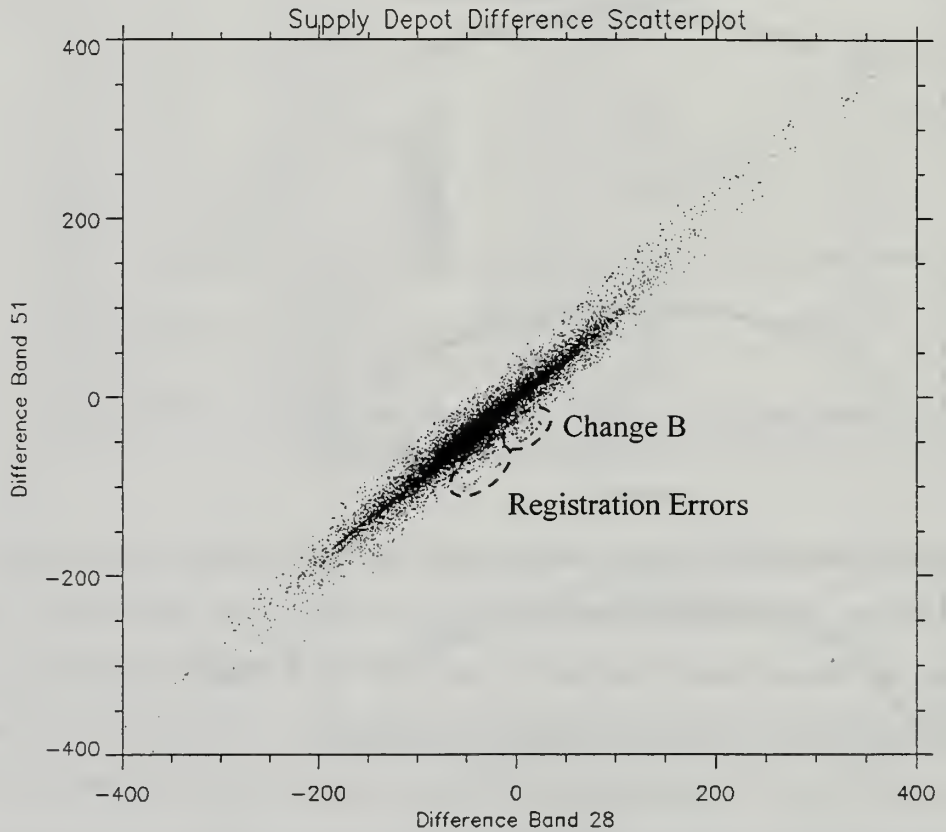

Figure 5.25: The two-dimensional scatter plot comparing difference bands 28 and 51.

The spectral change is not readily discernable in the standard difference bands, but it is discernable when comparing two bands that enhance the spectral feature. Figure 5.25 explains why a one-dimensional histogram is inadequate in this case. The change is located at the center of the distribution when looking at the data from either band.

However, the change is very discernable when both bands are included in the analysis and the axes are rotated 45°. Therefore a more useful change image could be obtained by transforming these two difference bands into principal components. Figure 5.26 displays PC band 2 from a principal component transform of difference bands 28 and 51. The change is more readily identified in this change result. Figure 5.27 is the histogram for PC band 2. Rotating the axes improves the TBS by 730% (from 0.70 to 5.12). The change competes only with the registration errors. An improved registration process would further improve the change detection process. Figure 5.28 is a scatter plot of the principal component transform. A color version of this figure can be found in Appendix B. The changes are now above the background distribution which allows them to be distinguishable in PC band 2.

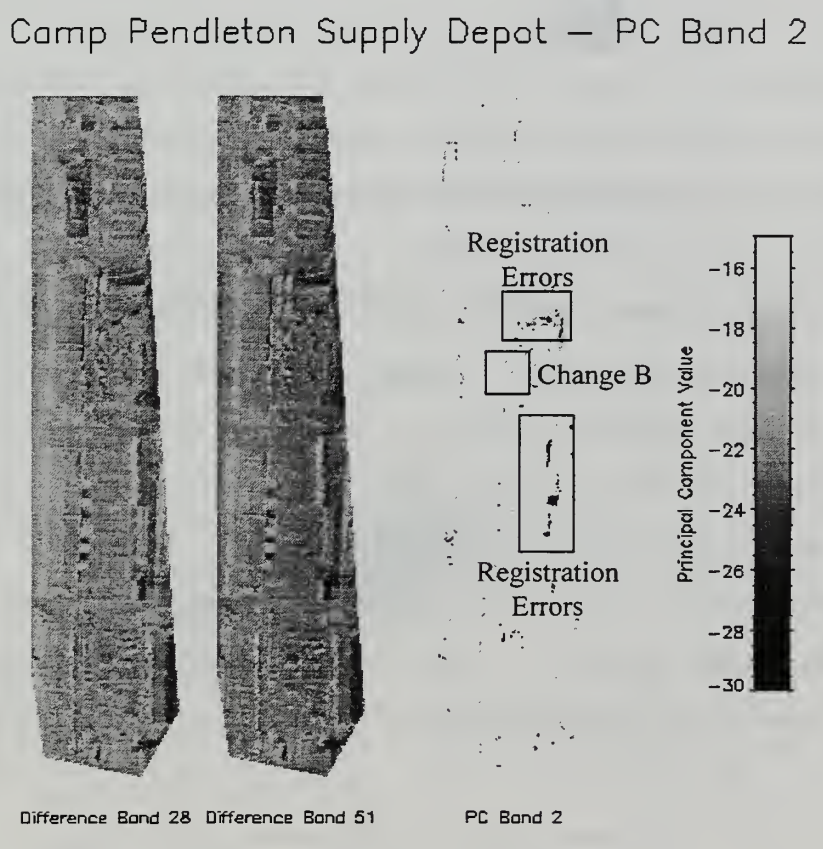

Figure 5.26: The change result for the Camp Pendleton data using the second principal component of the difference bands 28 and 51.

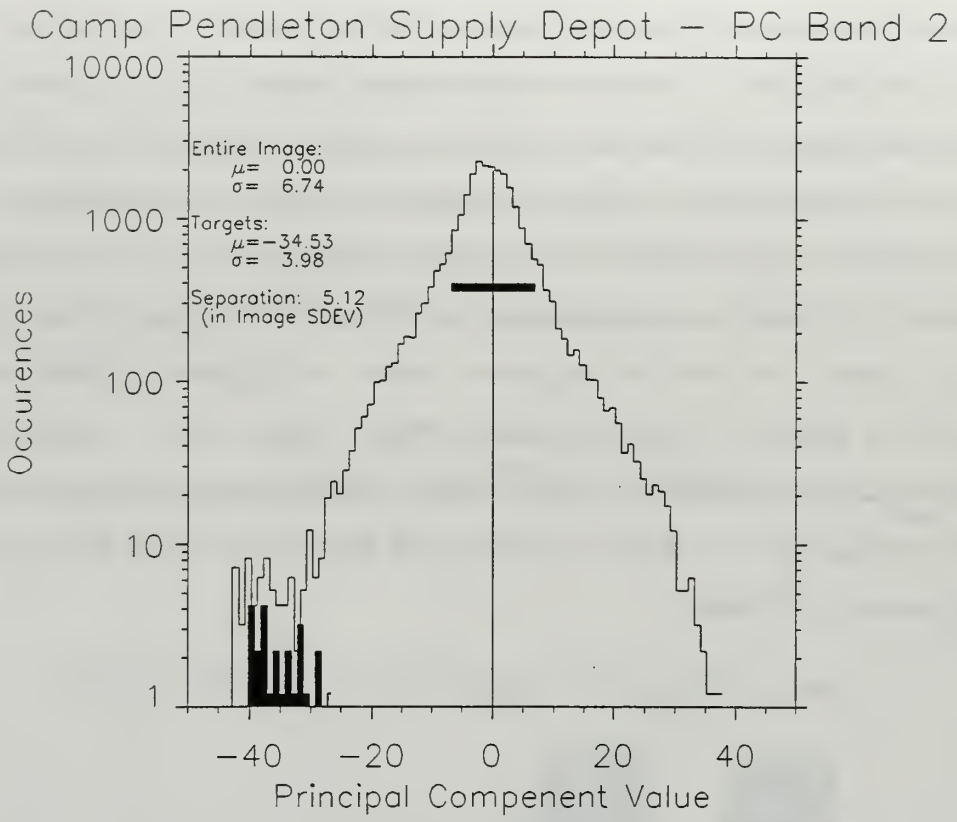

Figure 5.27: The histogram for the PCA result of the Camp Pendleton data.

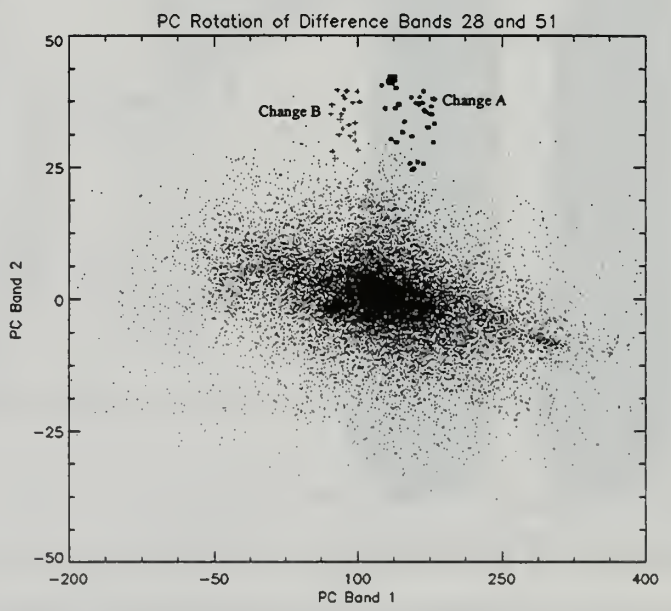

Figure 5.28: The principal component rotation of the scatter plot in Figure 5.25 The change class are now at the top of the plot.

2. Spectral Angle

A spectral angle result of the Camp Pendleton supply depot was obtained using the dot product method previously discussed. These results are displayed in Figure 5.29 and Figure 5.30. Color versions of these figures can be found in Appendix B. The left image in both figures is the spectral angle result while the right image is a comparison of run 1 and run 2 of band 54. The spectral angle image uses a hue, saturation, and value (HSV) color space to add a contextual dimension to the result. The spectral angle is described in hue (color) with violet being the lowest angle and red being the highest. Radiance for band 51 is described in value (brightness) while saturation remained at a constant maximum value throughout the result. Therefore, any red pixel in the image is associated with a high change in spectral angle regardless of its brightness. The band comparison uses complimentary colors (blue and yellow) to describe their relationship. For example, a pixel with a high value in run 2 but a low value in run 1 will have a blue tint while a pixel with a high value in run 1 but a low value in run 2 will have a yellow tint. Pixels that appear neutral will have the same value in both runs.

Again this result demonstrates the difficulty in distinguishing genuine change from registration errors; however both changes previously discussed can be identified in Figure 5.29 (available in color in Appendix B). Change A, caused solely by thermal differences, can be seen as a difference in radiance (brightness value) but has a low spectral angle (hue). This supports the previous assertion that spectral change did not take place at this location. Change B, which was associated with a spectral difference, has a higher spectral angle indicated by its yellow hue. For the Camp Pendleton data, the spectral angle technique is sufficiently sensitive to detect spectral change which demonstrates that familiar techniques can be applied to spectral thermal data.

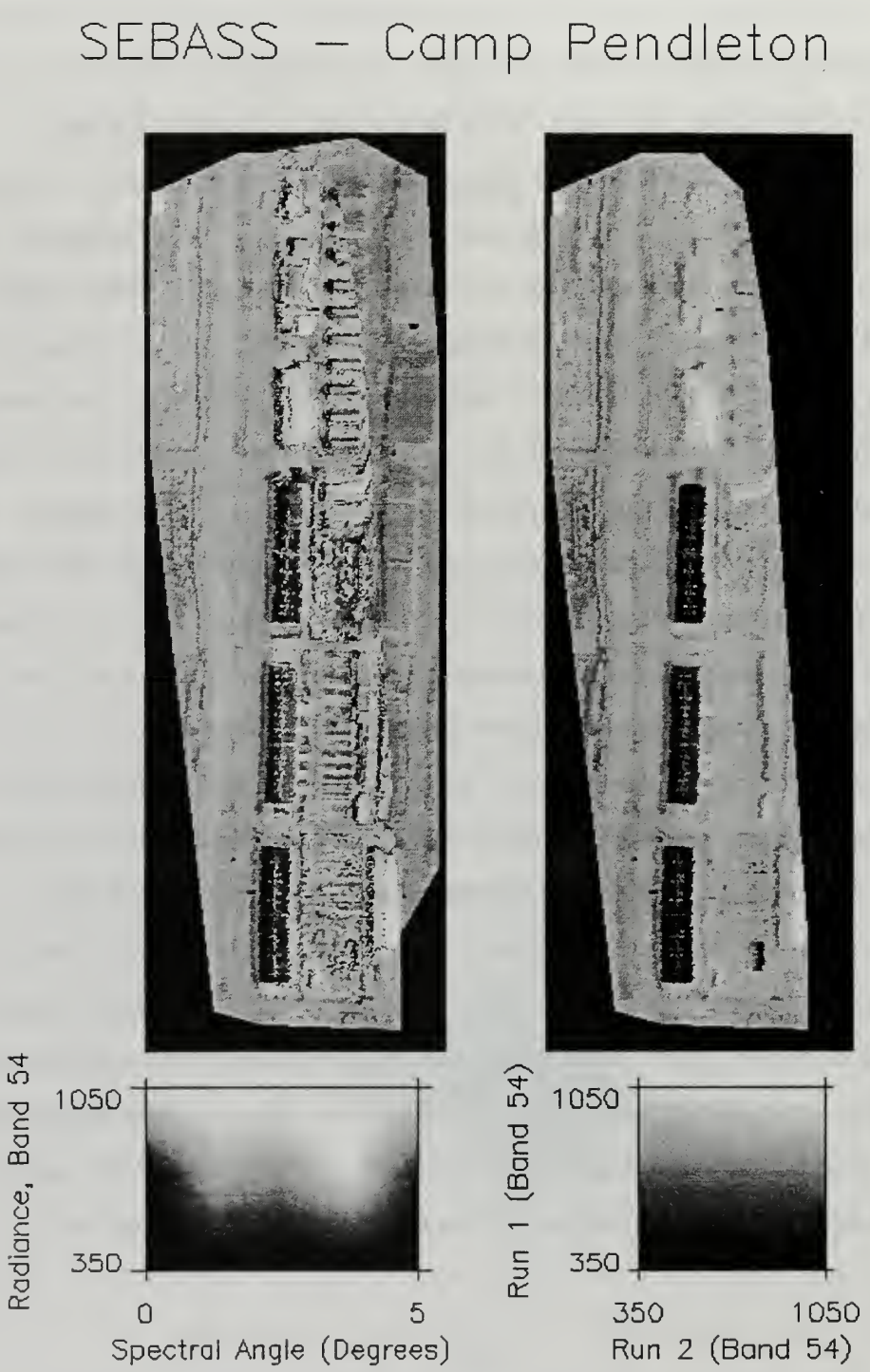

Figure 5.29: Spectral angle result for the Camp Pendleton data.

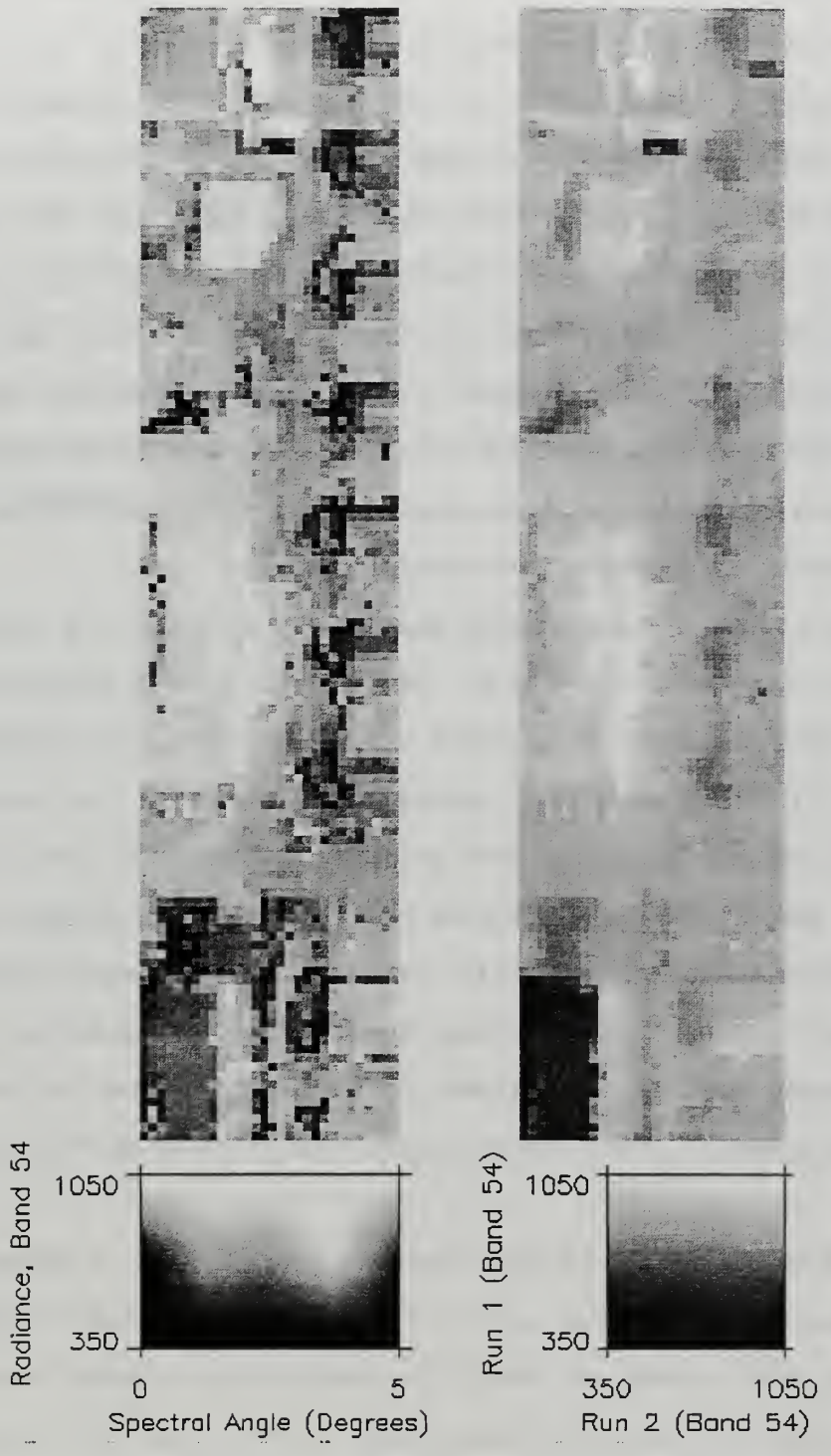

Figure 5.30: A tighter view of Figure 5.29.

3. Registration Errors and False Detections

To maintain radiometric integrity of the data, both roll correction and registration used nearest neighbor operations. This has the effect of "moving" a pixel to a new position, but since a pixel cannot be moved a fraction of a step, roundoff errors were introduced. This is best illustrated using the dot product result of the supply depot. At first glance, it would appear that there are several changes (depicted as red in Appendix B in Figure 5.29), but it quickly becomes obvious that detection along sharp edges (such as building rooftops) are caused by registration error. It is easy to identify and ignore false detections caused by edges which leaves a small number of detections remaining. It would seem probable that these are true detections, but as demonstrated earlier, genuine spectral changes are occurring at smaller spectral angles while pixels with larger spectral angles appear still to be associated with registration errors.

Figure 5.31 can be used to further examine such a detection. A color version of this figure can be found in Appendix B. The maximum detected change occurs near a building and may be a large vehicle parked next to the building. To examine the result more closely, Figure 5.31 presents the spectra from three pixels. It is obvious from the plots that the spectra from the first pixel are nearly identical. The same is true for the spectra from the third pixel. The second pixel, the maximum change, contains two dissimilar spectra which would suggest the presence of spectral change; however, there is a high degree of similarity between the spectrum in run 1 of pixel 2 and run 1 of pixel 3. Likewise, spectral similarity exists between run 2 of pixel 1 and run 2 of pixel 2. This suggests that registration errors and not spectral change are the probable cause of this detection.

This demonstrates that the largest spectral angles are mostly associated with false detections since registration errors can have a dramatic effect on pixel dissimilarity. Dai and Khorram (1997) quantify the effects of misregistration on change detection. With respect to Landsat TM data, they determine that, in order to limit the change detection error to less than 10%, it is necessary to register images to within one fifth of a pixel (a

registration accuracy of 0.1934 pixel). Changes of interest must then occur at lower spectral angles. Figure 5.32 illustrates such an example. Note that the roof of the warehouse is depicted as green. This equates to a spectral angle of approximately three degrees. The surrounding pavement is depicted as cyan which equates to a spectral angle of approximately two degrees. In this case, the higher spectral angle is cause by a decrease in rooftop temperature while the pavement temperature remains relatively constant. A color version of Figure 5.32 is included in Appendix B.

Registration errors caused primarily by the aerial platform from which the data were collected confound the change analysis and make it difficult to interpret. It is likely that change detection will be more useful in analyzing data from a space-based platform once one is available.

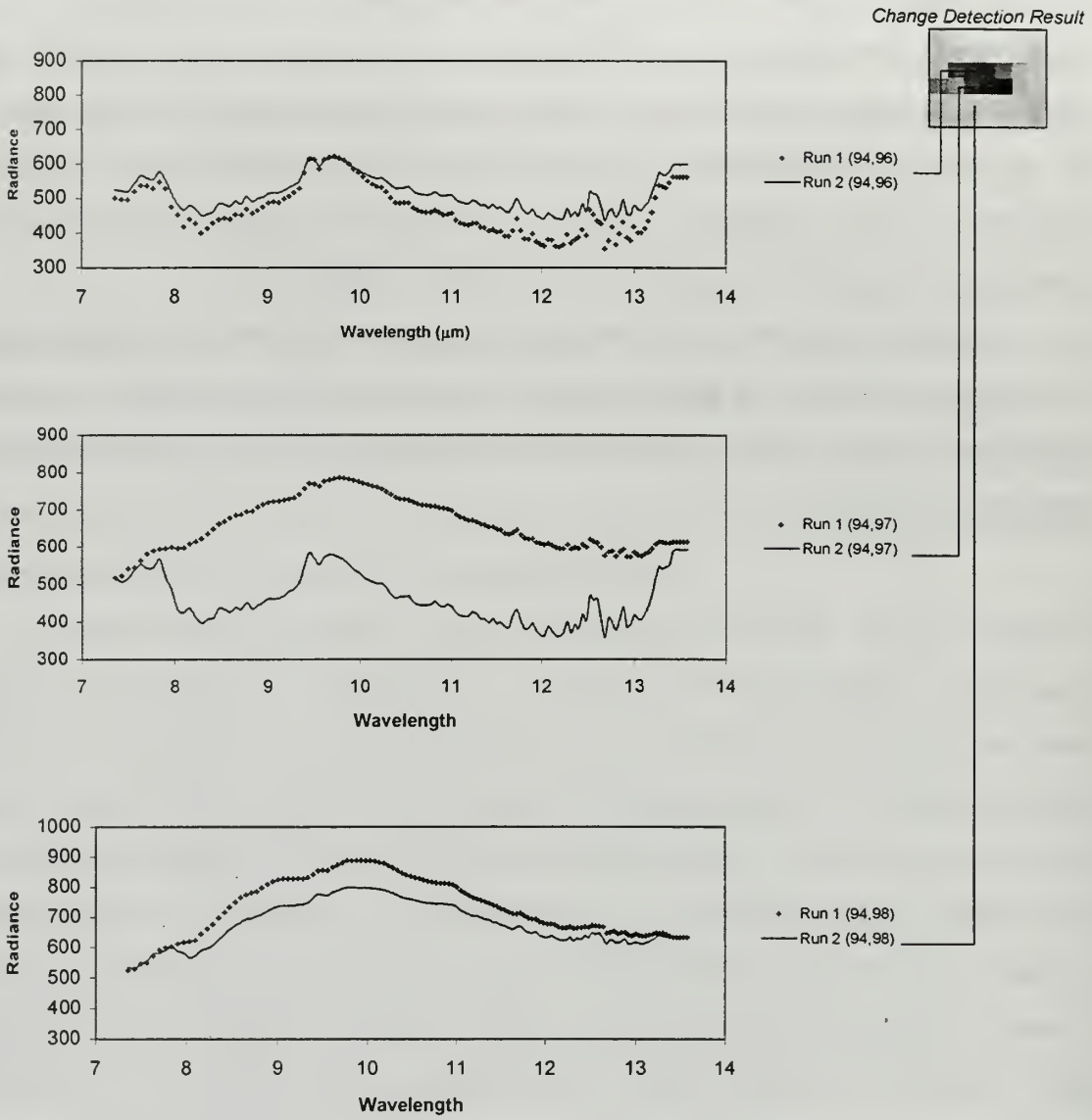

Figure 5.31: A sample of spectra from pixels that exhibit high change in the spectral angle result.

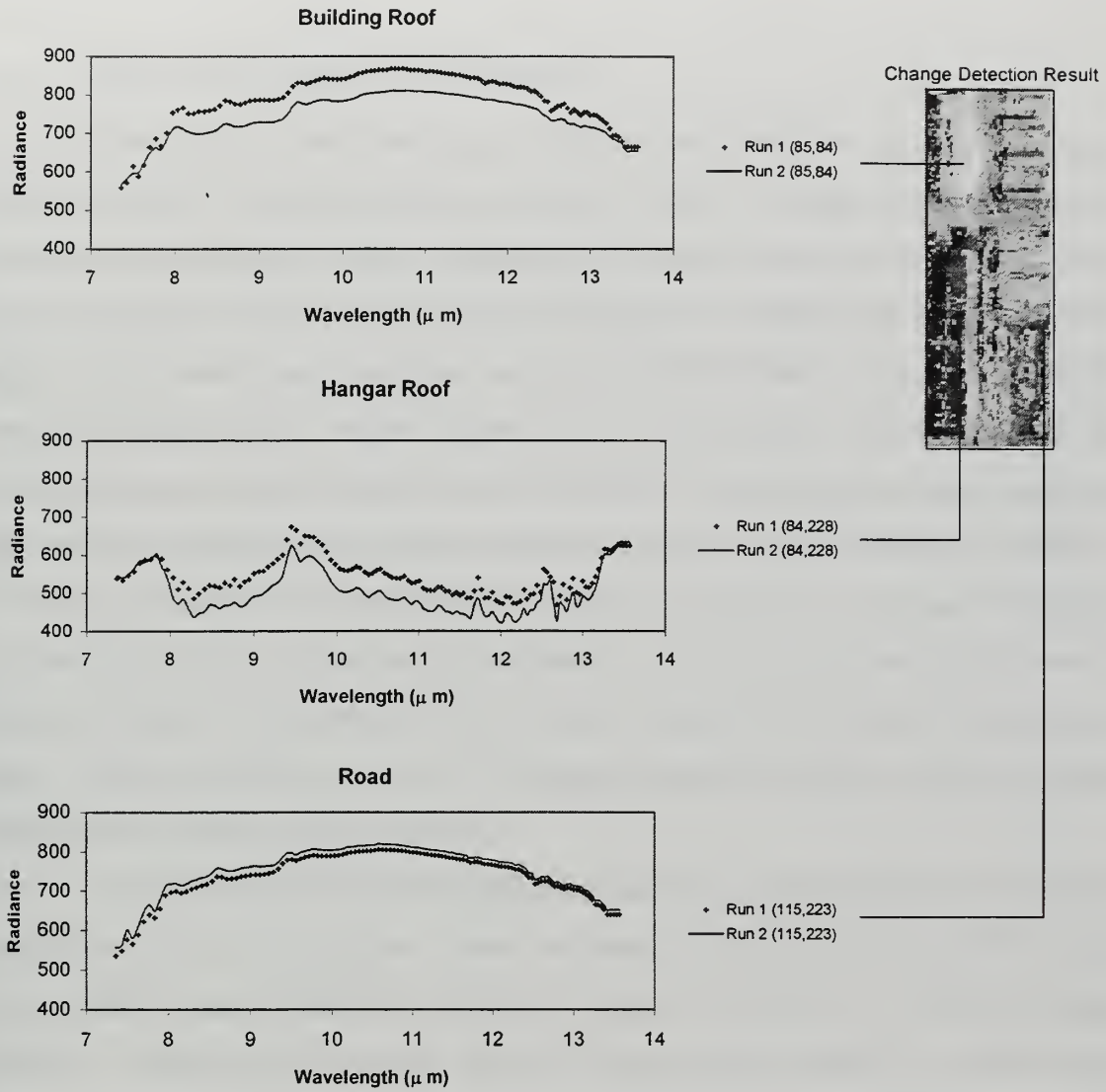

Figure 5.32: A sample of pixels representing varying degrees of change

VI. RESULTS

A. SEBASS INSTRUMENT AND DATA

SEBASS has demonstrated some utility in the LWIR for atemporal anomaly detection (Collins, 1996 and Smith and Schwartz, 1997). Collins (1996) was able to discriminate camouflaged military vehicles in a desert environment using techniques normally applied in the reflective portion of the spectrum. Smith and Schwartz (1997) applied similar techniques to an initial analysis of CARD SHARP data and successfully detected uncamouflaged vehicles. Figure 4.2 not only depicts vehicle locations but demonstrates that a single stretched band is sufficient in providing the same result, and that the discriminating factor is thermal rather than spectral. Later work by Schwartz, *et al* (1997) concluded that anomaly detection in this environment can be done successfully. The utility of LWIR spectral imagery for support to military operations (SMO) may be somewhat limited since pronounced spectral features are not as prevalent in the emissive regions than in the reflected regions. This does not negate the need for a thermal spectral system which enables night exploitation.

The CARD SHARP collect highlighted instrument inconsistencies which made spectral change detection difficult. Small variations in gain across the LWIR FPA made it impossible to use hypercubes converted to apparent emissivity for spectral change detection. Without such a data set, spectral changes could not easily be isolated from thermal changes. Since thermal changes tend to overpower spectral changes, analysis of the combined data was prohibitive. SEBASS is undergoing continuous improvement in these areas which should make apparent emissivity more reliable in the future.

B. EVALUATION OF SPECTRAL CHANGE TECHNIQUES

Consideration of advanced spectral change detection methods was eliminated from the study based on the low quality of both sets of data. Instead, an in-depth

characterization of thermal spectral change was more relevant. The techniques used in this study required a high degree of *a priori* knowledge to sufficiently explore the feasability of thermal spectral change detection. In order to properly employ these techniques, information about target position must be available. This is not an unreasonable assumption as anomaly detection can provide that information and could lead to the development of a target history for a given area. Essentially, change detection is the detection of new anomalies not present in the target history.

The target-to-background separation (TBS) proved to be a useful measure of spectral change as long as the targets could be identified prior to analysis. By tracking the TBS at every wavelength, it became easy to identify which bands were spectrally significant for a given change. This could aid in selecting the appropriate bands to be used for visual (spatial) discrimination. The spectral features observed in the CARD SHARP data were on the order of one percent of the total observed radiance; however, this was not substantially above the observed noise. Even though the NESR was 0.1 μflicks, thermal fluctuations, registration errors, and gain inconsistencies dramatically reduce the SNR.

Once spectrally significant bands were identified, 2-D scatter plots were useful in classifying the type of spectral change and descriminating spectral from thermal change. The comparison of change A (thermal) to change B (spectral) in the Camp Pendleton supply depot is an excellent example of this technique's sensitivity to spectral differences. Although the object at change B showed no appreciable change in temperature that could be detected in a one-dimensional histogram, it was very discernable using a scatter plot of two significant bands. It is also important to note, however, that change B occurred where there was no target history. The scatter plot helped to identify it as a potential target before TBS could be used as a measure of spectral dissimilarity.

TBS was not inappropriate in the case of the Camp Pendleton data as long as it was correctly applied. Applying TBS to individual bands provided little additional

information, but applying it to the most discernable principal component of several spectrally significant bands improved change detection by more than 700% increasing the SNR by more than a factor of five. Registration errors still overpower genuine changes and preclude practical use of these techniques until such errors can be reduced to manageable levels.

The spectral angle technique was effective in isolating spectral changes. The spectral angle comparison of change A and change B in the Camp Pendleton data proved that subtle spectral change could be discerned from thermal change. The thermal difference in the two runs at change A of the Camp Pendleton supply depot scene increased radiance by 10% while the spectral difference at change B increased radiance by only 5%, yet the difference in spectral angle between the two changes was approximately 2° - a difference of 40% in favor of the spectral change. This suggests that spectral angle will be a useful tool for change analysis.

C. THE UTILITY OF THERMAL DATA FOR CHANGE DETECTION

Because an object's temperature can confound spectral analysis, using thermal hyperspectral data for change detection may not be the preferred method for most applications. However, the findings in this study prove that thermal spectral change detection is possible.

Monitoring most military operations with thermal hyperspectral imagery comes with limitation. Pertaining to CC&D, there are few spectral features available for exploitation in the LWIR region. Most healthy vegetation acts as a blackbody from 8 to 14 μm. The woodland camouflage used in CARD SHARP acted in a similar manner with only one minor spectral feature at 9.16 μm in the U.S. camouflage. The thermal inertia of the uncamouflaged tanks varied greatly from the backgound which provided the primary input for the change detection. The Camp Pendleton data provided a spectrally rich environment suggesting that thermal hyperspectral data may be more useful in an industrial environment. It is unclear at this time if relfective spectral change detection

would provide better results; however, reflective sensors are useless at night thus maintaining the need for the same capability in the LWIR region.

D. REQUIREMENTS FOR IMPROVED CHANGE DETECTION

This study indicates that spectral change detection could be useful, but further improvements must be made before an imagery analyst could employ such techniques. It is difficult to quantify current registration accuracy considering that future platforms will likely be space-based hopefully eliminating the introduction of attitude errors. The problem would then be similar to that already encountered with Landsat multispectral imagery. The 0.1934 pixel registration accuracy requirement for TM (Dia and Khorram, 1997) may be sufficient; however, the push to conduct subpixel analysis may be more restrictive.

The NESR for SEBASS is typically less than 1.0 μflick which equates to a SNR of greater than 800; however most thermal signatures are within one percent of the total signal. In order to accurately detect a one-percent signature, the *signature*-to-noise ratio must be at least 10 thus requiring a SNR on the order of 10^4. This was evident in the CARD SHARP data where it was extremely difficult to identify small spectral variations in a heavily vegetated area. Larger spectral changes were present in the Camp Pendleton data. Ignoring thermal fluctuations and registration errors, a 40 μflick spectral change was detectable. This equates to a *signature*-to-noise ratio of 40. The spectral change in these data would have been an easily discernable signature if it were not for the high number of false detections. Registration errors and thermal changes overpowered the spectral changes reducing the SNR from 40 to 0.5 which emphasizes the importance of isolating emissive spectra independent of temperature and of reducing errors caused by misregistration. Therefore, external errors have the greatest impact on the effectiveness of change detection, but NESR must further be reduced in order to detect even smaller changes.

VII. CONCLUSION

This study indicates that detection of thermal spectral change is possible given that spectral features are available and the data are relatively free of thermal and registration-induced noise. With a great deal of effort, spectral change was isolated in both the CARD SHARP and Camp Pendleton data. The use of TBS, scatter plots, and PCA on selected difference bands were effective analysis tools in detecting and identifying change. However, analyses of these data were complicated by the confounding effects of temperature and the high number of false spectral changes detected due to registration errors. Producing an accurate and reliable emissive data set and improving the registration process will greatly affect interpretability to the point were imagery analysts may find hyperspectral change detection a useful tool.

Before this can be done, many small steps must be taken to improve the quality of the imagery and the reliability of the techniques. All hyperspectral sensors must continue to improve in terms of SNR, reliability, and overall data quality. Further study is required to determine where the point of diminishing returns exists for various measures of image quality with regard to the most sensitive change detection techniques. Also, further study is required in the analysis of emissive spectra independent of temperature. For various reasons, the data in this study did not produce reliable emissivity images. Once image and calibration data are available to this end, a comparison of results between temperature dependent and independent data would be useful to determine the need for strictly emissive spectra.

In the end, this study has provided useful insight into the sensitivity of simple change detection methods for discriminating small spectral changes. While the data, provided the worst case scenario, it was still possible to make an acceptable identification. Future research on higher quality data sets should further support this finding.

APPENDIX A. HYPERSPECTRAL ANALYSIS TECHNIQUES (STEFANOU, 1997)

	Technique	*A Priori* Knowledge	Purpose	Operation	Result
Principal Components Transform	*Principal Components Analysis (PCA)*	None	Image enhancement by transforming orginal pixel vector into a new vector with uncorrelated components ordered by variance.	Uses the eigenvectors of the image covariance matrix to assemble a unitary transformation matrix. When applied, this matrix creates l-band PC image with the most significant PC bands first.	Useful for discriminaton but not in identifying target spectra.
	Maximum Noise Fraction (MNF)	None	Same as PCA but orders PC bands by image quality.	Measure noise fraction as noice variance divided by signal variance. Noise variance is esbmated from a uniform observed background. The eigenvectors of the resulting matrix are applied to the image to obtain the MNF transform.	Useful for descriminaton but not in identifying target spectra.
	Standardized Principal Components Analysis (SPCA)	None	Removes unequal SNR in all PC bands.	Normalizes the variances of all PC bands to unity. This accounts for uneven individual-band SNR. Therefore, each band contributes equal weight to the analysis.	The image quality of each PC band is improved significantly - especially in the higher bands.
Matched Filter	*Simultaneous Diagonalization*	Scene Endmember Spectra	Produces a single-band image which contains abundance informabon of a particular target spectrum in every pixel.	Performs linear filtering on the hypercube to obtain a new image in which the original pixel vectors have been transformed by a filter vector which represents the desired endmember.	Single-band image results vary based on noise assumpbons (see OSP and LSOSP).
	Orthogonal Subspace Projection (OSP)	Scene Endmember Spectra	Same as SD Filter; however, the additive noise is assumed to be zero.	Applies a least sqaures orthogonal complement projector and then maximizes the SNR via a matched filter.	Some undesired enmembers may be emphasized over the target endmember. Target spectrum must be in greater than 5% abundance.
	Least Squares OSP	Scene Endmember Spectra	Reduces the effects of noise on OSP by using a least squares estimate of the noise thus converting the *a priori* model to an *a posteriori* model.	Decomposes the observations space into a signature and noise space and projects the observations into a signature space. Then OSP is used to eliminate undesisred signatures.	The improved SNR aids in better descriminating the target endmember.
	Filter Vector Algorithm (FVA)	Scene Endmember Spectra	Assuming linear endmember mixing, this algorithm attempts to demix the scene.	Relative abundances of each endmember in a pixel is determined by taking the inner product of a matched filter vector (designed for endmember abundance) with the observed pixel vector.	
Unknown Background	*Low Probability of Detection (LPD)*	Target Spectra	If a target spectrum occurs in the image with a low probability (subpixel level), undesired signatures can be esbmated directly from the data and eliminated.	A linear mixing model is used where the desired endmember abundance is set to zero in order to estimate the contribution of undesired endmembers. The undesired signatures are removed using an orthogonal complement projector operator leaving a single-band image representing relative abundances of the desired endmember.	The algorithm properly supresses the backgound in low-abundance scenes, but produces poor results when applied to high-abundance scenes.
	Constrained Energy Minimization (CEM)	Target Spectra	Relaxes LPD constraint of low target abundance.	Uses beam forming to deterimine a filter vector that produces single-band image representing a weighted sum of the responses at each of the spectral bands within the observed pixel vector.	Sucessful target detection appears to depend on the target spectrum used. CEM operators with less vanablity produce better target descrimination in the output image which depends only on the behavoir of the target pixel vector.
Limited Image Endmembers	*MUSIC-Based Endmember Identification*	Reference Spectra (Laboratory)	Employs the use of known "pure" reference spectra to compare with mixed pixels for endmember identification.	First uses a noise-whitened covariance matrix to determine the number of disbnct spectral signatures. Then forms an orthogonal subspace to all linear combinations of spectral signatures in the scene using principal eigenvectors. Then applies a noise subspace projection operator to a spectral library in order to identify endmembers.	Identifies pixels containing target endmembers.
	Partial Unmixing	Reference Spectra (Laboratory)	Reduces the dimensionality of the observabons by identifying the spectral bands on which the spectral reflectance is functionally dependent.	Using MNF, the intrinsic dimensionality of the data is determined. The observed spectra are projected onto the principal axes of the most significant eigenvectors.	Identifies pixels containing target endmembers.
	Spectral Angle Mapper (SAM)	Reference Spectra (Laboratory)	Determines the spectral similarity betweena reference spectrum and a spectra found at the pixel of an image.	Calculates an angular difference, in radians, between an observed pixel vector and a vector that represents the reference spectrum. The smaller the angle, the closer the match to the reference spectrum.	Produces a single band image where the lowest values in the image represent the closest matches to the target spectrum.

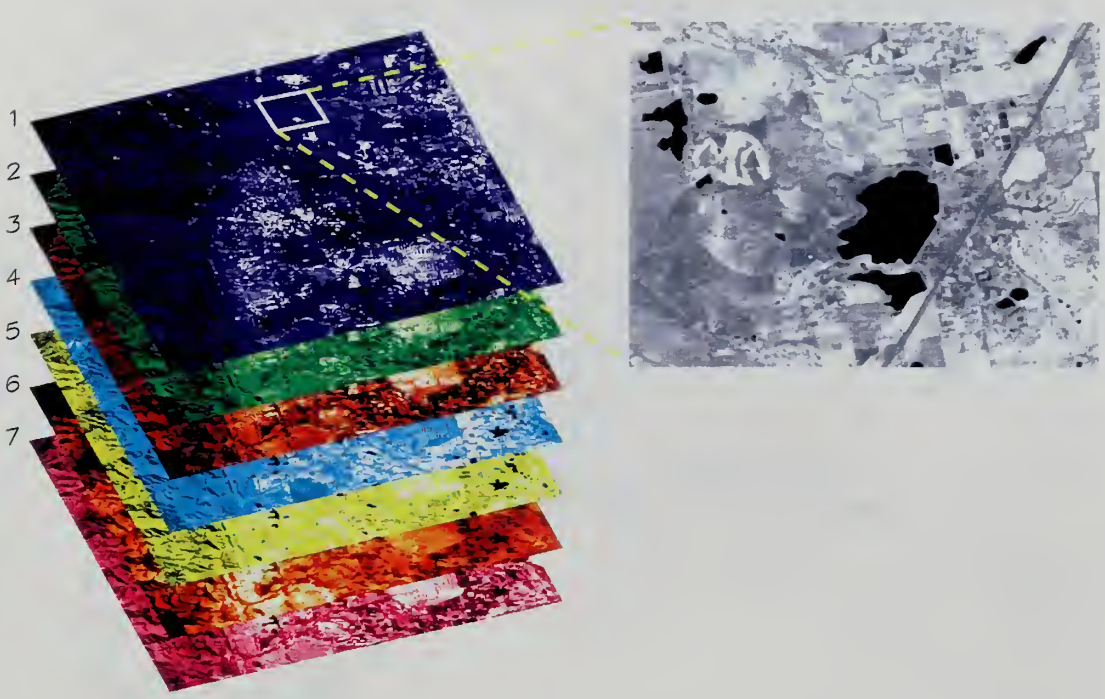

Figure 2.1: A subset of two Landsat TM images of Boulder, Colorado are used as examples in this chapter.

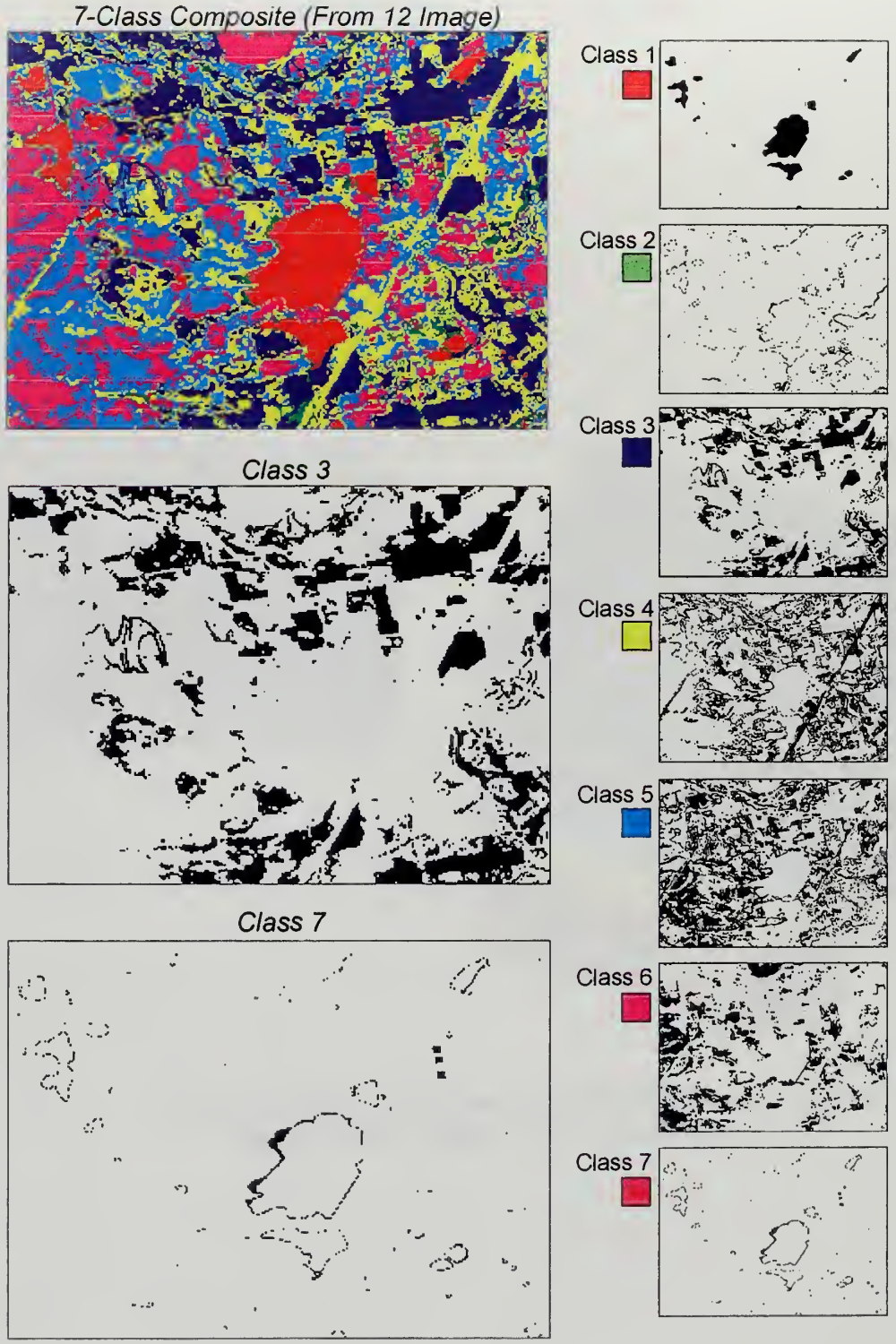

Figure 2.21: Direct multidate classification. The right side is a breakout of the various classes. Classes 3 and 7 contain change information.

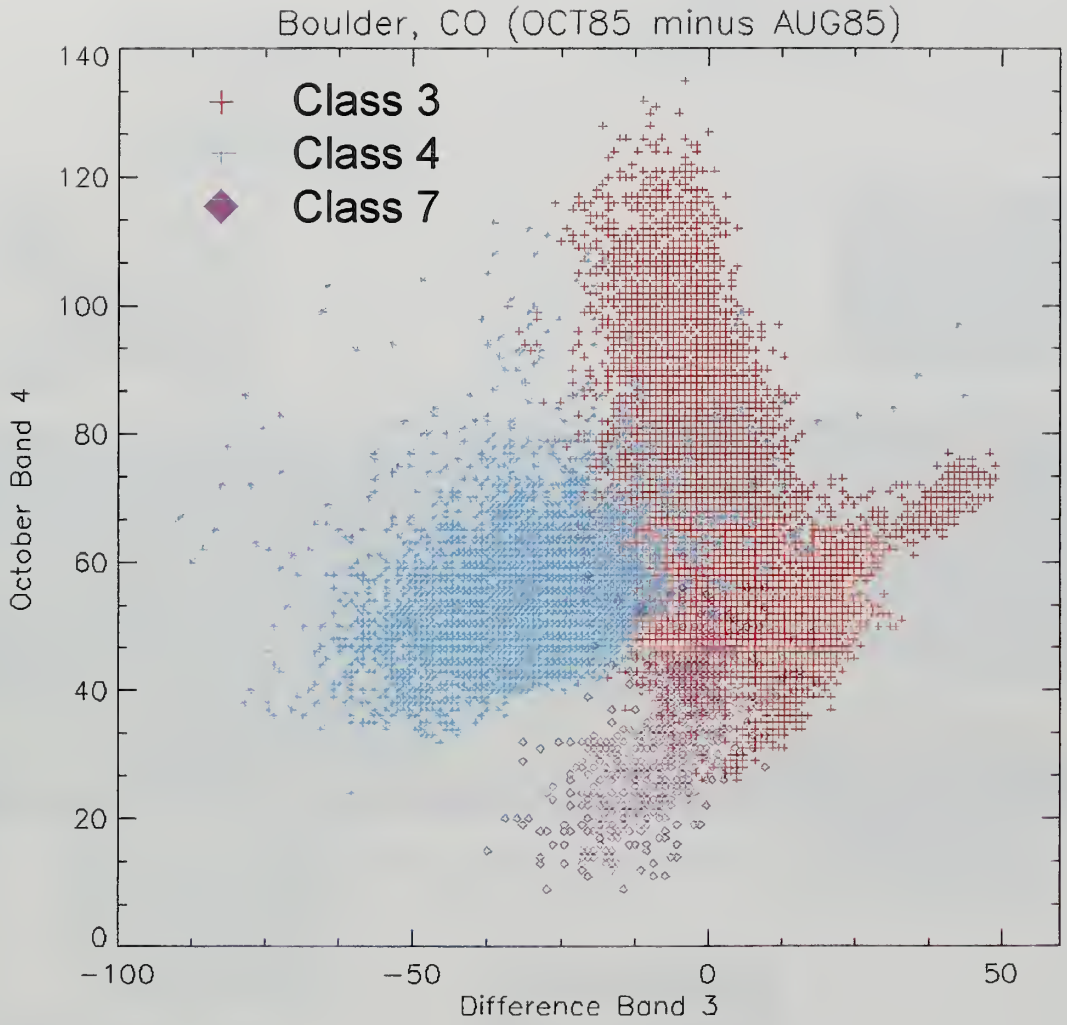

Figure 2.22: A scatter plot of three classes.

Figure 4.1: Site layout at Redstone Arsenal (from Smith and Schwartz, 1997).

Figure 4.2: Vehicle positions in the CARD SHARP field of view.

Figure 4.3: The M1E1 Abrams MBT positioned at site S1 with woodland camouflage.

Figure 4.4: The M1E1 Abrams MBT positioned at site S1 without camouflage.

Figure 4.5: A composite image consisting of Landsat TM (bands 1, 2, and 3), a color aerial photograph mosaic, and the two SEBASS images used for this study.

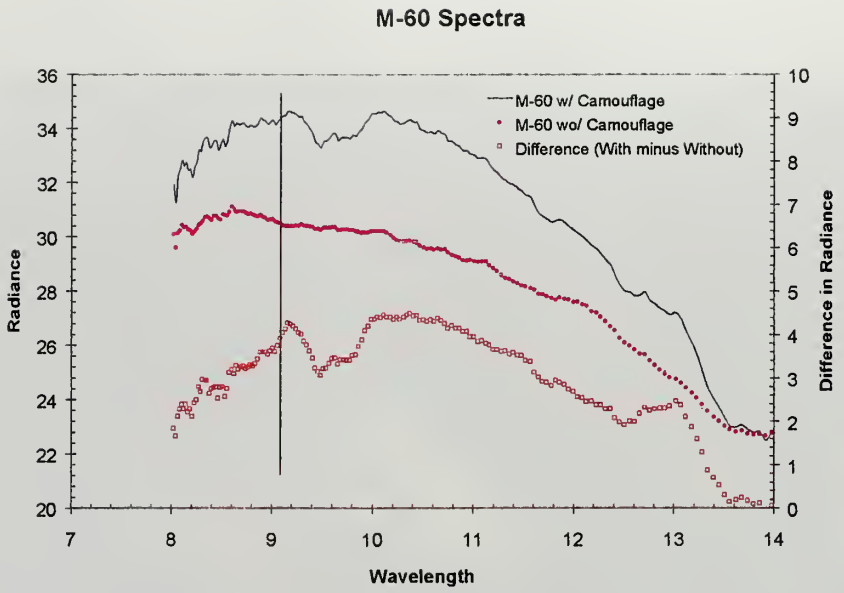

Figure 5.4: Ground truth spectra acquired during CARD SHARP for the M-60A MBT.

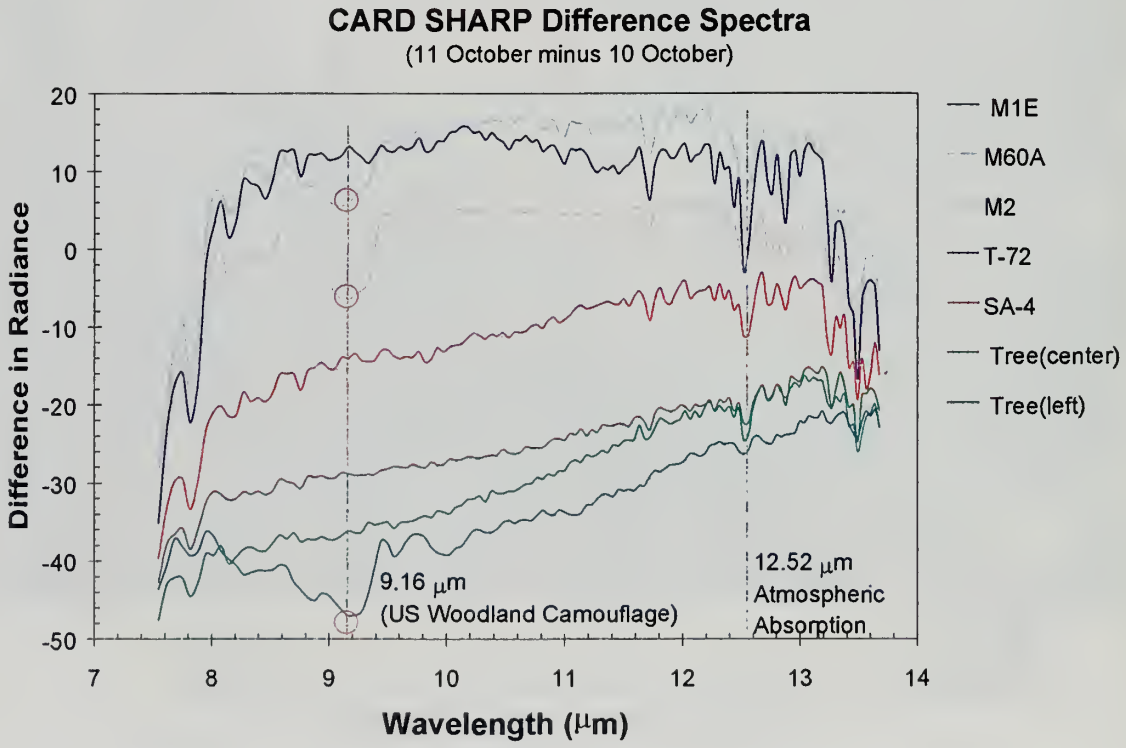

Figure 5.5: A variety of difference spectra produced by subtracting the spectrum at a given pixel location in the 10 October image from the spectrum at the same pixel location in the 11 October image.

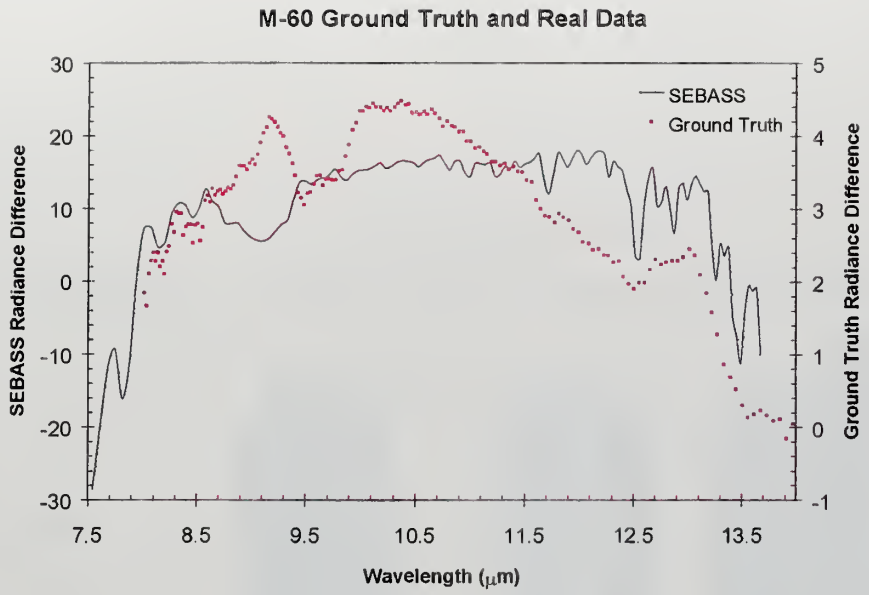

Figure 5.7: A comparison of SEBASS and ground truth *difference* data for the M-60A MBT with and without camouflage.

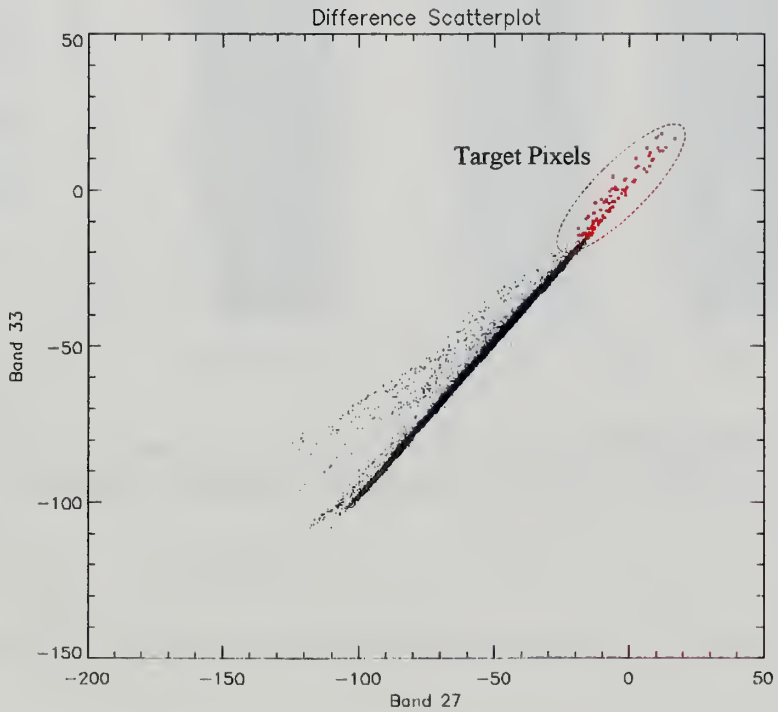

Figure 5.18: A scatter plot for CARD SHARP difference band 27 (9.16 μm) and band 33 (9.50 μm).

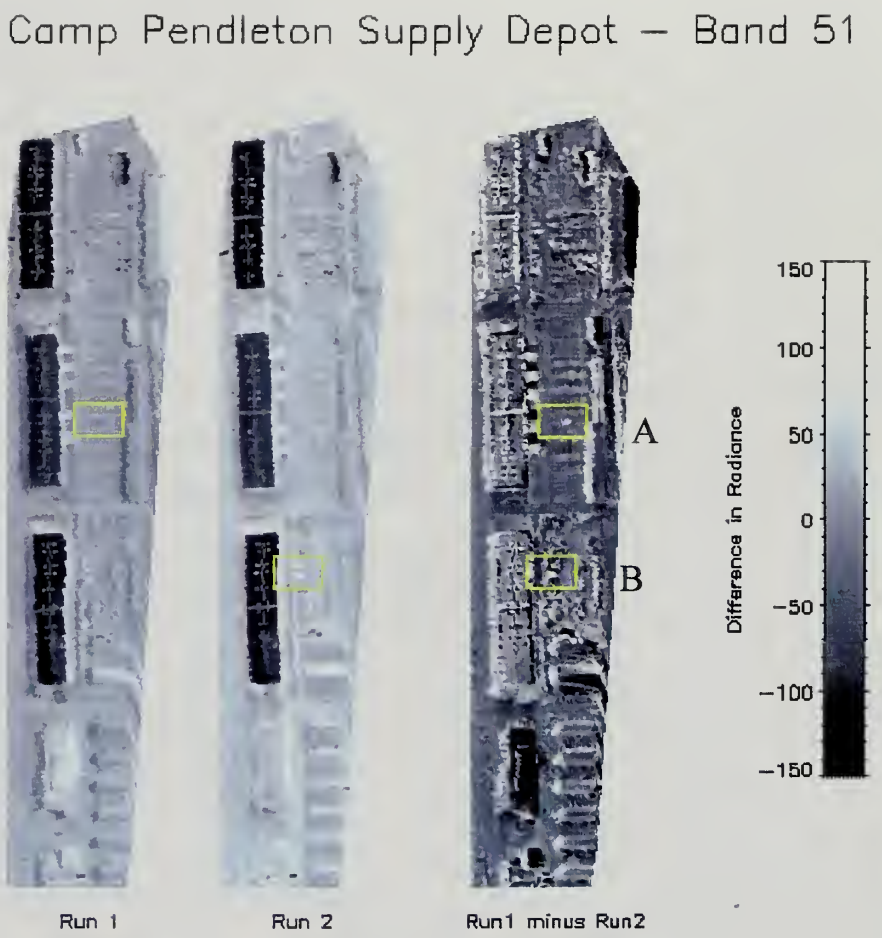

Figure 5.21: Image differencing result for band 51 (10.28 μm) of the Camp Pendleton data. Two genuine changes are indicated at A and B.

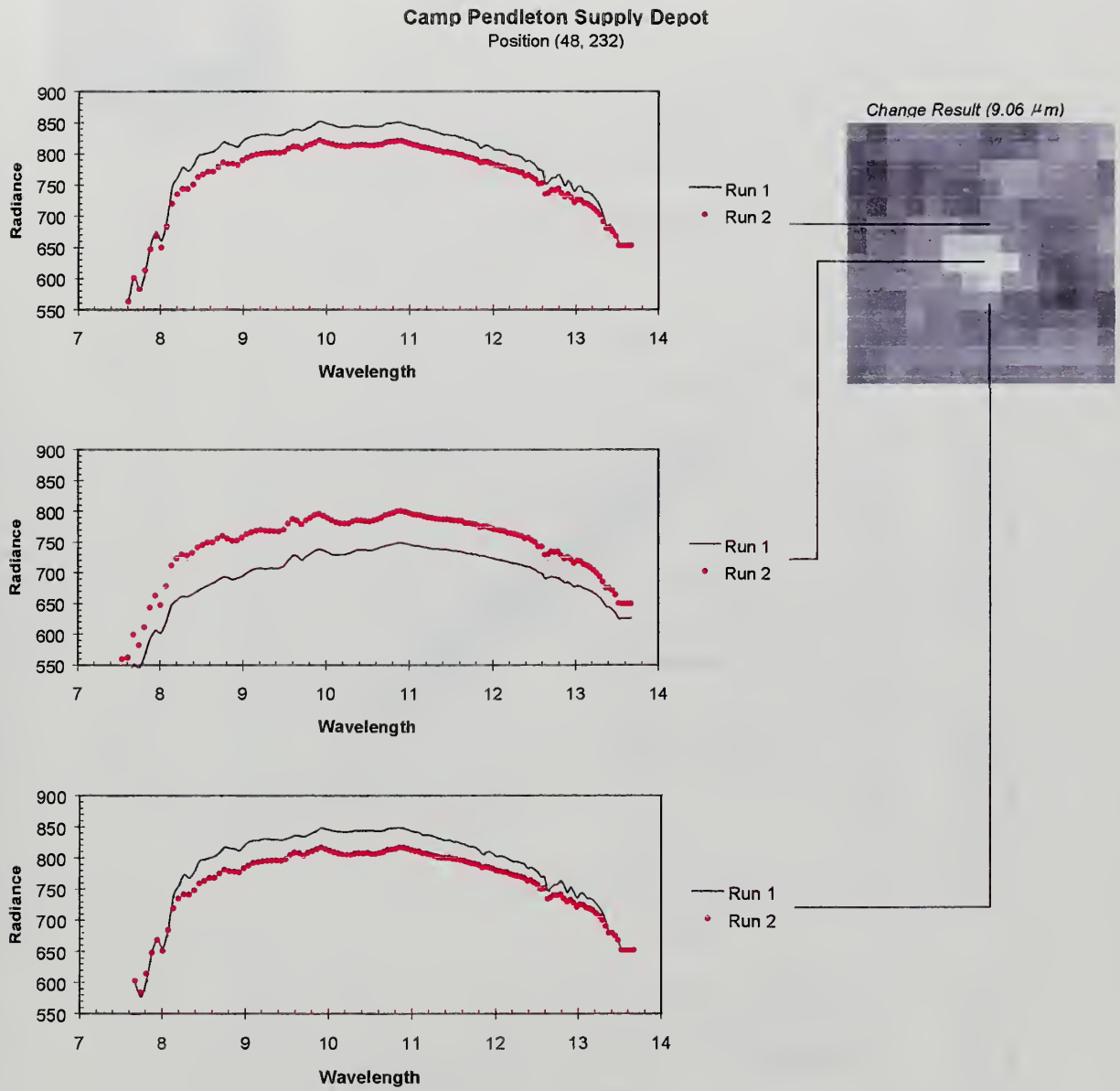

Figure 5.22: A sample of three spectra across change A in Figure 5.21.

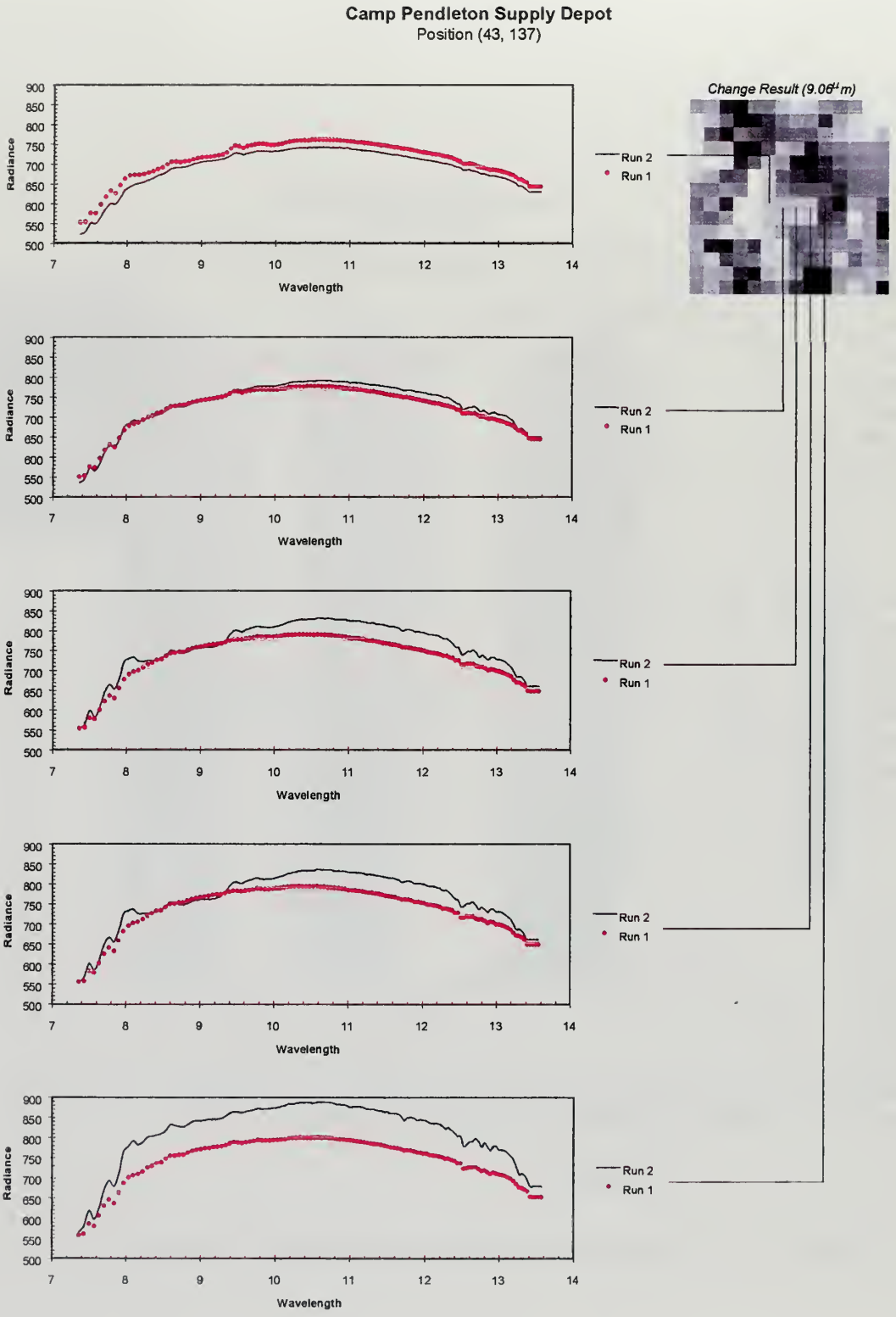

Figure 5.24: A sample of five spectra across change B in Figure 5.21.

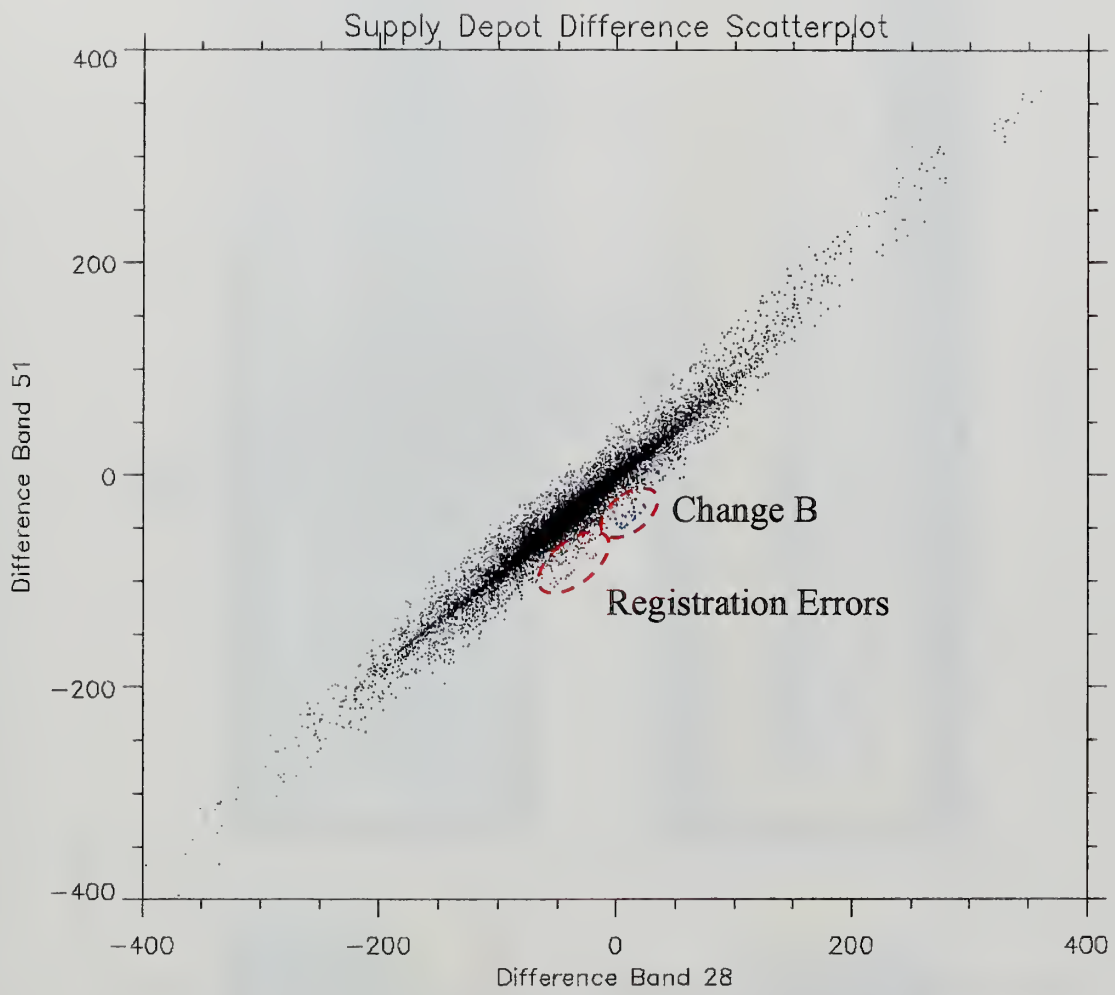

Figure 5.25: The two-dimensional scatter plot comparing difference bands 28 and 51.

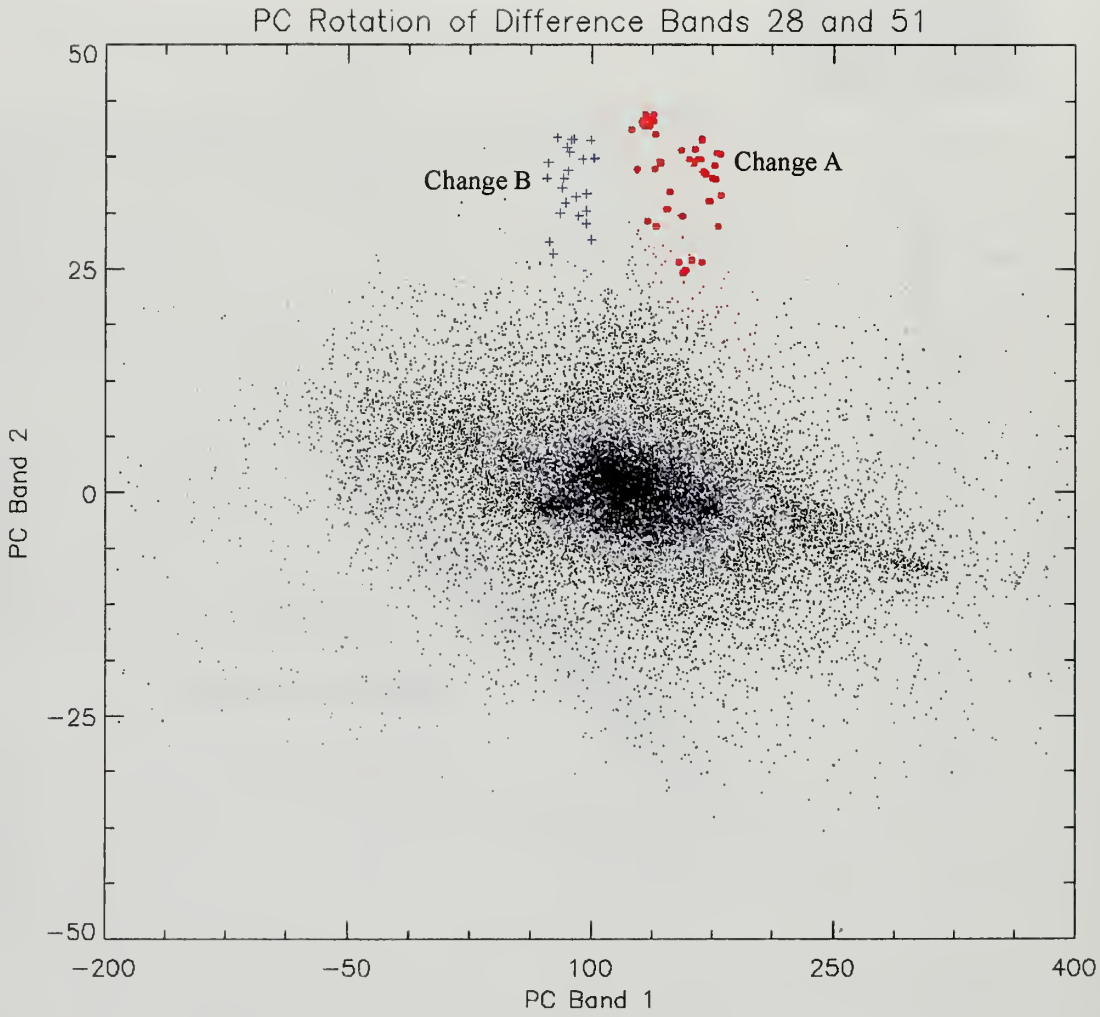

Figure 5.28: The principal component rotation of the scatter plot in Figure 5.25 The change class are now at the top of the plot.

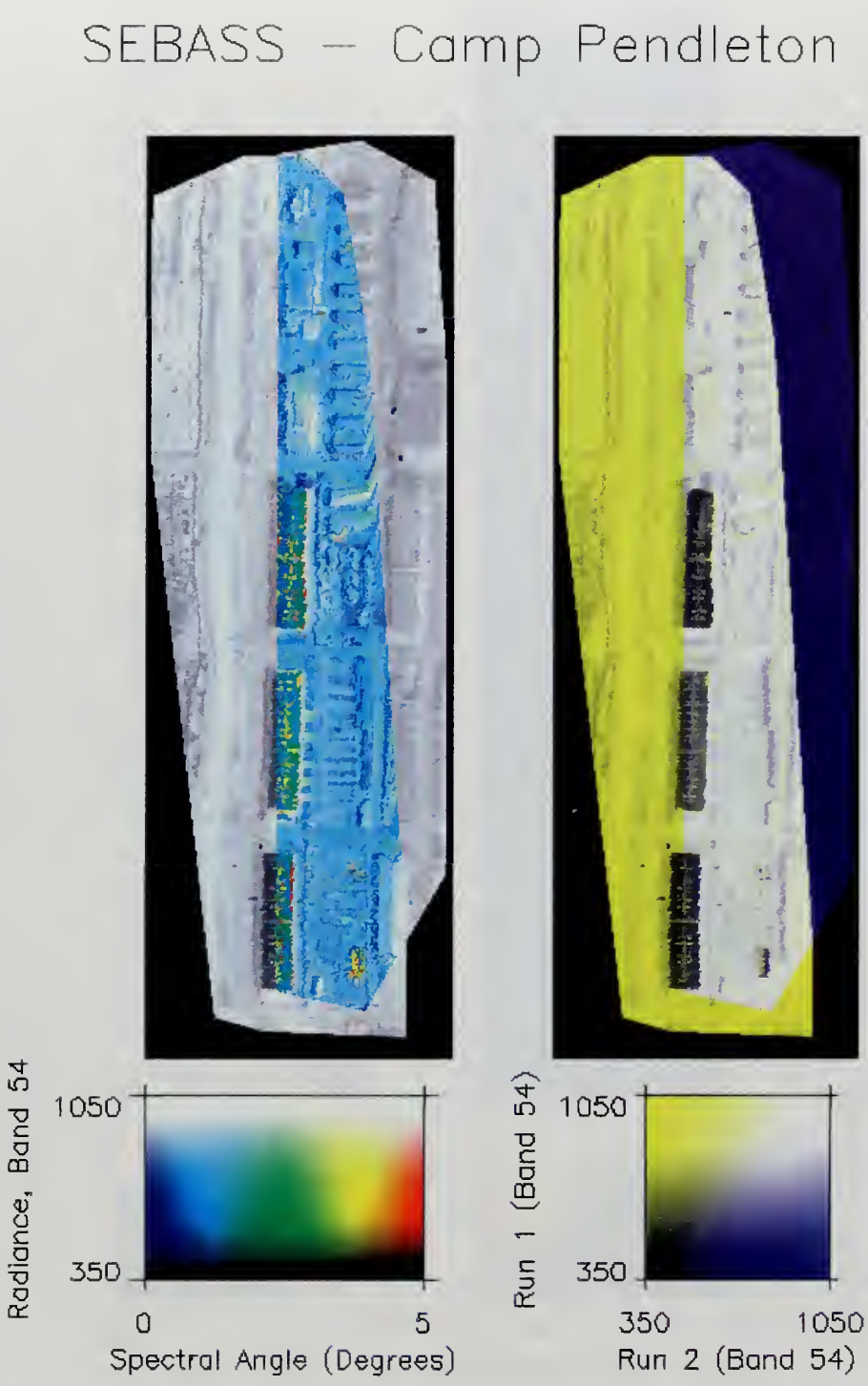

Figure 5.29: Spectral angle result for the Camp Pendleton data.

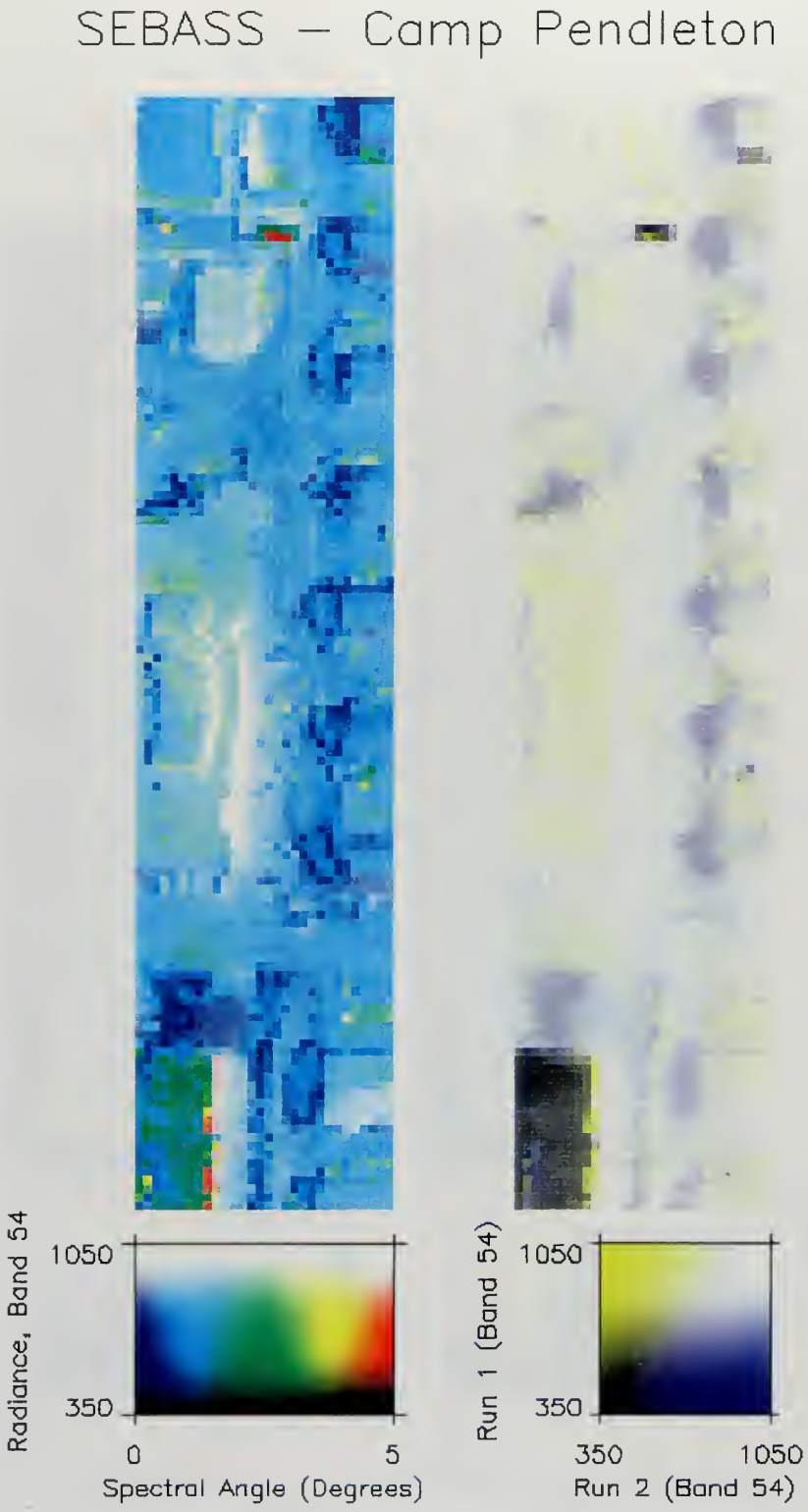

Figure 5.30: A tighter view of Figure 5.29.

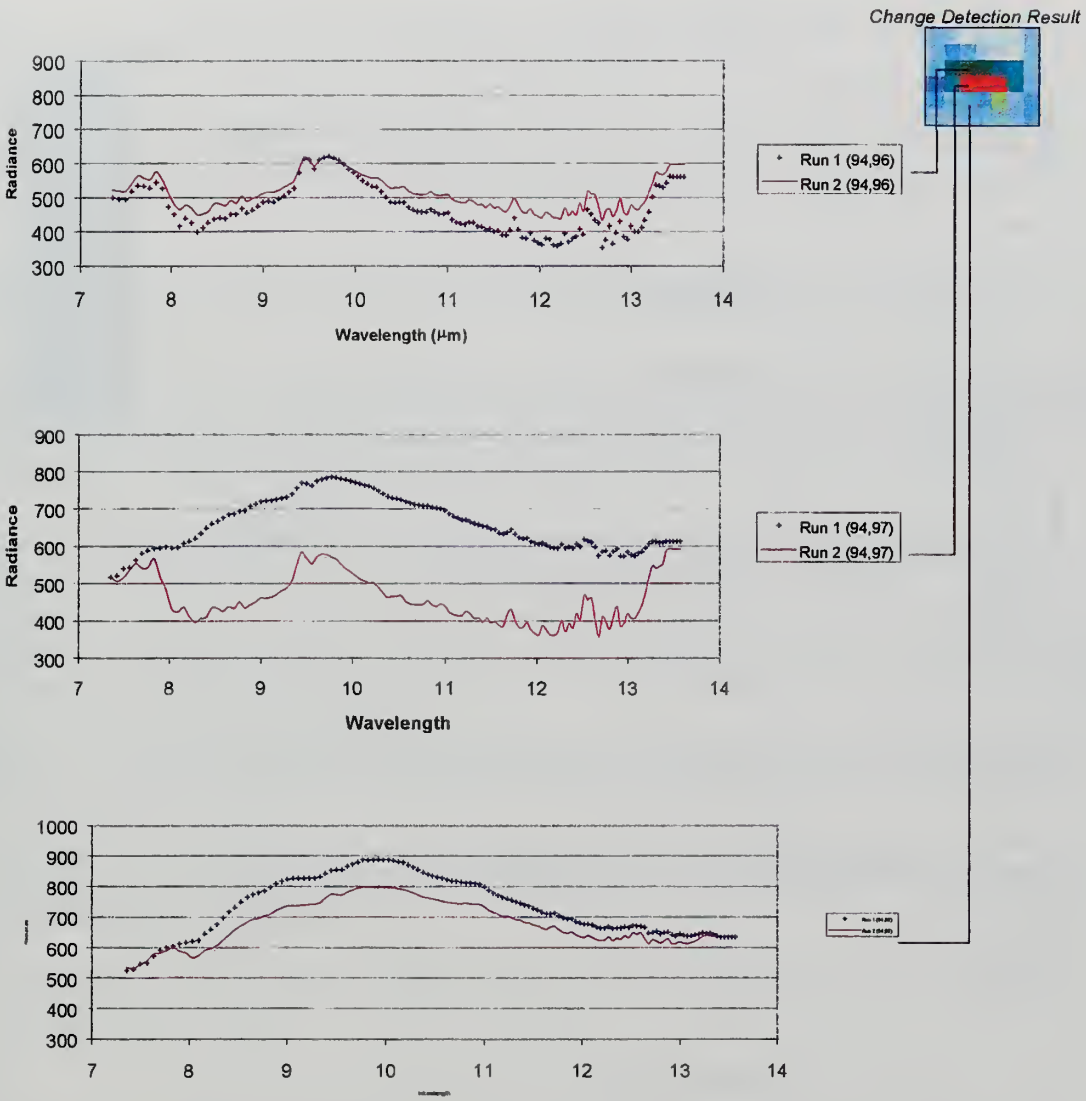

Figure 5.31: A sample of spectra from pixels that exhibit high change in the spectral angle result.

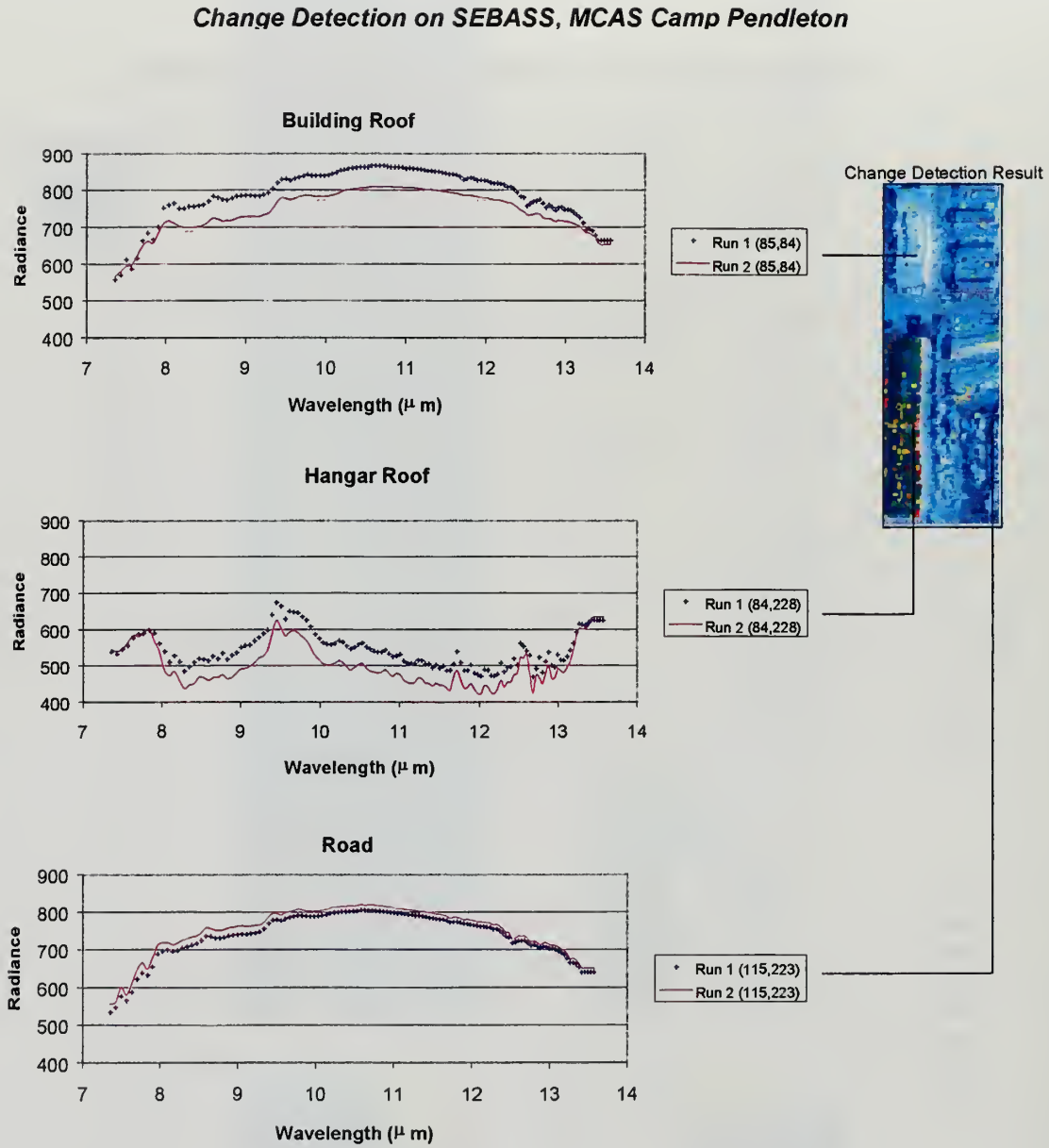

Figure 5.32: A sample of pixels representing varying degrees of change.

LIST OF REFERENCES

Carlotto, M. K., "Detection and Analysis of Change in Remotely Sensed Imagery with Application to Wide Area Surveillance," *IEEE Transactions on Image Processing*, vol. 6, no. 1, pp. 189-202, January 1997.

Collins, B. H., *Thermal Imagery and Spectral Analysis*, Master's Thesis, Naval Postgraduate School, Monterey, CA, September, 1996.

Coppin, P. R. and Bauer, M. E., "Processing of Multitemporal Landsat TM Imagery to Optimize Extraction of Forest Cover Change Features," *IEEE Transactions on Geoscience and Remote Sensing*, vol. 32, no. 4, pp. 918-927, July 1994.

Deer, P., "Digital Change Detection Techniques in Remote Sensing," Department of Defence, Defence Science and Technology Organization, DSTO-TR-0169, 19XX.

Dia, X., Khorram, S., "Quantification of the Impact of Misregistration on the Accuracy of Remotely Sensed Change Detection," *IEEE International Geoscience and Remote Sensing Symposium*, vol. 4, pp. 1763-1765, August 1997.

Hackwell, J. and Hayhurst, T., *In-scene Atmospheric Compensation of Infrared Hyperspectral Data*, The Aerospace Corporation, August 1995.

Hackwell, J., *SHARP (SEBASS II) Architecture (SEBASS High-Altitude Research Project*, The Aerospace Corporation, May 1997.

Hackwell, J., *The Aerospace SEBASS Hyperspectral Infrared Sensor*, The Aerospace Corporation, May 1997.

Hayhurst, T. L., *Elementary Thermal IR Phenomenology for SEBASS*, The Aerospace Corporation, June 1997.

Johnson, B. R., *SEBASS Calibration for Western Rainbow Collection*, The Aerospace Corporation, May 1997.

Kahle, A. B. and Rowan, L. C., "Evaluation of Multispectral Middle Infrared Aircraft Images for Lithographic Mapping in the East Tintic Mountains, Utah," *Geology*, vol. 8, pp.234-239, May 1980.

Kahle, A. B., Surface Emittance, Temperature, and Thermal Inertia Derived from Thermal Infrared Multispectral Scanner (TIMS) Data for Death Valley, California," *Geophysics*, vol. 52, no. 7, pp. 858-874, July 1987.

Lillesand, T. M. and Kiefer, R. W., *Remote Sensing and Image Interpretation*, 2nd ed., John Wiley & Sons, New York, NY, 1987.

Michener, W. K. and Houhoulis, P. F., "Detection of Vegetation Changes Associated with Extensive Flooding in a Forested Ecosystem," *Photogrammetric Engineering & Remote Sensing*, vol. 63, no. 12, pp. 1363-1374, December 1997.

Parzen, E., *Change Analysis*, Department of Statistics, Texas A & M University, no. 172, June 1992.

Ray, T. W., Farr, T. G., Blom, R. G., Crippen, R. E., and DeJong, E. M., "Using Airborne and Satellite Data for Multitemporal Studies of Land Degredation," *IEEE International Geoscience and Remote Sensing Symposium*, vol. 1, pp. 125-127, August 1994.

Riordon, C. J. "Non-urban to urban land cover change detection using Landsat Data," *Summary Report of the Colorado Agricultural Research Experiment Station*, Fort Collins, Colorado, 1980.

Schowengerdt, R. A., *RemoteSensing: Methods for Image Processing*, 2nd ed., Academic Press, San Diego, CA, 1997.

Schwartz, C. R., Cederquist, J. N., and Rogne, T. J., "Comparison of Modeled to Measured Infrared Multispectral Target/Background Signatures", *SPIE Proceedings*, vol. 2235, pp. 162-184, 1994.

Schwartz, C. R., Cederquist, J. N., Twede, D. R., and Eismann, M. T., "Detection of Low Contrast Hyperspectral Infrared Image Data," *Spectroradiometric Symposium*, November 1997.

Singh, A., "Change Detection in a Tropical Forest Environment of Northeastern India Using Landsat," *Remote Sensing and Tropical Land Management*, edited by M. J. Eden and J. T. Parry, John Wiley & Sons, London, England, pp. 237-254, 1986.

Singh, A., "Review Article: Digital Change Detection Techniques Using Remotely-Sensed Data," *International Journal of Remote Sensing*, vol. 10, no. 6, pp. 989-1003, 1989.

Singh, A., "Tropical Forest Monitoring Using Digital Landsat Data in Northeastern India," Ph.D. thesis, University of Reading, Reading England, 1984.

Smith, A. M., Schwartz, C. R., B*rassboard Airborne Multispectral Sensor System Specification Program, Phase 3: Image Measurements and Analysis, Volume 4: Redstone Arsenal Autumn 1996 Image Measurements*, Environmental Research Institute of Michigan, March 1997.

Stefanou, M. S., *A Signal Processing Perspective of Hyperspectral Imagery Analysis Techniques*, Master's Thesis, Naval Postgraduate School, Monterey, CA, June 1997.

Suga, Y., Inoue, T., Matsumoto, T., and Takeuchi, S., "Landcover Change Detection by Combination of NOAA/AVHRR with Landsat/TM," *IEEE International Geoscience and Remote Sensing Symposium*, vol. 4, pp. 2017-2019, August 1993.

Therrien, C. W., *Discrete Random Signals and Statistical Signal Processing*, Prentice Hall, New York, NY, 1992.

Tucker, C. J., "Red and Photographic Infrared Linear Combinations for Monitoring Vegetation," *Remote Sensing of the Environment*, vol. 8, pp. 127-150, 1979.

U.S.Army Engineer Topographic Laboratories, "New Methods in Change Detection Using Multispectral Data", DACA76-86-C-0018, May 1991.

Weismiller, R. A., Kristof, S. J., Scholz, D. K., Anuta, P. E., and Momen, S. A., "Change Detection in Coastal Zone Environments," *Photogrammetric Engineering and Remote Sensing*, vol. 43, pp. 1533-1539, 1977.

Willoughby, C. T., Marmo, J., and Folkman, M. A., "Hyperspectral Imaging Payload for the NASA Small Satellite Technology Initiative Program," *IEEE Proceedings of the Aerospace Applications Conference*, vol. 2, pp. 67-79, February 1996.

INITIAL DISTRIBUTION LIST

1. Defense Technical Information Center 2
   8725 John J. Kingman Road., Ste 0944
   Ft. Belvoir, Virginia 22060-6218

2. Dudley Knox Library 2
   Naval Postgraduate School
   411 Dyer Road
   Monterey, California 93943-5101

3. Richard C. Olsen, Code PH/OS 5
   Department of Physics
   Naval Postgraduate School
   Monterey, California 93943-5002

4. Chairman, Code SP 1
   Space Systems Academic Group
   Naval Postgraduate School
   Monterey, California 93943-5002

5. David Cleary, Code PH/CL 1
   Department of Physics
   Naval Postgraduate School
   Monterey, California 93943-5002

6. Captain E. Abbott 1
   Department of the Navy, CNO
   Code N632, Room 5P773, The Pentagon
   Washington, D.C. 20350-2000

7. Dr. John A. Hackwell 2
   Space and Environment Technology Center
   Aerospace Corporation
   2350 E. El Segundo Bl.
   El Segundo, California 90245-4691

8. Lt. Col. I. Falto-Heck 1
   USAF
   14675 Lee Road
   Chantilly, Virginia 20151-1715

9. Captain Rob Bonjovi 1
USAF
14675 Lee Road
Chantilly, Virginia 20151-1715

10. W. Williams 1
USAF
14675 Lee Road
Chantilly, Virginia 20151-1715

11. Dr. Greg Pavlin 1
SITAC
11781 Lee Jackson Memorial Highway
Suite 500
Fairfax, Virginia 22033-5309

12. Mark Pistokini 1
Joint Intelligence Center, Pacific
OTX
Box 500
Pearl Harbor, Hawaii 96860

13. Dr. John Schott 1
Center for Imaging Science
Rochester Institute of Technology
54 Lomb Memorial Drive
Rochester, New York 14623-5604

14. Dr. Alex F. Goetz 1
CSES/CIRES
Box 216
University of Colorado
Boulder, Colorado 80309

15. Dr. Jesse Leitner 1
AFRL/VSSS Bldg. 277, Suite 250
3550 Aberdeen Avenue SE
Kirtland AFB, New Mexico 87118-5776

16. Commander, Naval Space Command 1
ATTN: N112
5280 4th Street
Dahlgren, Virginia 22448-5300

17. Lieutenant Richard J. Behrens, USN 2
Joint Intelligence Center, Pacific
OTX
Box 500
Pearl Harbor, Hawaii 96860

12 483NPG TH 3179
10/99 22527-200

DUDLEY KNOX LIBRARY
3 2768 00368314 5